International Journal of Coastal, Offshore & Environmental Engineering

Since 2015

ISSN: 2980-8731 (online)

Special issue

Marine Renewable Energy

Volume 6 | Issue 5| Nov 2021

IJCOE

Editor-in-Chief: Prof. Hamid S.Bahai

International Journal of Coastal, Offshore & Environmental Engineering (IJCOE)

Vol. 6/ Issue. 5/ Nov 2021

25

INTERNATIONAL JOURNAL OF
IJCOE
COASTAL, OFFSHORE &
ENVIRONMENTAL ENGINEERING

Volume 6 | Issue 5 | Nov 2021

www.ijcoe.org

info@ijcoe.org

www.ijcoe.org

International Journal of
Coastal, Offshore
& Environmental
Engineering
Since 2015
ISSN: 2980-8731 (online)

In The Name of God

Message from the Editor-in-Chief

The IJCOE journal office was established in 2015,and its first issue was published in 2016. TheIJCOE covers a wide range of research in thefields of oceanography & ocean technology, aswell as marine industries & marine engineering.The editorial board of IJCOE consists of nearly130 of the greatest scientists and researchersfrom over 30 countries worldwide, and thejournal's review board comprises 1,000 membersfrom all five continents. The membership andapplication process for joining the editorial andreview boards of this journal is ongoing. IJCOE isa research-academic quarterly journal that haspublication and distribution permissions fromthe Press Organization and permission topublish scientific-research articles from theMinistry of Science, Research, and Technology(MSRT) with an "A" rating. It also holds a "Q1"rating from the ISC institute with an impactfactor (IF) of approximately 0.43 and isconsidered a "core journal" (prestigious andoutstanding journal). IJCOE is an open-accessjournal and allows the download and receipt ofaccepted articles in full text for free. It respectsand adheres to copyright and COPE regulations.The journal's office operates 24/7, providingservices to researchers. In addition to publishinga regular quarterly journal, IJCOE has 16 specialissues on specific topics in preparation. It alsoprovides conditions for publishing specializedbooks, references, and handbooks. Moreover, itis ready to cooperate with the secretariats ofreputable international conferences to publishtheir selected and outstanding articles. IJCOEevaluates, appraises, and publishes books,articles, and the scientific achievements andfindings of esteemed researchers and scientistsworldwide who are innovating and conductingin-depth research in the "important and strategicfield of the maritime technology & Oceanengineering." It welcomes any form of jointcooperation with universities, research institutes,and related research centers at the national,regional, and international levels, and extends ahand for collaboration.

Classification of Editorial Board in IJCOE

- Editor-in-Chief
- Director-in-Chief
- Deputy Editor
- Executive Managers
- English Text Editor
- Technical Editor
- International Editorial Board
- National Editorial Board
- Editorial Board Associate
- Editorial Board Assistant
- Guest Editorial Board
- Advisory Board
- Administrative Coordinator
- Honorary Board Member
- Methodology Advisor

Author Benefits

- Open Access
- Rapid Publication
- Thorough Peer-Review
- No Copyright Constraints
- Coverage by Leading Indexing Services
- Discounts On Article Processing Charges (APC)
- No Space Constraints, No restriction on the maximum length of the papers, number of figures or colors

Aims of IJCOE

Hydrodynamics

Marine equipment

Structural mechanics

Ocean environmental predictions

Stochastic calculations Experimental

Automatic Control of Marine Systems

Scope of IJCOE

Marine Hazards

Ocean Acoustics

Naval Architecture

Ocean Engineering

Coastal Engineering

Marine Meteorology

Marine Earth Sciences

Underwater Technology

Marine Renewable Energy

Polar & Arctic Engineering

Marine Renewable Energy

Marine Geography & Geodesy

Marine Environmental Engineering

Automatic Control of Marine Systems

Hydro Physics & Physical Oceanography

Type of papers

- Case Studies
- Book Reviews
- Review Article
- Letters to the Editor
- Methodology Papers
- Editorials and Commentaries
- Response or Rejoinder Papers
- Perspective or Opinion Papers
- Conceptual or Theoretical Papers
- Meta-Analysis and Systematic Reviews
- Short Communications or Brief Reports
- Research Articles (Original Research Papers)

Scientific Research Journal

Ministry of Science, Research And Technology (MSRT)

Jurnal Ranking 2023: A

Ministry Of Science, Research And Technology (ISC)
Citation Impact 2022: 0.429
Quartile 2022 : Q1
Core Collection

IJCOE is a Member of

- CIVILICA
- Google Scholar
- Jouroscope
- COPE 20TH ANNIVERSARY 1997-2017
- ISC
- JREF.IR Journals Reference
- DOAJ DIRECTORY OF OPEN ACCESS JOURNALS
- ISSN INTERNATIONAL STANDARD SERIAL NUMBER INTERNATIONAL CENTRE
- Researcher.Life
- doi Crossref mEDRA
- iThenticate
- magiran
- OPEN ACCESS
- pistotn
- ResearchGate
- Regional Information Center for Science and Technology RICEST
- ScienceGate
- Scilit
- SID
- website.informer.com
- WEBrate

Cantact Us

Office 1 | Research Institute of Meteorology and Atmospheric Science

Address | Tehran, Shahid Kharrazi Highway, Pajoohesh Blvd, Research Institute of Meteorology and Atmospheric Science, Sand and Dust Storm International Research Center (SDS-IRC), No. 13, 1st floor.

Phone | +982144787652

Postal code | 13611-14977

website | www.rimac.ac.ir

Office 2 | Iranian National Institute for Oceanography and Atmospheric Science

Address | Tehran, Dr. Fatemi Gharbi St., Shahid Etemadzade St., No. 3, third floor.

Phone | +982166944873

Postal code | 13389 – 14118

website | www.inio.ac.ir

Email | Info@ijcoe.org

Website | www.ijcoe.org

Follow Us

www.ijcoe.org

INTERNATIONAL JOURNAL OF IJCOE COASTAL, OFFSHORE & ENVIRONMENTAL ENGINEERING

Volume & Issue:

Volume 6, Issue 5, November 2021

Special issue of “Marine Renewable Energy”

Number of Articles: 6

Content

INTERNATIONAL JOURNAL OF
COASTAL & OFFSHORE ENGINEERING

IJCOE Vol.6/No.5/ Autumn 2021 (1-9)/ **Special issue of "Marine Renewable Energy"**

Available online at http://www.ijcoe.org

The role of different positions of tidal turbines for energy extraction in Qeshm channel

Maryam Soyuf Jahromi[1*], **Mahdieh Emami**[2]

[1] Assistant Professor of physical oceanography, Department of Nonliving Resources of Atmosphere and Ocean, Faculty of Marine Science and Technology, University of Hormozgan, Bandar Abbas, Iran; oyufjahromi@yahoo.com.au*

[2] PhD candidate of physical oceanography, Department of Nonliving Resources of Atmosphere and Ocean, Faculty of Marine Science and Technology, University of Hormozgan, Bandar Abbas, Iran; mahdiehemami94@yahoo.com

ARTICLE INFO

Article History:
Received: 16 Nov. 2021
Accepted: 30 Nov. 2021

Keywords:
Energy extraction
Turbine
Khuran Strait
Tides
Mike3

ABSTRACT

The use of renewable energy instead of oil and gas reservoirs in the Persian Gulf can be a good platform for renewable energy farms. This study investigates the energy generated by the tidal flow velocity in the Qeshm channel, using a three-dimensional hydrodynamic model, MIKE3, Flow Model FM. By installing a hypothetical tidal turbine from Voith Company, with a diameter of 1 m at seven different stations of the model (respectively from east to west of the channel), the tidal energy from the horizontal flow of the area is calculated. In the mentioned simulation, wind stress and thermohaline flow are ignored so that the dominant current is the current caused by the change of water level due to the tide. The flow velocity pattern in spring and neap tides at Higher High Water (HHW) was then analyzed at the seven stations. The energies of the simulated currents showed that the east side of the channel had more energy potential on the days of spring tides, so that at IP1 station, in the first spring tide, 175 watts of electricity is generated, which in the second spring tides decreases by 28.5%. On the other hand, the west side of the channel had the potential to generate electricity in neap tides. Station IP6 had the potential to generate electricity in both the spring and neap tides, which had more neap tides potential than the spring tides. The difference in power generated in the first and second neap tides at IP6 was only 0.7%, which is less than 30.2 W compared to the first and second spring tides. Therefore, it can be said that according to the shape of the region, the second bend of Qeshm channel was a more suitable place for energy extraction with the assumed tidal turbine in the region.

1. Introduction

One of the most important ways to use renewable energies is the use of the seas energies. Using seas to receive energy has attracted attentions of the international community after the oil crisis of the 1970s. Marine Renewable Energies (here after MRE) have the ability to provide 7% of global electricity demand [1]. Among all MRE, the tidal current energies are due to the tides, resulting the gravitational pull of the moon [2][3]. Tidal energy is one of the most reliable and promising energy sources [4], due to its predictability and many other attractive features [5]. It can also reduce reliance on fossil fuels. Tidal energy is expressed both as the kinetic energy of tidal currents and as potential energy of the water level difference between the tides.

The flows of tides in tidal channels are particularly important, especially in places where the density difference and wind-driven flows (as the other two types of marine currents; [6] are insignificant. Moreover, the flow pattern can be locally affected by shoreline shape and depth changes [7]. Therefore, identifying the best place to install tidal current turbines will be one of the challenging issues in the MRE basin. In this regard, countries such as China (e.g. [3]), the European Union (e.g. [8], the United Kingdom (e.g. [9], and other developed countries, have conducted researches in this field in order to take a step towards economic savings of this type of renewable energy. Few researches have been done in Iran [10][11][12] that deal with these issues. In this study, the Qeshm tidal channel, located in the north of the Strait of Hormuz, which is strongly affected by the tides [13][14], has been simulated to identify the location of the maximum tidal flow velocity in the channel. Then, the best place to receive tidal energy is calculated by assumptive tidal turbines in different selected positions along Qeshm channel.

2. Materials and Methods

2.1. The study area

The studied area was the Qeshm tidal channel (Figure 1, 26.66-27.15°N, 55.23-56.27°E), located in the north of the Strait of Hormuz, Persian Gulf (24-30°N, 48-56°E). Persian Gulf is a semi-closed basin [16] with a length of 990 km, a width of 56-338 km, and an average depth of 35 m [17][18]. It is located in the southwest of Asia on a continental shelf. The Persian Gulf is connected to the Oman Sea and the Indian Ocean by the Strait of Hormuz and is surrounded by Iran, Iraq, Kuwait, Saudi Arabia, Bahrain, Qatar, and the United Arab Emirates.

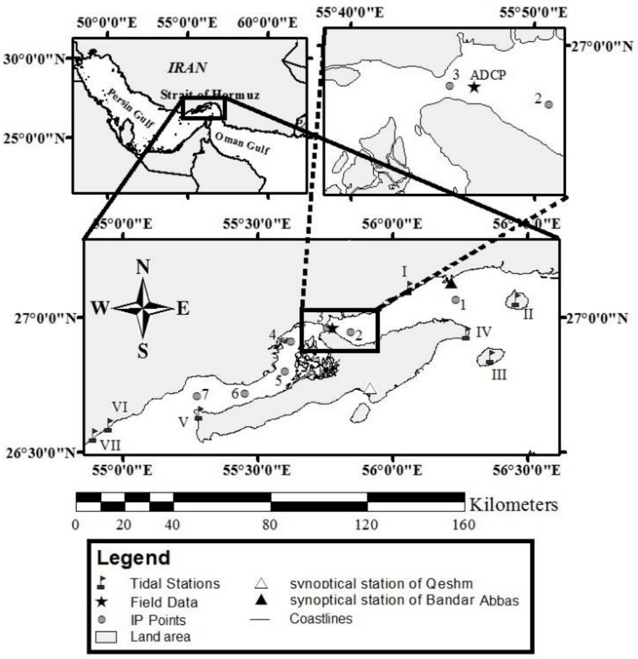

Figure 1. Geographical location of Qeshm channel relative to Persian Gulf. Stations 1 to 7 are the position of model outputs along the channel to determine the maximum tidal velocity of the channel. Stations I to VII are tidal stations. The triangles are meteorological stations and the star is the location of ADCP. This figure is prepared in ArcGIS [15] environment.

The Strait of Hormuz is also a curved waterway (Figure 1) that separates the Iranian plate from the Arabian plate and connects Persian Gulf to Oman Sea. The bottom of Strait of Hormuz has a steep slope in the north-south direction. This strait is internationally strategic and the countries of its border produce 30% of the world's oil which is exported through the Strait of Hormuz. In addition to oil, 45% of the world's natural gas reserves are held by the region countries [19]. The existence of oil has led to the economic dependence of countries in the region on oil, and therefore in the field of MRE, no serious action has been taken by countries of the region [20]. Qeshm Island, is the largest island of Persian Gulf with an area of 2.5 times the country (island) of Bahrain [21] in the Strait of Hormuz. Qeshm channel is located between the north of Qeshm Island and the south coast of Iran. This channel is also sometimes called the Khuran Strait (Figure 1). This channel is also known by its eastern important ports (Shahid-Rajai and Bahonar port) and its western aquatic environment (mangrove forests) near IP4 of Figure 1 and it has unique complexities.

Although the length of the Persian Gulf from the Strait of Hormuz to the northwestern part of Arvand River (with discharge of 435 m^3s^{-1}, [22]) is approximately 1000 km [23][24], but the length of the Qeshm channel is about 110 km [25]. The maximum width of the channel is 25 km between Bandar Abbas and Qeshm city and the minimum width of the channel is 3.5 km between the Pohl port and Laft port in the Khuran Strait [25].

The Persian Gulf's climate is affected by extra-tropical weather system, which comes from the northwest. On the other side, the Oman Sea is affected by the tropical system of the Arabian Sea and the Indian Ocean, so that the monsoon cycle causes south winds in summer and strong north winds in winter. The Strait of Hormuz is the border of these two climate systems [18], which modulates the effects of those two systems; so that the prevailing wind is local and short-lived duration. Hence, the Qeshm channel is more affected by tides [25] than the prevailing climatic patterns. The Qeshm channel tides are mixed semidiurnal tides and affected by K_1, N_2, S_2, M_2, and O_1 components [26][27][28]. Since Qeshm channel is affected by the shape of its coastline [29], then the natural characteristics can affect the placement of devices in energy extraction.

2.2. The simulation method

To study the Qeshm channel MRE, the three-dimensional hydrodynamic model MIKE 3 [30], Service Pack 3, 2012 version, related to the Danish Hydraulic Institute (DHI) has been used, which has already been used in other aquatic basin studies (such as [31], [30], [32], [33], [34]). Besides, the models of this institute have been already tested in the Qeshm channel area (for example [35], [36], [37] and [29]). The MIKE 3 flow model, abbreviated MIKE 3 FM, hereinafter referred to MIKE, uses the finite volume method. This hydrodynamic module solves the three-dimensional equations of stability, mass, and time-dependent momentum, the incompressibility of Navier-Stokes equations using the Boussinesq approximation and the hydrostatic pressure. MIKE uses the UNESCO equations for seawater state (1980) [38] in the form of a series of relationships between salinity, temperature, and density [39]. Its most important feature is the flexible triangular and rectangular grid with different sizes in its computational range [40], which it is used a triangular grid in this study (Figure 2). Figure 2 shows the details of grids and bathymetry of the Qeshm channel, prepared in the MIKE Zero. Numbers of created triangular grids were 4433 with 3136 points. The topographic information of the area is provided by

NOAA NGDC and provided by ERDDAP Server [41]. The main source of NOAA NGDC data is the ETOPO1 satellite, which is made up of multiple regional and global datasets and connects the data with an alternative global model of the land surface, land topography, and ocean bathymetry.

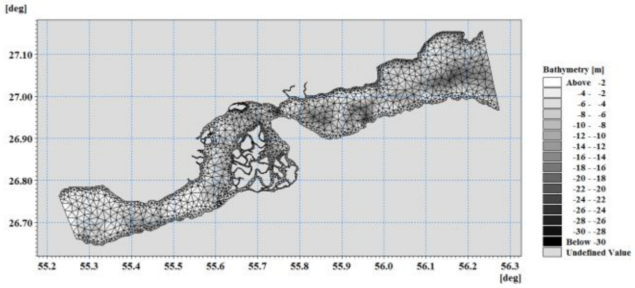

Figure 2. The bathymetry of Qeshm channel with the flexible triangular mesh scheme of the model in MIKE3.

The used coordinate system for the simulation was the Cartesian coordinate system in horizontal directions, and the Sigma coordinate system in the vertical direction, so that the vertical coordinates could follow the elevation of the bed. The numbers of layers of the Sigma coordinate system were considered five levels, which was appropriate due to the shallow depth of the area (with maximum depth of -30 m). The thickness of each layer varies from at least 0.4 m to 6 m (depending on bed depths and changes of water levels in spring and neap tides).

Two land (hard) borders in the north and the south of domain and two open borders in the east and the west were considered (Figure 2) where the open borders could change the water level due to tides. The length of the channel was 110 km and its width was 19.8 km in the eastern border and 11 km in the western border with the maximum depth of -30 m. Tidal data were used on the open borders. Table 1 shows the location of tidal stations around the Qeshm channel (flags I to VII of Figure 1). It was used the stations of I and VI for tidal injection into the simulation.

Table 1. Tidal stations on the domain.

No.	Station Name	Location	
		Latitude (˚N)	Longitude (˚E)
I	Bandar-E Shahid Rajai	27.11093415	56.0605717
II	Hormuz Island	27.0678342	56.46119855
III	Larak	26.85571385	56.36407975
IV	Bandar-E Bahman	26.9455038	56.2775832
V	Basaidu	26.6447722	55.2829242
VI	Bandar Lengeh	26.5640657	54.8908389
VII	Bandar Kong	26.6028576	54.94731545

Since the location of Qeshm channel is almost horizontal, narrow, and long and because of small variations of its latitude (26.6ºN-27.2ºN, with the width of approximately about 0.8 degrees), it does not cause much deviation in the Coriolis parameter. Maximum changes in the Coriolis parameter are less than one percent (0.45%). Therefore, the changes of the Coriolis force can be ignored in the current simulation.

Maximum wind speed and direction information, in two synoptical stations of Bandar Abbas (27.13ºN and 56.22ºE and 9.8 m above sea level [42], black triangle on Figure 1) and Qeshm (26.73ºN and 55.91ºE and 6 m above sea level, white triangle on Figure 1) were extracted from the Meteorological Organization of Iran in January 2016. Figure 4 shows these data in Matlab software [43]. It can be seen that the two meteorological stations are slightly different from each other. The average wind speed of Qeshm station is 5.80±2.31 m/s (mean ± standard deviation) and Bandar Abbas station is 5.67±1.71 m/s (mean ± standard deviation). Therefore, due to the small size of Qeshm channel, the wind speed can be considered constant and equals to 5.74 m/s in the whole domain. To simplify the simulation, the wind speed was considered to be zero, which was previously assumed in the study of [25]. The wind patterns are also local, so it is reasonable to consider the wind speed equals with zero. Therefore, it was assumed that wind stresses of the basin are negligible (according to the study of [25]) and equal to zero. It was also assumed that the current due to the density difference does not have much effect on the channel (according to the study of [25]) and the current caused by the waves has not been considered. As a result, it was assumed that the current pattern of Qeshm channel in this simulation were effected by tides.

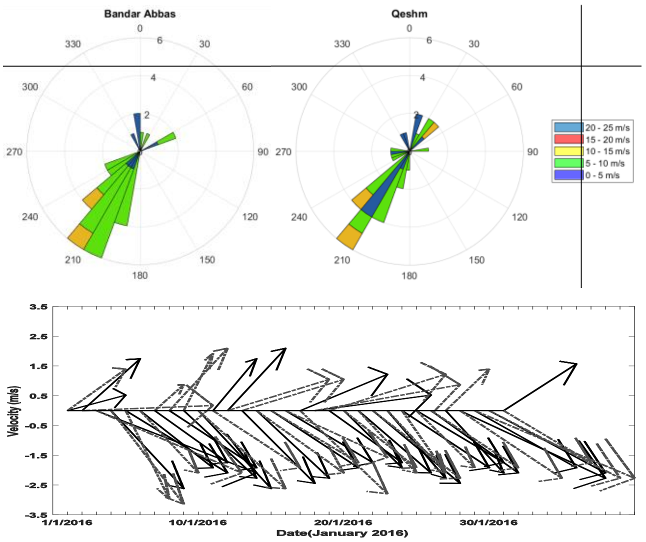

Figure 3. Comparison of wind speed between two synoptical stations of Bandar Abbas (black triangle of Figure 1) and Qeshm (white triangle of Figure 1), in January 2016. Up) Wind rose of Bandar Abbas and Qeshm. Down) The same feather diagram, for Bandar Abbas (black solid line) and Qeshm (gray dash line).

The simulation outputs included the flow speed and direction along horizontal and vertical directions, the velocity components along x, y and z axes. For the longitudinal check of Qeshm channel, seven stations (IP1 to IP7 of Table 2) were selected to study outputs quantitatively. These stations are shown on Figure 1 as gray points numbered one to seven. In each station it was installed an assumptive turbine.

Table 2. Location of turbines on the studied area as illustrated on Figure 1.

Station names	Geographical location	
	Latitude (˚N)	Longitude (˚E)
IP 1	27.06656	56.23585
IP 2	26.94609	55.84574
IP 3	26.9633	55.75624
IP 4	26.91282	55.622
IP 5	26.80152	55.6002
IP 6	26.71891	55.45219
IP 7	26.70973	55.27549

The appropriate input data is a good way to achive a good simulation. And then the model was run for one month (January, 2016) and the model outputs were extracted in the stations mentioned on Table 2 in spring and neap tides (Table 3).

Table 3. Spring and neap tides of the model

Date (year/m/d)	Time (hour)	Tidal type		Model time step
2016/1/2	1:00	1st Neap	HHW[*]	24
	7:00		HLW[+]	30
	13:00		LHW[**]	36
	19:00		LLW[++]	42
2016/1/11	4:00	1st Spring	HLW	243
	10:00		LHW	249
	16:00		LLW	255
	22:00		HHW	261
2016/1/18	3:00	2nd Neap	LHW	410
	9:00		HLW	416
	15:00		HHW	422
	22:00		LLW	429
2016/1/26	4:00	2nd Spring	LLW	603
	10:00		LHW	609
	16:00		HLW	615
	22:00		HHW	621

[*] HHW stands for Higher High Water

[+] LHW stands for Lower High Water

[**] HLW stands for Higher Low Water

[++] LLW stands for Lower Low Water

To extract the most suitable water level data for open boundaries, it was used Tidal Model Driver, hereafter TMD package version 2005 [44], related by Oregon State University [45] in Matlab software [43]. This software was written by Oregon State University in 2003 and was used in other studies such as [46]. This package can predict tides by the accuracy of at least one minute by one minute at any various point of the whole world. It was used the tidal amplitudes and phases of the eight main components (M2, S2, N2, K2, K1, O1, P1, Q1) of Persian Gulf on the special Persian Gulf version of TMD package by the resolution of 30 seconds on 30 seconds in January 2016 [47][48].

The reason of using TMD package was good accuracy on the field measurement comparisons. Figure 4 is a sample comparison (in January 2016) between TMD model (solid lines) and the field Iran National Cartographic Center water levels data in an eastern station (Bandar Abbas, Figure 4, up) and a western station (Bandar Lengeh, Figure 4, down) of open boundaries (dot lines). It is obvious that TMD can predict roughly accurate tidal information. This is obvious from the comparisons of measured data of all stations of Table 1 with TMD and tidal information of Tides4fishing website [49].

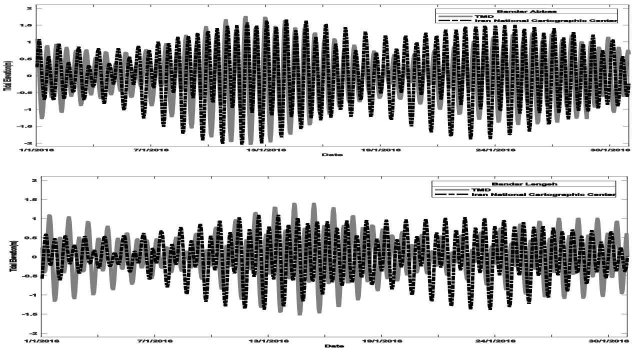

Figure 4: Comparison of model input data achieved by TMD (solid lines) and Iran National Cartographic Center field data (dot lines) in (up) eastern and (down) western boundaries in January 2016.

In order to force MIKE3 by tidal inputs of open boundaries, the average of four eastern station (I, II, III and IV of Table 1) was used for eastern boundary and the average of three western stations (V, VI and VII of Table 1) were used for western boundary of Qeshm channel. Their means were respectively 1.68 m and 2.03 m on the eastern and western boundaries. To import tidal data to MIKE3, it was used the middle of each eastern and western boundary.

To calibrate and validate MIKE3 model, measured ADCP current speed (located 26.963°N and 55.779°E) at depth 13 m from the bed near the Qeshm channel narrowing (Figure 1, star point) by one-hour interval from 1 September 2005 to 11 September 2005 was compared with model (Figure 5) by two different tidal inputs of TMD and Tides4fishing website. These tidal data were entered into the open east and west boundaries of the MIKE3 model, as times series, with the extension of dfs0. Because each time-series data of the stations can be extracted and mapped for analysis and statistics at those stations and maps [51]. Then, the exact correct point of the field data (Figure 1, star point) was also defined in the model as an output. The horizontal tidal velocity described as:

$$U_h=\sqrt{u^2+v^2} \tag{1}$$

where in Eq.(1), U_h stands for the horizontal tidal speed and u and v are horizontal components of tidal current in m/s.

The proper bed coefficient was also checked for the accuracy of results. In order to do that the model was implemented with the tide of 2005 and with different bed coefficients to compare the horizontal speed of the model sorted by different type of tides with the horizontal speed of the field data. From all tested and compared values of the bed coefficient of the model, the value of 0.004 was the most appropriate bed coefficient (Figure 5). As it is also obvious by the final outputs of MIKE3, there is better match between TMD input to the open boundaries of MIKE3 than Tides4fishing ones. Therefore, TMD was a better choice as tidal boundaries inputs of MIKE3. Although, there is a phase difference of 2 and 3 hours with the ADCP data. Since the type of tides of area are semidiurnal by the period of 12 hours and 50 minutes, then this phase difference, is about 15-23%, and therefore it is roughly appropriate and acceptable.

For tidal energy, various formulas have been proposed. Here, it was used Eq.(2) which was previously studied by others (e.g. [52], [53], and [54]) as:

$$P_{TK} = -\frac{1}{2}\rho A\overline{U_A^3} \qquad (2)$$

where in Eq.(2) ρ stands for the flow density and is equal to 1025 kg/m^3 for the studied area [25]; A is the cross-section of the turbine in m^2, and U is the averaged fluid velocity achieved by the simulation in m/s. Since on different bed depths and at different tidal currents scales, different type of turbines can be used, then a small type of Pit turbine type has been selected from Voith company for this simulation. These turbines have a diameter of 0.80 to 8.40 m [55] and the diameter of the installed turbine in the model was considered equal to one meter.

The model included turbines and was run in January 2016 on Widows 8.1 Enterprise by a corei7 CPU, RAM of 8 GB and hard of 1 TB by time intervals of one hour. The times series of model velocity components on the exact time of Higher High Water, HHW, of each day, transferred to Microsoft office Excel [56] to achieve the horizontal velocity speed of the stations.

4. Results and Discussion

The horizontal speed of HHW in both neap and spring tides in January 2016 are stated in Table 4 and 5, respectively. The average surface horizontal speed of HHW in spring tides is 0.22 m/s (IP2 to IP6). This value is 0.17 m/s in neap tides. For bottom layer, these values decrease to 0.16 and 0.13 m/s in spring and neap tides respectively. It means that the average speed is higher at surface layer in compare with bottom layer in both spring and neap tides. As it is also obvious for all stations, the tidal horizontal flow speed trend is also the same for surface and bottom layers by reduced values of bottom layer.

Table 4. The calculated horizontal speed (in meters per seconds) at the stations (IP2 to IP6, Figure 1) of Qeshm channel at neap tides in January 2016.

Date	Station	The horizontal speed (m/s)		
		Surface layer	Bottom layer	Difference (Surface–Bottom) (%)
2nd January 2016 (1st Neap Tide)	IP2	0.13	0.10	2.90
	IP3	0.27	0.19	7.38
	IP4	0.14	0.11	3.27
	IP5	0.13	0.09	3.23
	IP6	0.26	0.20	6.76
	Average	0.19	0.14	4.71
18th January 2016 (2nd Neap Tide)	IP2	0.10	0.08	2.10
	IP3	0.19	0.15	4.60
	IP4	0.13	0.10	2.95
	IP5	0.12	0.10	1.23
	IP6	0.24	0.18	6.15
	Average	0.16	0.12	3.41

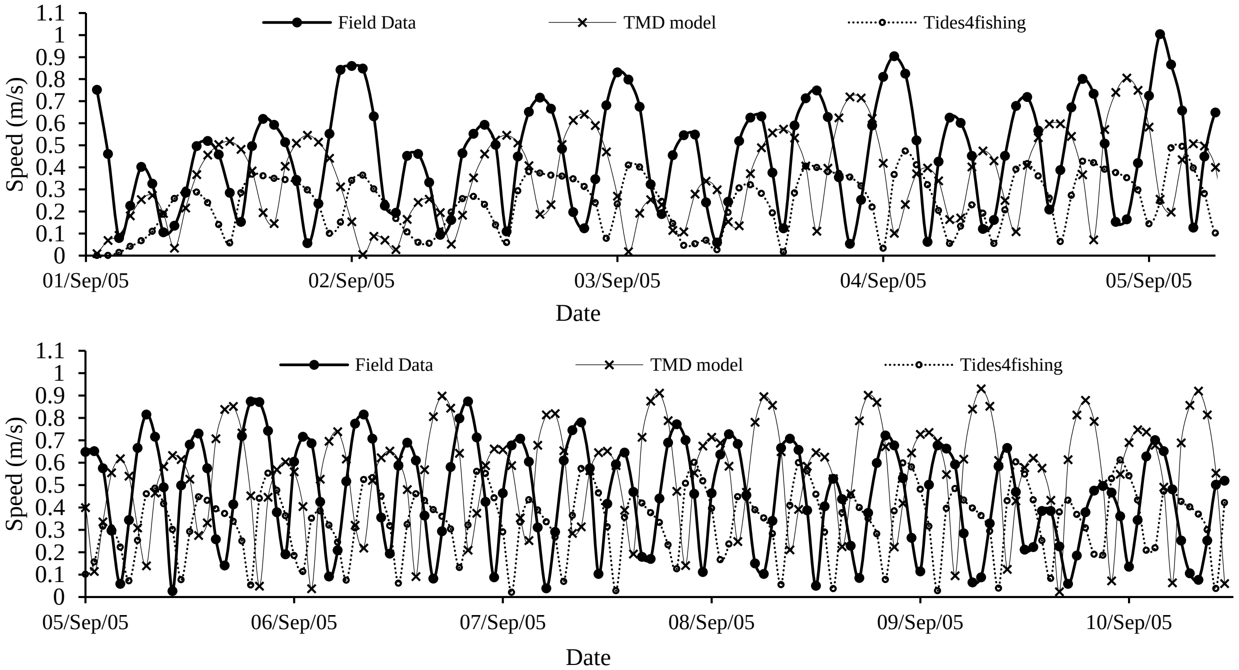

Figure 5. Comparison of MIKE3 current speeds (in meters per seconds) by different tidal input sources in September 1, 2005 to September 11, 2005. Tidal Model Driver input to MIKE3 are as solid line-cross points; Tides4fishing website [49] input to MIKE3 are as dot line-dot points and field data of [50] are as solid line-dot points.

Table 5. The calculated horizontal speed (in meters per seconds) at the stations (IP2 to IP6, Figure 1) of Qeshm channel at spring tides in January 2016.

Date	Station	The horizontal speed (m/s)		
		Surface layer	Bottom layer	Difference (Surface–Bottom) (%)
11th January 2016 (1st Spring Tide)	IP2	0.19	0.15	4.25
	IP3	0.37	0.26	10.42
	IP4	0.21	0.16	5.10
	IP5	0.17	0.13	4.03
	IP6	0.27	0.20	6.93
	Average	0.24	0.18	6.14
26th January 2016 (2nd Spring Tide)	IP2	0.16	0.12	3.49
	IP3	0.31	0.22	8.61
	IP4	0.16	0.12	3.72
	IP5	0.13	0.10	3.21
	IP6	0.25	0.19	6.40
	Average	0.20	0.15	5.09

Moreover, the average speed is higher on 1st and 2nd spring tides (0.24 and 0.20 for surface layer, and 0.17 and 0.15 for bottom layer, respectively). This amount is lower on 1st and 2nd neap tides (0.19 and 0.16 for surface layer, and 0.14 and 0.12 for bottom layer, respectively). At all stations (Table 4 and 5), the tidal horizontal speeds increase in both surface and bottom layers at spring tides while lower values are available for tidal speeds at neap tides.

Table 5 also shows that on the surface and bottom layers, the highest speeds referred to IP3 at the two spring tides (0.37 and 0.26 m/s during the first spring tide and 0.31 and 0.22 m/s during the second spring tide, respectively). It means that this station has potential for extract of tidal current energy. According to Table 5, the lowest values of surface and bottom layers referred to IP5 (0.17 and 0.13 m/s during the first spring tide and 0.12 and 0.10 m/s during the second spring tide, respectively) in the two spring tides (Table 5). Furthermore, in neap tides, IP6 has more high speed values on the surface and bottom layer (0.26 and 0.20 m/s at higher high water of the first neap tide and 0.24 and 0.18 m/s at HHW of the second neap tide, respectively) in compare with IP3 at the same time due to Table 4. It is also obvious that the horizontal speed of IP2 and IP5 both are small in neap tides and it means that these two stations are not suitable for extracting tidal current energy.

Therefore, results of Table 4 and 5 made clear that the positions of stations are important for high values of tidal horizontal speed (Eq. 2). The speed is low on IP2, the station before the narrowing part of the channel on the right of domain. Then it suddenly increases on IP3, the station exactly located on the first and most narrowing part of Qeshm channel. The IP3 speeds approximately doubles in compared with the previous station, IP2. Thereafter, the tidal horizontal speed decreases at IP4 before the mangrove forests and after the narrowest part of the channel. On IP5, after the mangrove forests, the horizontal tidal speeds decrease again and then increase again at the second narrowing part of the channel, IP6. This rhythm repeats by the period of 4 days between stations from IP2 to IP6.

On the other hand, as it is stated, there is a significant difference in station IP3 compared to IP2. The speed at station IP3 is almost twice that of IP2, which may be due to the difference in morphological characteristics of the location of station IP3 compared to IP2. This can reinforce the initial hypothesis about the effective location for extracting the most tidal energy.

Figure 6 shows the average tidal energy power in both the spring and the neap in January 2016 at each of the seven stations of Table 1.

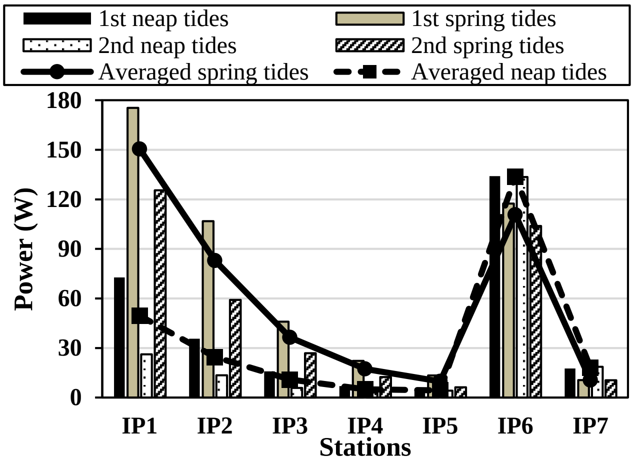

Figure 6. The averaged tidal energy powers (in watts) of turbines in January 2016 in spring and neap tides.

It can be seen that the highest tidal power is related to IP1 in the first spring tides (175.4 W) and then at the point IP6 in the first neap tides (134 W). Then, the first neap tides on IP6 and the second spring tides on IP1 are next with 125.5 and 133 watts, respectively. Relatively, the IP6 point has the most power among the stations at all four periods, with a maximum difference of 30 watts relative to each other. Station IP5 also has the lowest power between stations, which, due to its position after the middle curve of the channel, it makes sense to have the lowest tidal current velocity and therefore the lowest tidal energy. In general, except IP6 and IP7 stations, which have more power in neap tides, in other stations, the highest amount of power generation energy by the turbines are allocated to the days of the spring tides.

5. Conclusions

Results clearly showed that tidal velocities of Qeshm channel increased in both surface and bottom layers at the spring tides. It will be because of higher water levels of spring tides in compare with neap tides.

The model results of tidal current energy in Qeshm channel also illustrate that the location of the turbine installation is important. A spatial study of the highest power of installed turbines in different studied stations, showed well that the IP6 station has the highest amount of power generation capacity in both the spring and the neap tides, which according to the model results, it has the highest flow velocity. Although the greatest depth, and of course the highest speed was near the Qeshm channel (IP3 station), the potential of IP6 station was more than IP3 station in both the spring and the neap tides at HHW.

It should be noted that in this study, only one turbine with the lowest cross section (turbine diameter) had been used in the simulations and calculations. Of course, in areas with more depth than the channel, turbines with more number and cross-section can be used to increase energy production capacity, which has the greatest depth near the narrowing part of the Qeshm channel.

List of Symbols

A	cross-section of the turbine [in m^2]
HHW	Higher High Water [in m]
HLW	Higher Low Water [in m]
LHW	Lower High Water [in m]
LLW	Lower Low Water [in m]
P_{TK}	Tidal energy power [in Watts]
u	The first horizontal component of tidal current [in m/s]
U_A	The averaged simulated fluid velocity for the turbine [in m/s]
U_h	The horizontal speed of tidal current [in m/s]
v	The second horizontal component of tidal current [in m/s]
ρ	density [in kg/m^3]

8. References

[1] Fox, C.J., Benjamins, S., Masden, E.A. and Miller, R., (2018), *Challenges and opportunities in monitoring the impacts of tidal-stream energy devices on marine vertebrates*. Renewable and Sustainable Energy Reviews, Vol.81, p.1926-1938.

[2] Sverdrup, K.A., Duxbury, A. and Duxbury, A.C., (2006), *Fundamentals of oceanography*. McGraw-Hill Higher Education.

[3] Liu, H.W., Ma, S., Li, W., Gu, H.G., Lin, Y.G. and Sun, X.J., (2011), *A review on the development of tidal current energy in China*. Renewable and sustainable energy reviews, Vol.15(2), p.1141-1146.

[4] Gu, Y.J., Lin, Y.G., Xu, Q.K., Liu, H.W. and Li, W., (2018), *Blade-pitch system for tidal current turbines with reduced variation pitch control strategy based on tidal current velocity preview*, Renewable Energy, Vol.115, p.149-158.

[5] Lee, J.H., Park, S., Kim, D.H., Rhee, S.H. and Kim, M.C., (2012), *Computational methods for performance analysis of horizontal axis tidal stream turbines*. Applied energy, Vol.98, p.512-523.

[6] Talley, L.D., (2011), *Descriptive physical oceanography: an introduction*. Academic press.

[7] Baker, C., (1991), *Tidal power*. Energy Policy, Vol.19(8), p.792-797.

[8] Magagna, D. and Uihlein, A., (2015), *Ocean energy development in Europe: Current status and future perspectives*. International Journal of Marine Energy, Vol. 11, p.84-104.

[9] Xia, J., Falconer, R.A. and Lin, B., (2010), *Impact of different operating modes for a Severn Barrage on the tidal power and flood inundation in the Severn Estuary*, UK. Applied Energy, Vol.87(7), p.2374-2391.

[10] Zabihian, F. and Fung, A.S., (2011), *Review of marine renewable energies: case study of Iran*. Renewable and Sustainable Energy Reviews, Vol.15(5), p.2461-2474.

[11] Rashid, A., (2012), *Status and potentials of tidal in-stream energy resources in the southern coasts of Iran: A case study*. Renewable and Sustainable Energy Reviews, Vol.16(9), p.6668-6677.

[12] Uihlein, A. and Magagna, D., (2016), *Wave and tidal current energy–A review of the current state of research beyond technology*. Renewable and Sustainable Energy Reviews, Vol.58, p.1070-1081.

[13] Sabbagh-Yazdi, S.R., Zounemat-Kermani, M. and Mastorakis, N.E., (2008), *Simulation wetting and drying of mangrove forests due to tidal currents in Qeshm canal*. International Journal of Mathematical Models and Methods in Applied Science, Vol.2(1) p.18-23.

[14] Sabbagh-Yazdi, S.R. and Zounemat-Kermani, M., (2009), *Numerical solution of tidal currents at marine waterways using wet and dry technique on Galerkin finite volume algorithm*. Computers and fluids, Vol.38(10), p.1876-1886. doi:10.1016/j.compfluid.2009.04.010

[15] ESRI, (2011), *ArcGIS Desktop*, 64-bit, Version 10.3, Released 2011, Redlands, CA: Environmental Systems Research Institute.

[16] Barth, H. J., and Khan, N. Y. (2008), *Biogeophysical setting of the Gulf.* In Protecting the Gulf’s marine ecosystems from pollution, p.1-21. Birkhäuser Basel.

[17] Sheppard, C., Price, A. and Roberts, C., (1992), *Marine ecology of the Arabian region: patterns and processes in extreme tropical environments*. London, Academic Press.

[18] Reynolds, R.M., (1993), *Physical oceanography of the Gulf, Strait of Hormuz, and the Gulf of Oman—Results from the Mt Mitchell expedition*. Marine Pollution Bulletin, Vol.27, p.35-59.

[19] Cordesman, A.H., (2007), *Iran, oil, and the Strait of Hormuz*. Washington: Center for Strategic and International Studies. p.2-4.

[20] Al-Maamary, H.M., Kazem, H.A. and Chaichan, M.T., (2017), *Renewable energy and GCC States energy challenges in the 21st century: A review*. International Journal of Computation and Applied Sciences IJOCAAS, Vol.2(1), p.11-18.

[21]Fazelpour, F., Soltani, N., Nazari, A. and Katal, F., (2015), *Feasibility of satisfying electrical energy needs with wind-photovoltaic-battery hybrid power systems for a household in Qeshm Island Iran*, International Congress Energy and Environmental Engineering and Management Conference, Paris, France.

[22]Karbassi, A., Bidhendi, G.N., Saeedi, M. and Rastegari, A., (2010), *Metals removal during estuarine mixing of Arvand River water with the Persian Gulf water*. Open Geosciences, Vol.2(4), p.531-536.

[23]Moeini, M.H., Etemad-Shahidi, A. and Chegini, V., (2010), *Wave modeling and extreme value analysis off the northern coast of the Persian Gulf*. Applied Ocean Research, Vol.32(2), p.209-218.

[24]Yao, F., (2008), *Water mass formation and circulation in the Persian Gulf and water exchange with the Indian Ocean*. PhD thesis, University of Miami.

[25]Mahmoudov, M., Chegini, V. and Montazeri Namin, M., (2011), *Three-Dimensional Simulation of Qeshm Channel Currents*. Journal of the Persian Gulf, Vol.2(3), p.9-16.

[26]Foreman, M.G.G., (1979), *Manual for tidal heights analysis and prediction*. Pacific Marine Science Report 77-10, Institute of Ocean Sciences, Patricia Bay, Sidney, p.1-97.

[27]Najafi, H.S. and Noye, B.J., (1997), *Modelling tides in the Persian Gulf using dynamic nesting*, PhD thesis, University of Adelaide.

[28]Badri, M.A. and Wilders, P., (2012), *Flow estimation for the Persian Gulf using a kelvin wave expansion*. Indian Journal of Geo-Marine Science, Vol.41(3), p.249-258.

[29]Emami, M., Soyuf Jahromi, M., and Behmanzadegan, A., (2019), *Coastline Effect on Tidal Flow Pattern*. Journal of Marine Science and Technology, Vol.18(2), p.12-25. (In Persian)

[30]Moharir, R.V., Khairnar, K. and Paunikar, W.N., (2014), *MIKE 3 as a modeling tool for flow characterization: A review of applications on water bodies. International Journal of Advanced Studies in Computers*, Science and Engineering, Vol.3(3), p.32-43.

[31]Li, P., Li, G., Qiao, L., Chen, X., Shi, J., Gao, F., Wang, N. and Yue, S., (2014), *Modeling the tidal dynamic changes induced by the bridge in Jiaozhou Bay, Qingdao, China*. Continental Shelf Research, Vol.84, p.43-53.

[32]Kaiser, G., Scheele, L., Kortenhaus, A., Løvholt, F., Römer, H. and Leschka, S., (2011), *The influence of land cover roughness on the results of high resolution tsunami inundation modeling*. Natural Hazards and Earth System Sciences, Vol.11(9), p.2521-2540.

[33] Villaret, C., Hervouet, J.M., Kopmann, R., Merkel, U. and Davies, A.G., (2013), *Morphodynamic modeling using the Telemac finite-element system*. Computers and Geosciences, Vol.53, p.105-113.

[34] Kramer, S.C. and Piggott, M.D., (2016), *A correction to the enhanced bottom drag parameterisation of tidal turbines*. Renewable Energy, Vol.92, p.385-396.

[35]Ershadi, S., Arasteh, M. and Tajziehchi, M., (2013), *Numerical Modeling of Flow Pattern Changes in Tidal Inlet of TIYAB Port*, Research Journal of Environmental and Earth Sciences, Vol.5(11), p.691-702.

[36]Peykanpour, P., Bozorgi, M., Moein, M. and Shamaii, A., (2016), *Tidal currents model of Persian Gulf*, IIOABJ, Vol.7(5), p.293-301.

[37]Radfar, S., Panahi, R., Javaherchi, T., Filom, S. and Mazyaki, A.R., (2017), *A comprehensive insight into tidal stream energy farms in Iran*. Renewable and Sustainable Energy Reviews, Vol.79, p.323-338.

[38]UNESCO (1981) *Tenth report of the joint panel on oceanographic tables and standards*. UNESCO Technical Papers in Marine Science, Vol.36, p.1-28.

[39]DHI., (2009), *MIKE 21 & MIKE 3 Flow Model FM Hydrodynamic and Transport Module – Scientific Documentation*, MIKE by DHI, Horsholm, Denmark.

[40]www.boprc.govt.nz

[41]https://erddap.marine.ie

[42]Edalati, S., Ameri, M. and Iranmanesh, M., (2015), *Estimating and modeling monthly mean daily global solar radiation on horizontal surfaces using artificial neural networks in south east of Iran*, Journal of Renewable Energy and Environment, Vol.2 (1), p. 41-47.

[43]The MathWorks Inc., (2016), *MATLAB and Statistics Toolbox 64-bit*, Version 2016a, Release 2016a, Natick, Massachusetts, USA.

[44]Padman, L., and Erofeeva, S., (2005), *Tide Model Driver (TMD) Manual*. Earth and Space Research. Version 1.2. 28 November 2005.

[45]http://polaris.esr.org/ptm_index.html

[46]Nirwansyah, A. W., & Braun, B. (2019), *Mapping impact of tidal flooding on solar salt farming in Northern Java using a hydrodynamic model*. ISPRS International Journal of Geo-Information, Vol.8(10), p.451.

[47] ftp://ftp.oce.orst.edu/dist/tides/regional/PerS.tar.Z

[48] http://volkov.oce.orst.edu/tides/PerS.html

[49] https://tides4fishing.com/as/iran

[50] Khosravi, M., Siadatmousavi, S.M., Vennell, R. and Chegini, V., (2018), *The transverse dynamics of flow in a tidal channel within a greater strait*. Ocean Dynamics, Vol.68(2), p.239-254.

[51] Wood, D. (2006), MIKE BASIN. DHI water and environment, p.1-38.

[52] Soleimani, K., Ketabdari, M.J. and Khorasani, F., (2015), *Feasibility study on tidal and wave energy conversion in Iranian seas*. Sustainable Energy Technologies and Assessments, Vol.11, p.77-86.

[53] Bryden, I.G., Grinsted, T. and Melville, G.T., (2004), *Assessing the potential of a simple tidal channel to deliver useful energy*. Applied Ocean Research, Vol. 26(5), p.198-204.

[54] Bryden, I.G. and Couch, S.J., (2006), *ME1—marine energy extraction: tidal resource analysis*. Renewable Energy, Vol.31(2), p.133-139.

[55] https://voith.com/corp-en/BulbPitS-Turbines_Generators.pdf

[56] 56- JKP Application Development Services, (2016), *Microsoft Office Excel*, 64-bit, Version 2016, Weert, The Netherlands.

INTERNATIONAL JOURNAL OF
COASTAL & OFFSHORE ENGINEERING

IJCOE Vol.6/No.5/ Autumn 2021 (10-22)/ **Special issue of "Marine Renewable Energy"**

Available online at: www. Ijcoe.org

Renewable Energy Production by Microalgae; A review

Matin Khaleghi

Faculty of marine science, Chabahar maritime university, matinkhaleghi@yahoo.com

ARTICLE INFO

Article History:
Received: 21 Jul. 2021
Accepted: 09 Nov. 2021

Keywords:
Microalgae
Biofuel
Greenhouse Gases
Sustainability
Global Warming

ABSTRACT

Biofuels are the up and coming alternative to exhaustible, inenvironmentally and unsafe fossil fuels. Microalgae as a source of biofuels have been widely studied for biodiesel/biogas/biohydrogen/biochar/bioelectricity production and has been gathering much contemplation right away. Increasing in energy demand and in greenhouse gas emission makes it important to develop alternative energy carriers that are renewable, clean and environmentally friendly. The use of arable land for biofuels in some cases has been associated with food insecurities and increased greenhouse gases caused by indirect land use change effects. Microalgae can grow on land not suitable for agriculture and would alleviate these concerns**.** The high lipid and mineral contents of microalgae render it beneficial for the production of biofuels and value-added products. On the other hand, result in to the reducing pollution and protecting the environment, because as a result of generating electricity in fuel cells or mechanical force in blast engines, the only output is water vapor. This review focuses on the current scenario and future prospects of microalgae aimed at biofuel production and the technologies available for converting the biomass produced into biofuel are analyzed. The goal of this work was to give a comprehensive review on biofuel production from microalgae biomass.

1. Introduction

Microalgae are unicellular and multicellular photosynthetic microorganisms that grow rapidly and have highly efficiencient, and their biomass production is 50 times higher than that of fast-growing terrestrial plants [1]. Microalgae are eukaryotic organisms found in almost all ecosystems and are well adapted to a wide range of environmental pressures such as cold, heat, drought, salinity, light oxidation, UV radiation, anaerobic conditions and osmotic pressure [2]. They have low nutritional needs, high growth rate and the ability to accumulate or secrete the right metabolites, which is the main reasons for their biotechnology in the near future [2].

Microalgae have been suggested as good candidates for fuel production because of their higher photosynthetic property, efficiency, higher biomass production, and faster growth compared to other energy crops. Algae contain protein, carbohydrates and lipids. Lipids can be processed to biodiesel, carbohydrates to be ethanol and H_2, and proteins as raw material for biofertilizer. There are many ways to convert the oil and fats into biodiesel, namely transesterification, esterification, blending, micro emulsion and pyrolysis, but transesterification and esterification are the most commonly used methods. Other important factor in biodiesel production is fatty acids (FA) type, and its amount. There are three main type of the FA that can be present in a triglyceride, i.e., saturated, mono-unsaturated and poly-unsaturated with two or three double bonds. The cetane number (CN), kinematic viscosity, density and heating value of biodiesel can be predicted from the FA composition [3].

Microalgae cells are able to convert and store energy instead of using it for growth. Thus, microalgae biomass can be considered as new systems for the production of biofuels that potentially replace fossil fuels due to the renewability, stability and short growth cycle of algae. Biofuels are not only suitable for replacing fossil fuels, but also reduce the concentration of carbon dioxide in the atmosphere [2].

Microalgae are located at the bottom of the aquatic food chain and, as photosynthetic organisms, capture carbon dioxide and water and convert them into organic compounds (such as triglycerides) or electron acceptors (such as molecular hydrogen) with the help of sunlight, which eventually accumulate or precipitate [2].

The lipid and biomass content of microalgae can reach over 80% and 7.3 grams per liter per day of biomass dry weight makes them an ideal candidate for biofuel [4] and lipids can be extracted for biodiesel production from microalgal biomass [5], while the residual/leftover biomass can converted into different liquid and gases biofuel including bio-alcohols through fermentation [6], bio-H_2 through dark fermentation [7], and bio-CH_4 via anaerobic co-digestion [8].

The different microalgae cultivation systems consist of: Open system, Closed system (Photobioreactor), Algal turf scrubber (ATS), Hybrid cultivation system (HCS). The most common methods of harvesting microalgae are gravitational deposition, flocculation, centrifugation, filtration and micro-screening, flotation and electrophoresis technologies. The choice of technology for harvesting depends on the properties of the microalgae [9].

2. Microalgal Biofuels Production

Several characteristics that make microalgae suitable for energy recovery. These include: (i) absence of competition with food supply, (ii) high productivity with reduced cultivation areas (oil yield of about 70% by weight of dried biomass, with area requirement of just 0.1 m^2/year per kg extracted), (iii) growth possibility on areas not suitable for other crops, without subtraction of soil from food crops cultivation, (iv) production in most types of water (fresh, brackish and waste water), with minimal or positive impact on water resources use [10].

The adverse impact of fossil fuel combustion products on the environment and its depletion as non-renewable energy has accelerated the pace of energy transformation in various countries [11, 12, 13].

Among the various types of biomass, algal biomass is highly considered for biofuel production due to higher lipid and sugar content in algal biomass [7, 14, 15]. Microalgal biomass has the potential for production of a broad range of biofuel through different routes. Microalgal biomass can be transformed into biodiesel through the transesterification of lipid [16], bioethanol, bioH_2 through the fermentation of carbohydrates [7, 17], while bio-CH_4 via co-digestion [18].

The use of algal biomass for bio fuels production has many advantages, namely: algal bio-mass can be produced all over the year and have a rapid growth capability, it grows in aqueous media, but it requires less water than terrestrial crops, it can be grown in brackish water on non-arable land, algae cultivation does not need herbicides or pesticides application and the nutrients for algae growth (mainly nitrogen and phosphorus) can be obtained from wastewater, thus as the algae grow, water effluent from agro-industrial sectors are treated. Algae growth does not compete with food production and it improves air quality due to CO_2 bio-fixation, as 1 kg of dry algal biomass uses around 1.83 kg of CO_2. Many species of microalgae have oil content between 20 and 50% dry weight and by changing the growth conditions the oil yield may increase significantly. The thermochemical processes developed for biomass energetic valorization may be also used for algal biomass, having in mind the specificities of this type of biomass. Thermochemical processes are usually divided into dry or conventional and wet or new hydrothermal processes that operate under sub or supercritical conditions [3]. A conceptual model for integrated microalgal biomass and biofuel (biomethane, biodiesel, biohydrogen, and biogas) production is shown in Figure 1 [19].

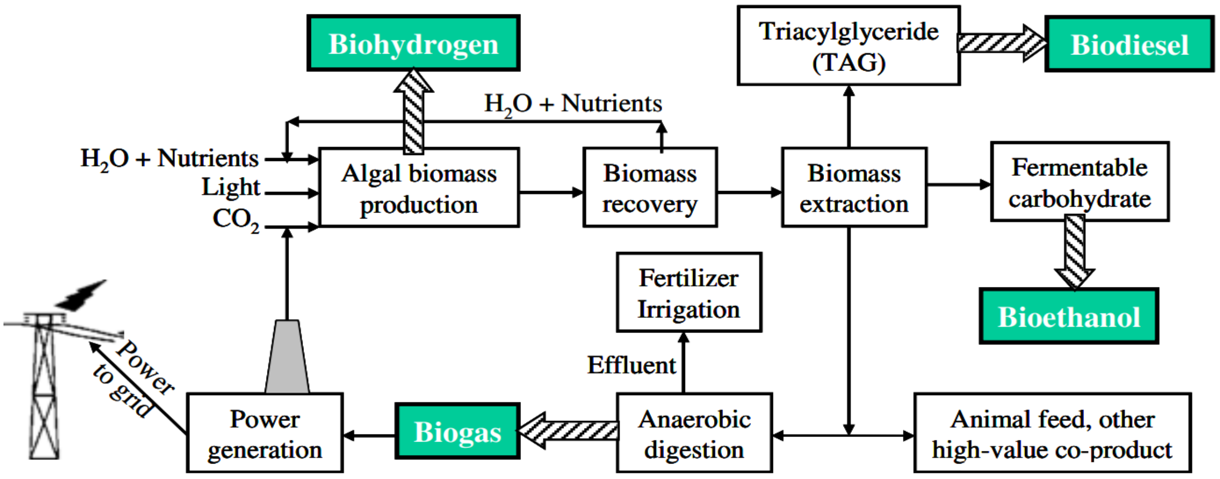

Figure 1. A conceptual model for integrated microalgal biomass and biofuel production.

2.1. Biodiesel

The biodiesel production should involve cell disruption, extraction, and transesterification of the oil to biodiesel. There are several methods for the effective extraction of lipids from microalgae, including autoclave, microwave, sonic and 10% NaCl solution to identify the most effective method of cell degradation [20].

The rapid increasing in the concentration of carbon dioxide in the atmosphere along with the depletion of fossil fuel reserves has led to an increase in attention to renewable fuels. Due to the high biomass production of microalgae, rapid lipid storage in their cells and the ability to survive in saline water have been identified as important food storage for industrial biodiesel production [21]. Among the microalgae that are potentially used as biodiesel biofuels, Chlorelea is the most considered due to its ability to adapt to heterotrophic and phototrophic breeding conditions [4]. Microalgae is able to produce a considerable quantity of lipids in the range of ~5000 to 100,000 L/hector/day, while microalgal derived biodiesel have a high energy content (39 to 41 KJ/g). Table 1 shows oil content of certain microalgae suitable for biodiesel production [19].

Table 1. Oil content of certain microalgae suitable for biodiesel production.

Microalgae	Oil content (% dry wt)	Reference
B. braunii	25–75	Chisti 2007 [62]
Chlorella emersonii	63	Illman et al. 2000 [63]
Chlorella minutissima	57	Illman et al. 2000
C. vulgaris	56.6	Liu et al. 2007
C. vulgaris	40	Illman et al. 2000
C. protothecoides	23	Illman et al. 2000
Chlorella sorokiniana	22	Illman et al. 2000
C. cohnii	20	Chisti 2007
Cylindrotheca sp.	16–37	Chisti 2007
D. primolecta	23	Chisti 2007
Isochrysis sp.	25–33	Chisti 2007
M. salina	>20	Chisti 2007
Monodus subterraneus	39.3	Khozin-Goldberg et al. 2006 [64]
Nannochloris sp.	20–35	Chisti 2007
Nannochloropsis sp.	31–68	Chisti 2007
N. oleoabundans	54	Metting 1996 [65]
N. oleoabundans	35–54	Chisti 2007
Nitzschia laevis	69.1	Chen et al. 2008b
Nitzschia sp.	45–47	Chisti 2007
Parietochloris incise	62	Solovchenko et al. 2009 [66]
P. tricornutum	20–30	Chisti 2007
Schizochytrium sp.	50–77	Chisti 2007
T. sueica	15–23	Chisti 2007
Chlorella sp.	28–32	Chisti 2007

Biodiesel can be produced by direct transesterification with heterogenous/homogenous catalyst or via in-situ(trans)esterification of the microalgal lipids [22].

High lipid efficiency of dominant and rapidly growing algae is one of the main preconditions for commercial production of bio-gasoline from microalgae lipid. Although large amounts of algal biomass are produced under optimal growth conditions, they are relatively low in lipids, while species with high lipids are typically slow-growing. Major advances in this area can be made by inducing lipid biosynthesis, for example, through environmental pressures. There has been a wide range of studies to identify and develop efficient lipid induction techniques in microalgae such as nutrient stress (eg, nitrogen or phosphorus deficiency), osmotic stress, radiation, pH, temperature, heavy metals and other chemicals. In addition, several genetic methods have been developed to increase triglyceride production and inductance [23].

Growth stress conditions can often be used to increase natural lipid formation. This stress was either due to the use of nutrient-deficient breeding cultivation or the addition of excess salt to nutrient-rich cultivation. It seems that the combination of nutrient deficiency and salt enrichment increases lipid formation in *Isochrysis sp.*, but this condition reduces lipid in *Dunaliella salina*. Interestingly, the amount of free glycerol for *Dunaliella sp.* seems to be quite high. *Botryococcus braunii* produces relatively high lipid content in each set of different growth conditions, but the highest value was 54.2% (DW) in nutrient deficiency conditions [3]. Nannochloropis, which grows in nitrogen-deficient cultivations, can increase lipid levels from 28% to more than 50%. Lipid production indicates that a maximum of 150 mg/L per day is achieved when cellular nitrogen reaches 5 to 6%. However, in this study, the initial concentration of nitrogen in the breeding medium reached more than 25 mg/l [3].

Microchloropsis salina (*Monallantus salina*) is able to produce 72% of lipids in nitrogen deficiency conditions. To produce lipids, the percentage of them in microalgae is less important than maximizing growth rate. The result is that nitrogen-deficient cultivation increases lipid production compared to cultures with sufficient nitrogen. High light environments have more lipids than low light environments. In addition, the amount of lipids in culture and lipid production rates indicate that higher amounts of lipids are produced under conditions of sufficient nitrogen and high light, due to greater biomass growth [24].

2.2. Biogas

In the biogas production model, it is assumed that the inflows to the AD are derived from five process steps. These include the vinasse, a by-product in ethanol production; the primary sludge from the wastewater primary treatment stage; the algae residues (lipid-extracted algae (LEA) and the undisrupted algae) from the oil extraction step; the filtered algae in the harvesting section; and crude glycerol, a by-product from the transesterification step in the biodiesel production.

The vinasse from the ethanol production factory was one of the components with a high mass flow rate. Considering the molasses-based distillery effluent, vinasse, as the main component in the anaerobic digestion, the following four reactor configurations were implemented on a commercial scale: a continuous stirred-tank reactor (CSTR), an upflow anaerobic sludge blanket (UASB) reactor, a fixed film/media digester (or anaerobic filter, AF), and a thermophilic digester. The most successful configurations today are the UASB and CSTR reactors. The UASB reactors are used for the treatment of a wide range of industrial wastewaters (from low-to-high-strength wastewater) including vinasse. UASB reactors are being encouraged because of their several advantages including plain design, uncomplicated construction and maintenance, low construction and operating costs, low sludge production, robustness in terms of chemical oxygen demand (COD) removal efficiency and wide applicability, less CO_2 emissions due to less energy requirement, as well as quick biomass recovery [25].

co-digestion of microalgae biomass and primary sludge (PS) enhances 65% CH_4 productivity as well as microcontaminants removal efficiency achieved up to 90%.

During the AcoD process, the produced biogas contains CH_4 (50–65%) and CO_2 (40– 50%) and traces amount of H_2SO_4, N_2O, which need separated from the methane [26]. Therefore, innovative and sustainable biogas upgrading technologies are immediately required. However, there are several traditional upgrading technologies (chemical adsorption, membrane separation, and pressure swing adsorption) available, which demand a high cost [27]. Recently, microalgae-based biogas upgrading are under investigation to avoid the major disadvantages of conventional biogas upgrading [28].

2.3. Biohydrogen

The need to safeguard our planet by reducing carbon dioxide emissions has led to a significant development of research in the field of alternative energy sources. Hydrogen has proved to be the most promising molecule, as a fuel, due to its low environmental impact. Even if various methods already exist for producing hydrogen, most of them are not sustainable [29].

Hydrogen as the cleanest source of energy is a promising alternative to conventional fossil fuels. Among different technologies for hydrogen production, photosynthetic microorganism, such as microalgae, has a great potential to produce hydrogen, by using only water and sunlight, as both clean and cheap sources. Microalgal biohydrogen photoproduction: scaling up challenges and the ways forward [30].

Many algal species show potential to produce hydrogen under certain conditions. Nonetheless, certain technical barriers like developing low-energy methods to harvest microalgal cells, difficulties in continuously producing biomass at a large scale, the presence of invasive species in large-scale ponds, low light penetrance in dense microalgal cultures, and the lack of cost-effective bioenergy carrier extraction techniques, are required to overcome before using microalgae as an economically viable biofuel feedstock [31].

Microalgal hydrogen production is made possible by biological processes directly or indirectly, depending on sunlight, or by fermentation processes and thermochemical technologies for biomass conversion (Figure 2)[29].

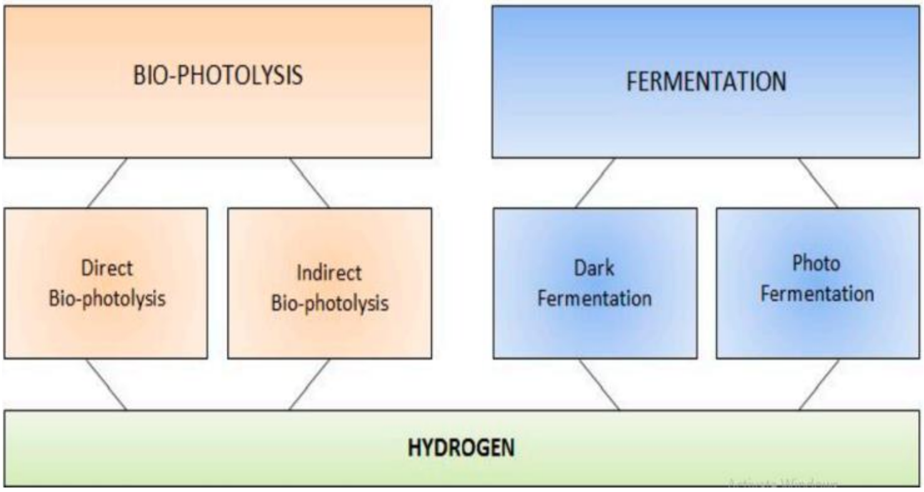

Figure 2. Hydrogen production processes in microalgae.

A large number of unicellular, filamentous, fresh water, and marine cyanobacterial species and strains have been produced large quantity of hydrogen. *Gloeocapsa alpicola*, *Anabaena variabilis*, *Anabaena azollae*, *Arthrospira (Spirulina) platensis*, *Anabaena cylindrica*, Cyanothece, *Nostoc muscorum*, etc. has been produced a high quantity of hydrogen gas. *Anabaena sp.* is produced extraordinarily significant amount of hydrogen. Among them nitrogenstarved cells of *A. cylindrica* produces highest amount of hydrogen (30 ml H_2/lit/h) [19].

Microalgae can produce biohydrogen naturally by light or its biomass can be used as a raw material for fermented biohydrogen.

The pivotal process of microalgal metabolism consists of oxygenic photosynthesis and complex redox reactions that take place at the level of the thylakoid membranes in chloroplasts through two successive phases. During the first light-depending reactions, ATP and reduced NADH, and NADPH, are generated to be involved in the next dark reactions where the atmospheric CO_2 is fixed by a RuBiSco (ribulose-1,5-bisphosphate carboxylase/oxygenase) enzyme to ultimately generate energy rich-carbohydrate stores. Specifically, during the light phase, an electron transport chain is generated along with photosystems II (PSII) via the plastoquinone (PQ) pool, cytochrome b6f complex (Cyt b_6f) and photosystems I (PSI) due to the light energy received as photosystems are associated with light-harvesting complexes I and II (LHC I and LHCII), consisting of numerous photoreceptive pigments. These electrons through PSI leave the electron transport chain and reach the final acceptor ferredoxin (Fd) [32]. In anoxic conditions, Fd is able to address electrons to the hydrogenase enzyme.

This kind of enzyme catalyzes a reversible reaction in which hydrogen can also be split into electrons and protons [29]:

$2H^+ + e^- \leftrightarrow H_2$

In direct photolysis, there is a dissociation of water into hydrogen and oxygen in the presence of light, that is, $H_2O \rightarrow H_2 + ½O_2$. Green microalgae can use light to carry out photosynthesis as they possess chlorophyll a and the photosynthetic systems: Photosystem (PS) II and Photosystem (PS) I, respectively. Disadvantages are the enzyme hydrogenase is very sensitive to oxygen so when a certain amount of oxygen is present, will inhibit hydrogenase activity and will stop it from producing hydrogen. Also, it requires high intensity of light. The advantages include tenfold more solar conversion in green microalgae.

There is two step processes during Indirect photolysis, firstly there is a splitting of water molecules in the presence of sunlight and protons and oxygen is formed. Secondly carbon dioxide fixation occurs storage carbohydrate is being produced, followed by the production of hydrogen gas by hydrogenase.

$12H_2O + 6CO_2 + \text{light energy} \rightarrow C_6H_{12}O_6 + 6O_2$
$C_6H_{12}O_6 + 12H_2O + \text{light energy} \rightarrow 12H_2 + 6CO_2$

Blue-green algae (cyanobacteria) are promising microorganisms for this. Advantages are hydrogen evolution is separated from oxygen evolution. It can also produce relatively higher hydrogen yields. Furthermore, by-products can be efficiently converted to hydrogen. Disadvantages are like significant adenosine triphosphate (ATP) requirement of nitrogenase. Also, this requires continuous light source which is difficult for large scale processes [31]. Furthermore, genetic modification in the bio-H_2ase gene can increase the resistance ability of the hydrogenase enzyme. A different genetic approach used for enhancement of bio-H_2 production in microalgae such as (i) overexpression of PSII gene, cytochrome b_6f, hemA, and lba gene, translational repressor NAB1 protein; (ii) knockout of light-harvesting gene, IFR1 protein, OEE_2 gene; (iii) cloning of pyruvate oxidase gene, DT hydA gene; (iv) antisense transformation of sulp/sulp2 gene or amino acid substitution; (v) insertion of GAL4 gene, CRY1, and CRY2 gene, VP 16 and other light inducible system can enhance the bioH_2 production in microalgae (Figure 3) [7].

INTERNATIONAL JOURNAL OF
COASTAL & OFFSHORE ENGINEERING

IJCOE Vol.6/No.5 /Autumn 2021 (23-31) / **Special issue of "Marine Renewable Energy"**

Available online at: www. Ijcoe.org

Comparison of Horizontal and Vertical axis tidal turbine with a new design to the renewable energy production of marine currents

Mohammad Samadi[1], Madjid Ghodsi Hassanabad[2*], Babak Mozafari[3]

[1] Ph.D. Student, Department of Marine industries, Science and Research Branch, Islamic Azad University, Tehran, Iran. ms.mohammadsamai@gmail.com
[2] Assistant Professor, Department of Marine industries, Science and Research Branch, Islamic Azad University, Tehran, Iran. m.ghodsi@srbiau.ac.ir*
[3] Associate Professor, Department of Power electric, Science and Research Branch, Islamic Azad University, Tehran, Iran. mozafari@srbiau.ac.ir

ARTICLE INFO

Article History:
Received: 18 Aug. 2021
Accepted: 10 Oct. 2021

Keywords:
Renewable energy
Horizontal axis tidal turbine
Vertical axis tidal turbine
New tidal turbine
CFD modeling

ABSTRACT

This study is a new design of a vertical axis turbine that generates renewable energy from low-speed currents tidal. Tidal Energy is one of the most important available resources among the renewable and environmentally friendly energy resources in oceans and seas. Tidal turbines are used to produce renewable energy. Some types of tidal turbines widely used and studied are vertical axis tidal turbines (VATT) such as Savonius, Darrieus, Gorlov, Lucid, etc., in which the flow direction is not essential for them. And some types of tidal turbines are Horizontal axis tidal turbines (HATT) which the flow direction is important and often have good performance than vertical axis turbines. These turbines are well suited for absorption of high-speed current, but most ocean areas have tidal flow at low speed. The main purpose of this research is a numerical study of tidal turbines with a horizontal and vertical axis rotor and designing and modeling VATT to increase the power efficiency in low-speed currents. In numerical modeling, the HATT at high speeds has high efficiency, and C_P to TSR is more than 0.4, but with the design of the vertical Savonius turbine, with the focus of the flow on the concave blade and the removal of force from the convex blade, almost equality in speed Less than 2m/s. In the modern design of the Savonius turbine, the ratio of C_P to TSR has been increased three times and reaches more than 0.3 in compare the simple Savonius classic turbine. Therefore, due to advantages such as easier installation and lower maintenance costs of Savonius turbines, and with the new design, the use of these turbines in renewable energy will be appropriate.

1. Introduction

nowadays, with the reduction of underground resources and fossil fuels, researchers are trying to use clean and renewable energy. The use of renewable energy in addition to economic savings brings good conditions for the environment [1]. One of these sources is the use of current energy generated by the tide. The use of tidal currents is of interest to researchers in the extraction and production of energy because this energy is available intermittently and regularly. This feature of tidal energy is contrary to wind force or solar radiation because it cannot be interrupted due to environmental conditions [2]. The use of tidal currents is of great interest to researchers in the extraction and production of energy because this energy is available intermittently and regularly. This feature of tidal energy is contrary to wind force or solar radiation because it cannot be interrupted due to environmental conditions. The power density of the ocean is about 832 times greater than that of the air, making it potentially a much more efficient energy source [2].

In general, there are various methods for extracting tidal current energy, such as tidal dams, tidal kites, oscillating hydrofoils, and tidal turbines. One of the tidal energy extraction options is hydrofoils and kites with limited installation depth.[3] Research also shows Tidal turbines have less harmful effects on the environment.[4] Therefore, the use of this type of technology (tidal turbines) is much more efficient than other methods of tidal energy extraction. As shown in the below graph, the most commonly used technology is current and wave energy extraction, indicating these energies' importance and superiority. [5]

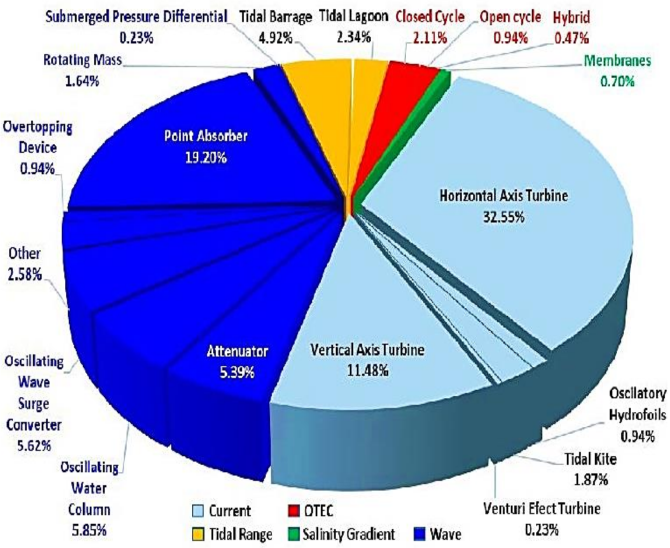

Fig 1. Technology distribution among projects [5]

Nowadays, research, design, and construction of tidal turbines are increasing rapidly. Many places have potential extraction and use of this energy.

Generally, the tidal turbine has two categories, horizontal and vertical. [6] Horizontal axis turbines convert fluid energy into mechanical energy by passing a current through a system of fixed and moving blades. And operates according to the drag system. Horizontal axis turbines are parallel flow turbines that are similar in concept to horizontal axis wind turbines. Vertical axis turbines are the same as horizontal axis turbines, except the vertical axis connects the turbine blades. This indicates the rotation performance of the blades due to the torque caused by the water force inside the blade. These types of turbines operate on the basis of a lift system [7].

Much research has been done on selecting horizontal and vertical axis tidal turbine types. Each of these types of turbines has its unique characteristics. The vertical axis turbine is easier to start and can rotate on both sides [8]. These turbines are also being developed for wind energy extraction and are less expensive to build and easier to install than vertical axis turbines [9]. Another feature of these turbines is that in the marine environment, especially for hydrokinetic applications, the equipment is exposed to water. As an electrical component, the generator needs to be sealed, so this becomes one challenge. In a horizontal axis turbine, gear and generator must be placed underwater.

In contrast to a vertical-axis turbine, the generator can be coupled to one end of the shaft. So, it can be placed on top and at one end of the shaft. So, it can be placed on top and reduce the cost of arranging water-sealed technology [10].

The equipment is exposed to water in the marine environment, especially for hydrokinetic applications. As an electrical component, the generator needs to be sealed, which has become one challenge. In a horizontal axis turbine, gear and generator must be placed underwater.

On the other hand, the most critical challenges of vertical axis turbines, compared to horizontal axis turbines, can be mentioned as follows:

Irregular current velocity: Irregular current velocity is a typical challenge for all hydrokinetic turbine types. The current movements of seawater are dominantly driven by changing tides. Tides have predictable velocity according to tide time or ebb time. However, tidal currents velocity are irregular and fluctuate depending on location and specific time. [11]

Fatigue loading: The variation of radial force can effect on shaft or bearing. The closest effect is friction on the bearing, and the other impact is broken in the shaft. It happened experimentally in towing tank Shaft cannot resist fluctuation force with a big peak.

Vibration: The variation of radial force also can effect the supporting structure and other equipment. It is known as vibration. Some components like the generator are susceptible to vibration. On the other hand, if this vibration frequency coincides with the natural frequency of the support structure, it can be destructive. [12].

Cavitation: Cavitation is always to be a challenge in the hydrokinetic turbine. It can be defined as the formation of water bubble or voids when the local pressure falls below the vapor pressure. Slowly it can damage turbine material. Rough blade surface will decrease the performance. [12].

A tidal current turbine rated at 2–3 m/s in seawater can results in four times as much energy per year/m2 of rotor swept area as similarly rated power wind turbine. Although accessing tidal stream energy may be costly, the high energy availability if exploited will more than compensate for the higher costs as a result, the use of this energy is useful and practical and research on the performance of tidal turbines is important.

According to the advantages and disadvantages of tidal turbines, There are many types of research about the modeling of tidal turbines and the new designs of them in both horizontal and vertical axis types to increase efficiency, angular velocity, and output power of the turbines.

For example, Nachtane et al. (2020) studied the hydrofoil designs of horizontal axis tidal current from the technology development point of view. Also, the newest marine tidal current turbine technologies and its historical development were reviewed. Besides, they reviewed CFD models used to investigate the performance of tidal turbines and their optimization methods [13]. Gaurav and Prasad Saini (2019) studied the several rotor configurations of the vertical axis hydrokinetic turbines (VAHT). This research help researchers in selecting, performance-enhancing, and design optimizing the design of cross-flow hydrokinetic turbines [8]. Qian et al. (2019) reviewed the control methods and configuration of tidal turbines, with a focus on horizontal axis tidal turbines [14]. Li et al. (2016) present a review of the technological developments of the tidal turbine blade structure and hydrodynamics design. Subsequently, the key technologies to be researched for the tidal current turbine blade design were concluded and forecasted [15].

Many tidal turbines broadly studied and used are vertical axis tidal turbines such as Darrieus, Gorlov, Savonius, Lucid, etc., which work in any flow direction.

In another study, Payambourpour et al. (2020) investigated a turbine with a flow deflector as a laboratory and numerical analysis. The studied turbine has 2 blades with a large number of semicircles with different diameters and an axis perpendicular to the flow direction. In this study, the researchers examined various parameters. Finally, they evaluated the turbine's efficiency, and as a result, the best deflection criteria obtained the collision current with the turbine to produce more efficiency. [16].

Gorle et al. (2019) introduced a method based on kinematic relations in the Darrieus turbine [17].

Kerikous and Thevenin (2019) improved the blade profile of a water current Savonius turbine for maximizing the output power of the turbine with a particular thick blade. They introduced 12 geometrical terms to shape optimization. Their optimum blade leads to considerably higher efficiency than common blades in Savonius turbines [18].

Elbatran et al. (2017) presented a new system for increasing the turbine efficiency with a ducted nozzle around Savonius rotor (6 different duct nozzle designs). Their design increased the maximum power coefficient by 78% compared to the commonly modified rotors [19].

Derakhshan et al. (2017) introduced a movable blade VATT and studied it numerically and experimentally. They achieved higher efficiency with their new design [20].

In this research, horizontal axis and VAT of Savonius type are modeled under the same conditions, and their output power results are compared. Then, the obtained results are compared with the newly designed Savonius turbine, and the results of each Will be examined.

In this research, a Savonius turbine has been designed that has the ability to generate energy in low tidal currents. Most Savonius turbines can’t produce good energy, but, with the changes in the turbine, the conditions for energy production for this model of the turbine have been provided. The performance of the designed turbine will be evaluated using numerical modeling. And the results will be discussed

2. Material and method

For modeling, it should be noted that the height of the turbine installation, temperature changes and water salinity, viscosity effect, the effect of disturbances in the course of all of the influential parameters in the turbine production energy [6] hence all the influential variables in the model It is considered the same.

In the Horizontal axis of one blade and two blades, according to the deviation and torque of swing, they produce significant alternate load. Rotors with more than two blades, rotor moment during a rotor rotation round, almost completely in general balance. Therefore, the horizontal axis of the 3 blade and the Airfoil in the design are used. In the design of the horizontal turbine, the choice of a profile in the form of Airfoil should have important criteria.

The profile should have a high lift coefficient, while keeping the drag coefficient low. As a result, the coefficient of C_L/C_D should have a high value before the pre-design of the blade should be examined for the selective profile. The production of blades should be easy and began to resist environmental conditions.

Also, the selected profile should be effective for the stability of the blade against the accumulation of marine and dirty plants .[21]

The optimal tip speed ratio depends on the number of turbine rotor blades. The smaller number of blades, the turbine should rotate faster than the maximum capable. The optimal tip speed ratio is obtained depending on the number of rotor blades.

$$\lambda_{OPT} = \frac{4\pi}{n} \tag{1}$$

In the above relationship, n number of rotor blades.

By applying the momentum theory of Betts and the strip's theory, the blade form's optimal form can be calculated. If producing a coefficient of lift and local length, follow a hyperbolic pathway during the blade radius, the flow rate of flow on the plate is not high, and the coefficient of the lift in its highest value is noted. In calculating the amount of chord on the airfoil, the mechanical power of the rotor from the wind flow or water is affected by the geometric form of rotor blades. With certain simplification and by ignoring the profile of the blade profile and tip vortices, a mathematical formula that can be solved analytically can result in the optimal aerodynamic distribution during the blade:

$$C_{Opt} = \frac{2\pi r}{Z} \frac{8}{9C_L} \frac{v_{WD}}{\lambda v_r} \tag{2}$$

In the above formula, the optimum local length of the blade in meters C_{opt}, design flow speed in meters per second, v_{WD}, local effective flow velocity in meters per second, $v_r = \sqrt{v_w^2 + u^2}$, peripheral speed Meters per second, u, local tip speed ratio, λ, local distribution coefficient, C_L, local length of blade, r, the number of rotor blades, Z, are.

Many studies have been investigated in terms of a variety of horizontal turbine airfoils, and their various characteristics are discussed. This study uses a horizontal axis turbine expression to use airfoil Naca 63-415 because it has good aerodynamic properties. Also, the naca63 airfoil series has a lot of time and less sensitivity to roughness and friction compared to other airfoils. [22]

In the vertical turbine modeling, the conventional Savnious turbine, which includes two half-cylindrical sections, will be modeled. The turbine, which has been proven to be a shaft, absorbs a portion of flow due to the collision of flow, and another part prefers to move in the opposite direction.

In the CFD modeling, Flow3D software is used. This software uses the first and second-order accuracy methods in solving equations

2.1. Theoretical consideration

The rules governing the flow of an incompressible fluid, expressed by the continuity equations and the size of the motion in the coordinate axes known as the equations of Navier Stokes, represent the sustainability of mass and size of movement to mathematical expression. If the fluid element is considered a constant volume in the computational atmosphere,

in this case, the forces of which and the principle of survival of the mass in this element are represented as partial derivative equations .

$$\frac{\partial \mathrm{u}_i}{\partial \mathrm{x}_i} = 0 \tag{3}$$

$$\frac{\partial \mathrm{u}_i}{\partial_i} + u_i \frac{\partial \mathrm{u}_i}{\partial \mathrm{x}_i} = \frac{-1}{\rho}\frac{\partial \mathrm{p}}{\partial \mathrm{x}_i} + \mathrm{g}_\mathrm{i} + v\nabla^2 u_i \tag{4}$$

In the relationships expressed Ui, the instantaneous speed component in the direction of i (m/s), V dynamic fluid (Ns/m^2), ρ density fluid (kg/m^3), g gear acceleration component in the order i (m/s^2), And P pressure at any point of the fluid. In the CFD modeling, the equations governing the non-density flow are expressed as the following relationships [23]

$$\frac{\partial}{\partial \mathrm{x}}(uA_x) + \frac{\partial}{\partial \mathrm{y}}(vA_y) + \frac{\partial}{\partial \mathrm{z}}(wA_z) = 0 \tag{5}$$

$$\frac{\partial \mathrm{u}_i}{\partial \mathrm{t}} + \frac{1}{V_F}\left(u_i A_{i1} \frac{\partial \mathrm{u}_i}{\partial \mathrm{x}_i}\right) = \frac{1}{\rho}\frac{\partial \mathrm{p}}{\partial \mathrm{x}_i} + \mathrm{g}_i + f_i \tag{6}$$

In the relationships expressed 5 and 6 u,v,w, fluid velocity components in the direction of x,y,z (m/s), V$_\mathrm{F}$ Volume fraction of Chase (m^3), A$_x$, A$_y$, A$_z$ Surface in the direction of x,y,z (m^2), ρ density (kg/m^3), P pressure at any point of fluid (Pa), g$_\mathrm{i}$ accelerated gravity component in the direction of i (m/s^2) and fi represents Reynolds stress (Pa).

2.2. Turbulence modeling

Researchers develop much disturbed models to simulate turbulent currents. The number of differential equations used for disturbing quantities to different categories, including alternate models, single equation models, second model models, models It has a tension equation and large vortex simulation, models. The simulation of turmoil in the Flow-3D modeling software using one of the five models of parental mixing length, a kinetic energy equation, the two equivalents of the K-ε model of the groups and the simulation model of large facial vortices It takes

The momentum and continuity equations with k-ε turbulence model are the governing equations of this study which are used to CFD simulation [24] with the volume of fluid (VoF) model for simulating free-surface flow according to the following equations [25].

$$V_f \frac{\partial \rho}{\partial t} + \frac{\partial}{\partial x}(\rho u A_x) + \frac{\partial}{\partial y}(\rho v A_y) + \frac{\partial}{\partial z}(\rho w A_z) = 0 \tag{7}$$

Momentum equations for the fluid velocity components (u,v,w) in the three coordinate directions:

$$\frac{\partial u}{\partial t} + \frac{1}{V_f}\left\{uA_x \frac{\partial u}{\partial x} + vA_y \frac{\partial u}{\partial y} + wA_z \frac{\partial u}{\partial z}\right\} = -\frac{1}{\rho}\frac{\partial P}{\partial x} + G_x + f_x \tag{8}$$

$$\frac{\partial v}{\partial t} + \frac{1}{V_f}\left\{uA_x \frac{\partial v}{\partial x} + vA_y \frac{\partial v}{\partial y} + wA_z \frac{\partial v}{\partial z}\right\} = -\frac{1}{\rho}\frac{\partial P}{\partial y} + G_y + f_y \tag{9}$$

$$\frac{\partial k_T}{\partial t} + \frac{1}{V_f}\left\{uA_x \frac{\partial k_T}{\partial x} + uA_y \frac{\partial k_T}{\partial y} + wA_z \frac{\partial k_T}{\partial z}\right\} = P_T + G_T + Diff K_T - \varepsilon_T \tag{10}$$

Turbulence transport equation in the three coordinate directions:

$$\frac{\partial k_T}{\partial t} + \frac{1}{V_f}\left\{uA_x \frac{\partial k_T}{\partial x} + uA_y \frac{\partial k_T}{\partial y} + wA_z \frac{\partial k_T}{\partial z}\right\} = P_T + G_T + Diff K_T - \varepsilon_T \tag{11}$$

Where P is the pressure, V_f Is the open volume fraction of the flow, ρ is the fluid density, and the components of velocity (u, v, w) are in the directions about x, y, and z. A_x, A_y and A_z are the open surface fraction in the x, y, and z directions. K_T, P_T, G_T, Diff K_T, and ε_T are turbulent velocity fluctuations in the flow, the turbulent kinetic energy, the buoyancy production term, diffusion term, and the turbulent energy dissipation rate, respectively.

To evaluate the efficiency and output power of turbines from dimensionless coefficients, power factor (Cp) and blade tip speed ratio (TSR) is introduced as the ratio of blade tip speed to free flow velocity. The mentioned coefficients are introduced below. [6]

$$C_P = \frac{P_{rotor}}{P_{available}} + f_x \tag{12}$$

Where P_{rotor} and $P_{available}$ are the power generated by the rotor (W) and incident flow power passes from the cross-section area of the turbine, respectively. $P_{available}$ is obtained as follows:

$$P_{available} = \frac{1}{2}\rho A U^3 \tag{13}$$

In which U and ρ are the free stream speed (m/s) and fluid density (kg/m^3), respectively.

$$TSR = \frac{R\omega}{U} \tag{14}$$

ω is the rotational speed of the rotor (rad/s), and R is the radius of the turbine rotor (m). Therefore, the last power that can be exploited is obtained as:

$$P_{rotor} = \frac{1}{2} C_P \rho A U^3 \tag{15}$$

3. Verification of the model

To ensure the accuracy of the modeling process and control the software outputs, the articles Bhuyan and Biswas have been used. Due to the laboratory and numerical model of this research and the design of a new hybrid turbine model, this research has been used for validation. In that research, a Savonius Hybrid Turbine is in the below table. It was investigated in two cases, laboratory and numerical. [26]

Table 1. Turbine's parameters Bhuyan and Biswas [26]

Parameter	**Dimensions**
Dimensions of H rotor	
Blade profile	NREL S818
Number of blades	3 (120° apart)
Blade chord length	0.1 m
Blade height	0.3 m
Diameter of H-rotor	0.3 m
Dimensions of Savonius rotor	
No. of Savonius blades	2
Height	0.25m
Diameter	0.08m
Thickness	0.005m

According to the specification provided in Table 1, first, the turbine is modeled in solid work software and then the model designed in numerical modeling software.

Figure 2, a show the experimental model of the Biswas and figure b and c represents turbine modeling

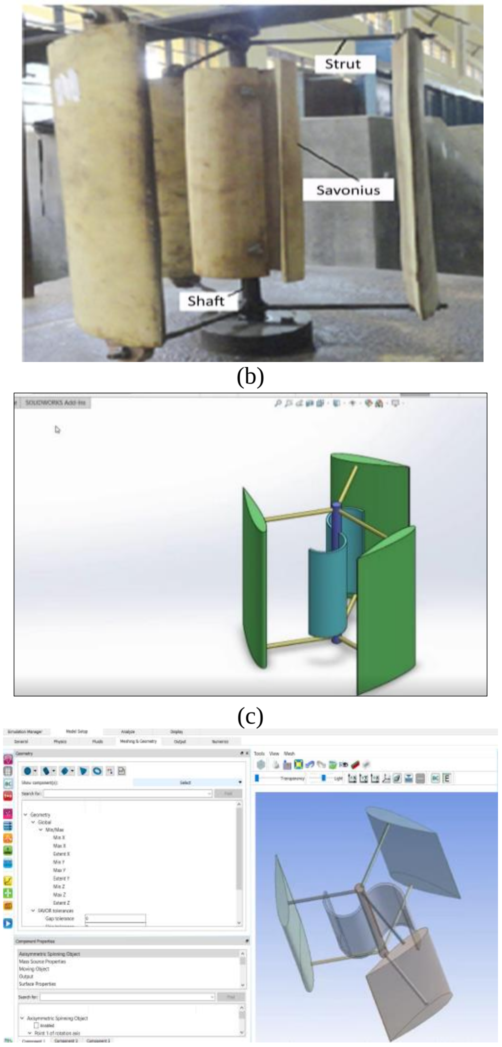

(a)

(b)

(c)

Fig 2. a: Bhuyan and Biswas laboratory turbine, b: design turbine in solid work, c: analysis model in software

Based on the figure shown in Fig 3, the values obtained from the proportion of torque coefficient to TSR have a good matching; therefore, the classical Savonius turbines and new design Savonius turbine and horizontal turbine are modeled and analyzed.

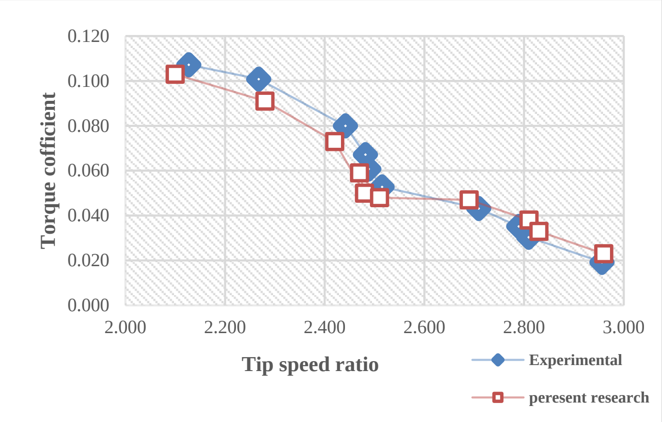

Fig 3. Comparison of the experimental and numerical model

4. Turbine model

In this section of research, Turbine modeling is done.

4.1. Simple Savonius turbine

The turbine model of this study is shown in Fig. 4, and Table 2 shows the quantities of parameters of that turbine. The overlap coefficient of the blades is defined by the following equation effects on the turbine's performance. Yaakob et al. show that the maximum turbine power coefficient relationship is obtained at β of between 0.2 and 0.25 [27]. Hence, this ratio in this study was selected at 0.23 approximately.

$$\beta = \frac{e}{d} \tag{16}$$

Table 2. Dimensions of turbine used in CFD simulation

Specification	Input Data
Rotor diameter	3.00 m
Turbine height	3.00 m
Hub diameter	0.80 m
thickness of blades	0.30 m
Overlap ratio	0.22

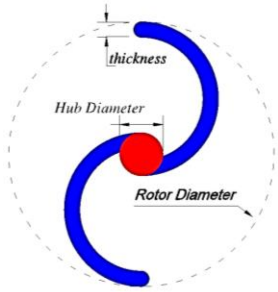

Fig 4. Schematic top view of simple savonius turbine

4.2. Horizontal turbine

The horizontal turbine model was used to model three blades with Airfoil Naka 43-415. To prevent long time and computational space are avoided by modeling the turbine body. Also, for the same modeling conditions, the surface of the fluid surface is identical in both turbines. Therefore, in modeling, the turbine characteristics are following Table 3.

Table 3. Dimensions of horizontal turbine used in CFD simulation

Specification	Input Data
Rotor diameter (d)	3.65
thickness of blades(m)	3 Blades-Airfoil Naka 43-415

Fig. 5: Airfoil Naka63-415

4.3. New Savonius turbine

The blades used in this research are designed inspired by the study blades of Tian et al. [28]. The turbine design of this study with its obstacles is shown in Fig. 6, and Table 4 shows the quantities of parameters of that turbine and its obstacles.

Table 4. Dimensions of turbine and its obstacles used in CFD simulation

Specification	Input Data
Rotor diameter	3.00 m
Obstacle diameter	2.20 m
Hub diameter	0.80 m
Turbine and obstacles height	3.00 m
Maximum thickness of blades and obstacle	0.3 m
Minimum thickness of blades and obstacle	0.10 m
Overlap ratio	0.22

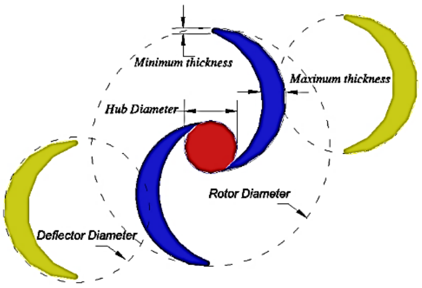

Fig 6. Schematic top view of turbine and obstacles

5. Results and Discussion

CFD simulation was done for four models (simple savonius turbine, horizontal turbine, new savnious turbine and Savonius Hybrid Turbine that had been done modeling for validation) in Constant and identical inlet current velocity. Computational fluid dynamics is a branch of fluid mechanics that uses numerical analyses to solve problem involving fluid flows. Computational Fluid Dynamics (CFD) is a computer solution of the governing equations for fluid flows (the conservation of mass, momentum, and energy) in up to three dimensions. This research has used Flow-3D software for CFD. FLOW-3D provides a complete and versatile CFD simulation platform for engineers investigating the dynamic behavior of liquids and gas in a wide range of industrial applications and physical processes.

FLOW-3D focuses on the free surface and multi-phase applications, serving a broad range of industries, including microfluidics, bio-medical devices, civil water infrastructure, aerospace, consumer products, additive manufacturing, and inkjet printing, laser welding, automotive, offshore, energy, and automotive.

The boundary condition and solution domain are the same selected. Fig. 7 shows the two and 3D time frames of CFD models.

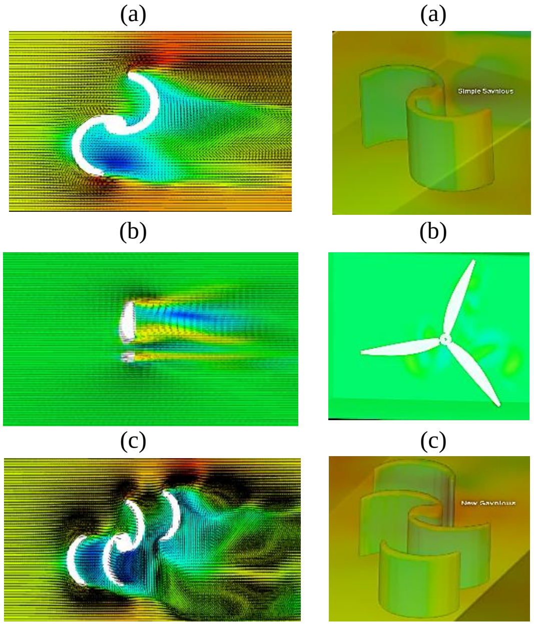

Fig 7. 3D view of the turbine a: simple savonius b: horizontal c: new savonius

In the modeling performed, C_p-TSR ratio is displayed in the following graphs. It is observed new turbine design savonius had low slippage than the horizontal turbine when the current velocity below 2m/s. In continuing with raise the current speed, the ability both Savonius turbine decreased. This is important, mostly, sea current is accompanied low speed, so use of horizontal turbine at the low velocity isn't a good choice.

One of the reasons for raising C_p-TSR in the horizontal turbine is turbine area motion. Obviously, with increasing the diameter of the Savonius turbine, the turbine efficiency will be high.

The considerable results of modeling show that C_P has an upward trend by increasing the speed of water flow in the Simple savonius turbine. However, C_P has an upward trend till 2m/s current speed and after that unexpectedly, has a downward trend in rotors with a new turbine.

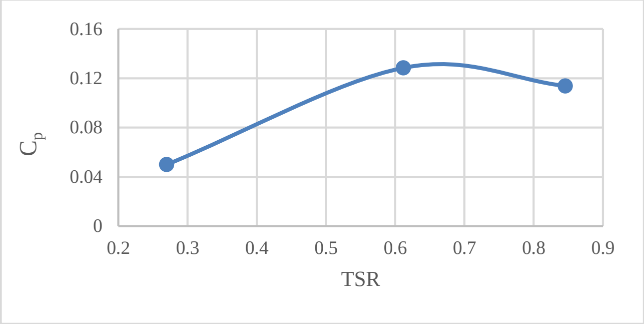

Fig 8. Cp-TSR Classic Savonius Turbine

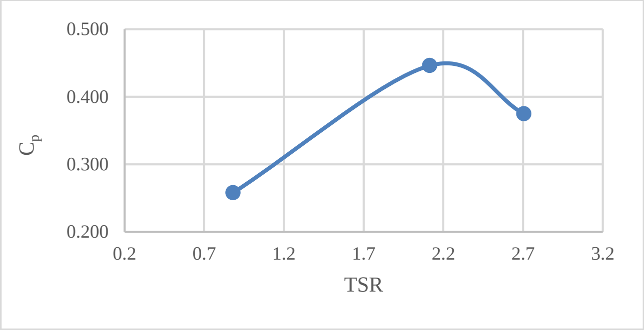

Fig 9. Cp-TSR New design Savonius Turbine

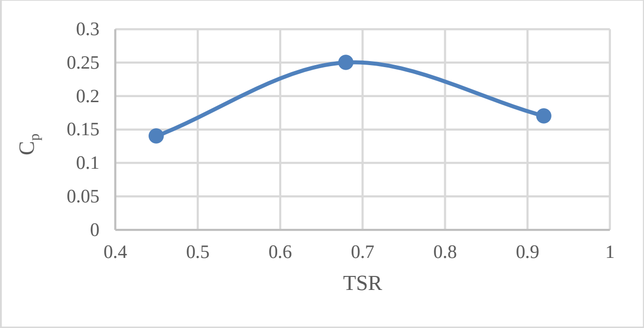

Fig. 10: Cp-TSR Hybrid H-Savonius Turbine

In the modeling performed, the C_p-current velocity ratio and power-current velocity ratio are displayed in the following graphs. It is observed new turbine design savonius had low slippage than the horizontal turbine when the current velocity was below 2m/s.

This issue is vital because marine currents often have low velocity. And since savonius turbine has fewer installation costs and the ability to rotate from both sides, it has suitable conditions for exploitation. And the other hand, the process of changes in two other turbines indicates a significant difference at high speeds that represents the horizontal turbine is better than the vertical turbine.

With consideration, the power graph can be concluded that the design of new turbines and the use of combined turbines will increase the turbine efficiency. So in Table 5, the amounts of the obtained capabilities are displayed and well-increasing the power of combined turbines compared to the simple Savonius turbine. The amount of turbine designed at a speed of 1m/s is almost equal to the horizontal turbine and drops 40% at speeds of 2m/s. In other words, it can be concluded from Table 5 that at low flow velocities, a good power can be achieved by selecting a designed Savonius turbine. And due to the low cost of installation and operation of this turbine, it is a more suitable choice than the horizontal axis turbine. On the other hand, as the flow rate increases, the ability of the horizontal axis turbine is well increased, so it can be concluded that turbines designed for high-speed flows are not suitable.

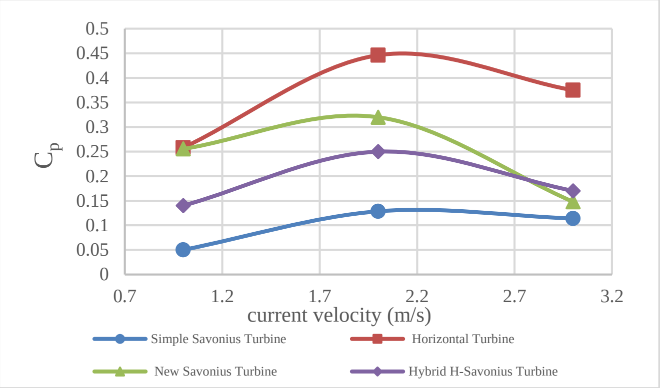

Fig. 11: C_P-current velocity ratio

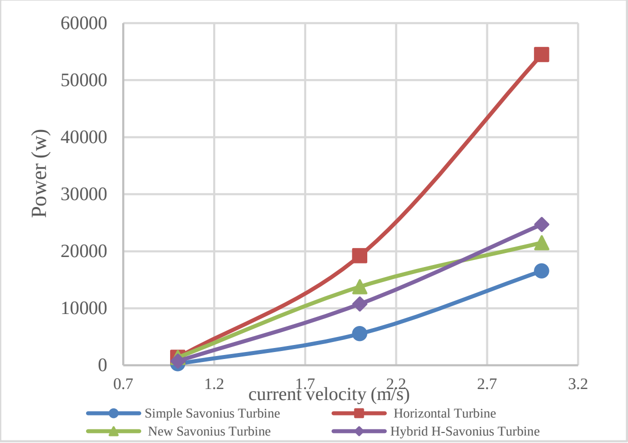

Fig. 12: Power-current velocity ratio

Table 5. Power Amounts

Turbine	Simple Savonius	Horizontal	New Savonius	Hybrid H-Savonius
Power in velocity= 1m/s	269	1388	1375	754
Power in velocity= 2m/s	5530	19209	13776	10763

6. Conclusions

The typical tidal turbine can absorb the tidal flow of the ocean at a relatively high speed. But some areas with the tidal flow are low speed. VATT, due to its low power coefficient, is not popular, while they have got less cost installation and have a good situation for maintenance. If this power increases, this turbine will be suitable for energy extraction. Using CFD modeling and designing a new turbine in this study has increased the ratio of Cp to TSR. The base of this design was focused on the current blade and the removal force from the convex blade. Simple Savonius turbines are not suitable for water currents less than 2m/s at all. Putting the semi-cylinder barriers as a manner in the turbine, front and back of the Savonius rotor, has a significant increase in the output performance. According to the obstacle that has been designed in this research, the result has shown that the power has risen to 2.50 times.

Also observed from numerical modeling, hybrid turbines and new VATT have increased their power near to HATT's performance

7. Reference

[1] Lawn, C. J., (2009), Technologies for Tomorrow Electric Power Generation, Journal of Mechanical Engineering Science. Vol. 223

[2] Neill, S. and Hashemi M, Reza., (2018), Fundamentals of Ocean Renewable Energy, Since direct.

[3] Roberts, B., Thomas, P., Sewell, Z., Khan, S., Balmain, Z. and Khan, J. G., (2016), Current tidal power technologies and their suitability for applications in coastal and marine areas, Ocean engineer, Vol.2, p. 227- 245.

[4] Ketabdari, M j. and Solymani, Kaveh., (1394), Types of energy extraction methods of wave and tidal and effect on sea environmental, 2th International Offshore Industries Conference, Tehran.

[5] Shadman, M, Silva, C., Faller, D. and Wu, Z., (2019), Ocean Renewable Energy Potential, Technologyand Deployments a Case Study of Brazil, energies, Vol.12.

[6] Samadi, M., Ghodsi, M.H. nad Mozafari, B., (2019), Energy production potential of Qeshm channel tidal current extraction with CFD modeling of a tidal turbine, 8th International Conference, Tehran, sanatisharif university, Vol.8.

[7] Kadiri,M., Ahmadian, R., Bockelmann-Evans, B., Rauen, W. and Falconer, R., (2012), A review of the potential water quality impacts of tidal renewable energy systems, Renewable and sustainable energy reviews, Vol 16(1), p. 329-341

[8] Saini, G. and Prasad Saini, R P., (2019), A review on technology, configurations, and performance of cross-flow hydrokinetic turbines, Energy research, Vol.41, p. 79-88.

[9] Pallotta, A., Pietrogiacomi, D. and Romano, G.P., (2019), HYBRI - A combined Savonius-Darrieus wind turbine: Performances and flow fields, Energy, Vol.116, p.433-452

[10] Khan, M. J., Bhuyan, G., Iqbal, M.T. and Quaicoe, J.E., (2009), Hydrokinetic energy conversion systems and assessment of horizontal and vertical axis turbines for river and tidal applications: A technology status review, Applied Energy Vol.86, p.1823–1835.

[11] Satrio, Dendy., Pria Utama, IKA and Mokhatasor., (2016), Vertical Axis Tidal Current Turbine

Advantages and Challenges Review, Proceeding of Ocean, Mechanical and Aerospace, Vol.3, p. 64-71.

[12] Libii, J.N., (2013), Comparing the calculated coefficients of performance of a class of wind turbines that produce power between 330 kW and 7,500 kW, World Transactions on Engineering and Technology Education, Vol.11, p. 36-40.

[13] Nachtane, M., Tarfaoui, M., Goda, I. and Rouway, M., (2020), A review on the technologies, design considerations and numerical models of tidal current turbines, Renew energy, Vol. 157, p.127-164.

[14] Qian, P., Feng, B.H., Liu, X., Tian, Y. and Zhang, D., (2019), Review on configuration and control methods of tidal current turbines, Renew and Sustainable. Energy, Vol.108, p. 125-139.

[15] Zhou, W., Li, H., Liu, H., Lin, Y., Xu, Q., (2016), Review on the blade design technologies of tidal current turbine, Renewable and sustainable. Energy. reviews, Vol.63, p. 414-422.

[16] Payambarpour Abdolkarim S.A., Najafi, F. and Magagnato, F., (2020), Investigation of deflector geometry and turbine aspect ratio effect on 3D modified in-pipe hydro Savonius turbine: Parametric study, Renew. Energy, Vol.148, p. 44-59

[17] Gorle, J.M.R., Chatellier, L. and F. Pons., (2019), Modulated circulation control around the blades of a vertical axis hydrokinetic turbine for flow control and improved performance, Renewable and sustainable. Energy. reviews V.105, p. 363-377.

[18] Kerikous, E., and Thevenin, D., (2019), Optimal shape of thick blades for a hydraulic Savonius turbine, Renew. energy V.134, p. 629-638.

[19] Elbatran, A.H, Ahmed Y. M and Shehata, A.S., (2018), Performance study of ducted nozzle Savonius water turbine, comparison with conventional Savonius turbine, Energy, Vol.114, p. 566-584.

[20] Derakhshani, S., Ashori M. and Salemi., (2017), Experimental and numerical study of a vertical axis tidal turbine performance, Ocean Enginer, Vol.137, p. 59-67.

[21] Edon, M., (2007), 38-meter wind turbine blade design, Internship Report. Universite of Savoie.

[22] Chen, C.C, Choi, Y.D. and Yoon, H Y., (2013), Blade design and performance analysis on the horizontal axis tidal current turbine for low water level channel, 6th conference on Pumps and Fans with Compressors and Wind Turbines.

[23] Ghasemzadeh, F. 2013. Simulation of hydraulic problems in Flow-3D (2th Ed.), Noavar Press, Tehran, Iran.

[24] White, F.M, (2008), Fluid mechanics, publish, Mc graw hill education.

[25] Alizadeh, H., Jahangir, MH and ghasempour, R., (2020), CFD-based improvement of Savonius type hydrokinetic turbine using optimized barrier at the low-speed flows, Ocean engineering Vol.202, p. 171-178.

[26] Bhuyan, S. and Biswas, A., (2014), Investigations on self-starting and performance characteristics of simple H and hybrid H-Savonius vertical axis wind rotors, energy converstion and manegment, Vol.87, p. 859-867.

[27] Bin Yaakob, O., Tawi, KB and Suprayogi Sunanto, D.T., (2010), Computer Simulation Studies on the Effect Overlap Ratio for Savonius Type Vertical Axis Marine Current Turbine, IJE Transactions A: Basics, Vol. 23, p. 79-88.

[28] Tian, W., Zhaoyong, M., Zhang, B. and Li, Y., (2018), Shape optimization of a Savonius wind rotor with different convex and concave sides, Renewable Energy, Vol. 117, p. 287-299.

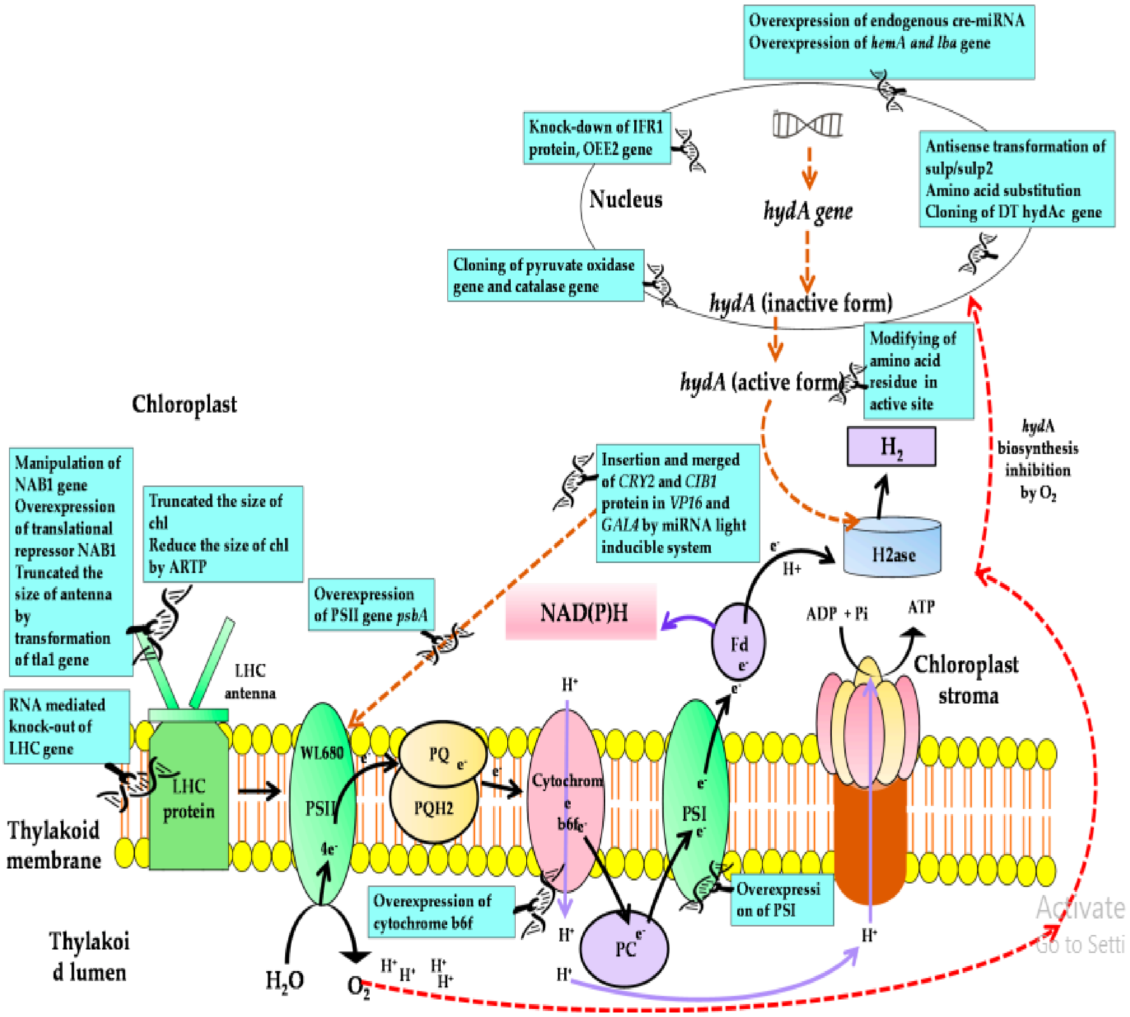

Figure 3. A different genetic approach used for enhancement of bio-H_2 production in microalgae.

2.4. Bioelectricity

One energy from aquatic herbs which is potential to be developed, eco-friendly, and competitive is microalgae. The potency of microalgae development is important in the future since microalgae have preeminence as food material, supplement, biodiesel, and bioethanol. It can also be utilized as the electricity producer. Microalgae-Microbial Fuel Cell (MMFC) technology utilizes the result of microalgae photosynthesis as an oxygen in the cathode with the tapioca wastewater as the anode to produce bioelectricity. The power density value was calculated based on the influence of the wide of electrode surface and the membrane circle. The wide of the electrode surface and the membrane circle was calculated by following equation:

$$P = V \times I \tag{1}$$

where P is power density (W), I is Current (A), and V is Voltage (V).

Power density can be influenced by the wide of electrode surface and membrane, so the equation is:

$$P = V \times t / A_{Total} \tag{2}$$

Tools that are used in MMFC technology are based on modified. MMFC tools design is based on the microbial fuel cell research, namely electrode and membrane usage type of substrate, the reactor design [33].

Microbial fuel cell is a technology that utilizes microbes to produce energy in the form of electricity. Microbes convert various kinds of organic compounds into CO_2, water, and energy. Recently, one of MFC technologies developed is MMFC (Microalgae Microbial Fuel Cell) technology. MMFC is an alternative that be used as a source of electricity generator through hydrolysis and fermentation of microalgae in one process unit. MMFC consists of an anode and cathode that connected through a load (usually a resistor). Anode chamber is containing microorganism cultures that catalyses the composition of organic materials into electrons and protons. Power will be produced by the reduction of oxygen or other compounds at the cathode chamber. On the operation of MFC, electrogene which will produce CO_2. Microalgae in the cathode chamber use CO_2 as a carbon source for growth [34].

These are the greenest and most sustainable types of fuel cells, and undoubtedly represent the future of energy production. MFCs can be double-chambered, with separated anodes and cathodes, or single-chambered, having the electrodes in the same container

[35]. In both cases, they exploit microorganisms and their metabolism to produce the fuel necessary for the fuel cell to function. Most MFCs are mixed, using anode bacterial cultures for hydrogen production and cathode microalgae strains for oxygen supply [36]. However, prototypes of fuel cells that work only with algal strains are in development [37]. MFCs have significant environmental benefits. Thanks to the biological processes underlying their functioning, they can combine energy production with other functions, such as bioremediation activities [38, 39]. It also bypasses the hydrogen storage limitation, since hydrogen is produced and utilized almost at the same time in the anodic chamber. However, this technology is not yet widely applied due to high costs and ineffective yields, which require further study for improvement [40]. Some recent investigation suggested that the integration of MB-MFCs system with microalgal based bioH_2 production are a cost-effective approach for wastewater treatment and bioH_2 production. In this system, wastewater is used as nutrient rich substrates for bacterial growth, the bacteria oxidize the substrates and generates H+ and e−, the e− moves towards the anode, and is then transferred to the cathode where electron flow generates a bioelectric current. Then, H+ moves towards cathode through the proton membrane exchanger and reacts with O_2 (which are produced during microalgal respiration) and forms H_2O. In algal cells, direct photolysis occurs, which produces bioH_2, furthermore, produced algal biomass during this treatment process can be utilized for fermentative bioH_2 production [41]. Table 2 shows the different microalgae strains utilized for bioelectricity generation [42]. Moreover, advance approaches are integrated for advancement of MB-MFC, while its large scale realization need to be demonstrated for real-world application and commercialization [43]. Although, single MB-MFC process is ineffective to generate the power of different commercial implementation; therefore, it can be integrated with AD technology.

Table 2. Different microalgae used for bioelectricity generation.

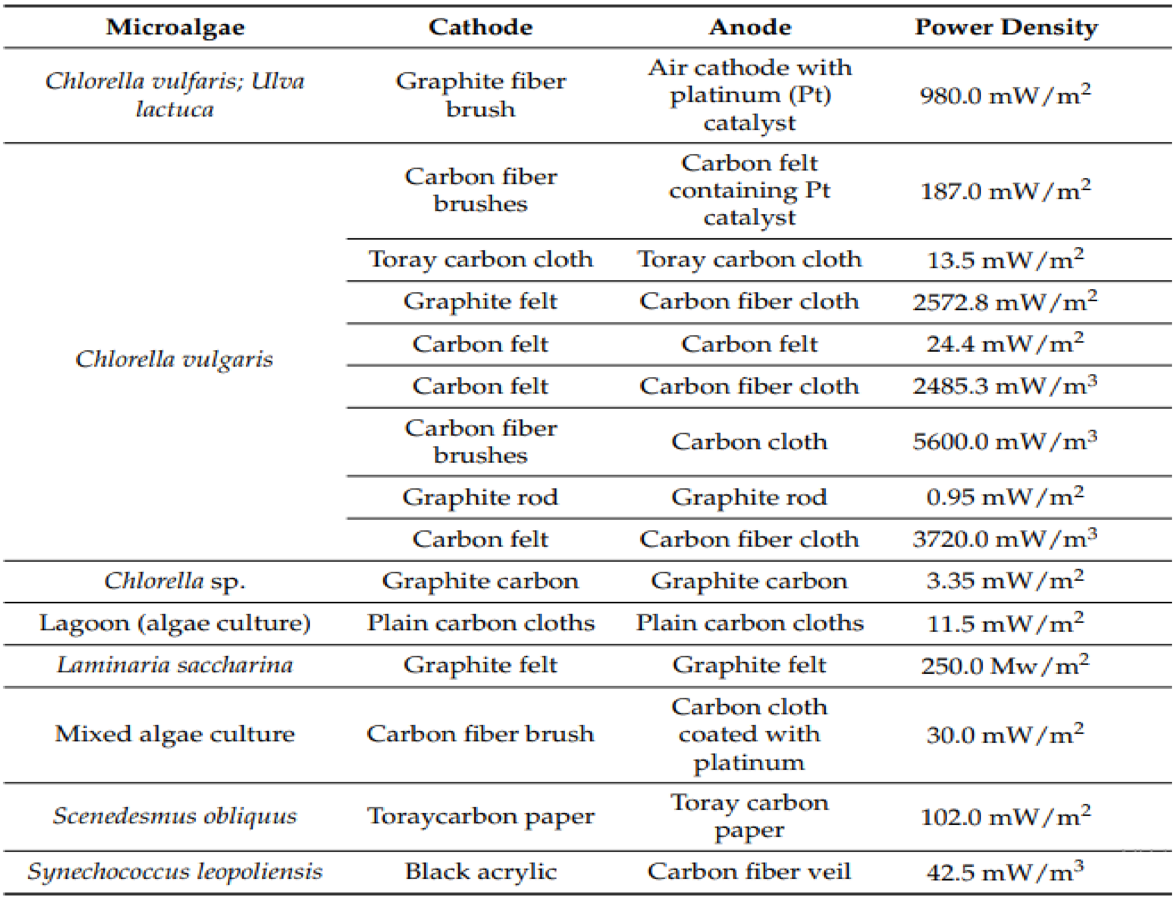

Microalgae	Cathode	Anode	Power Density
Chlorella vulfaris; Ulva lactuca	Graphite fiber brush	Air cathode with platinum (Pt) catalyst	980.0 mW/m^2
Chlorella vulgaris	Carbon fiber brushes	Carbon felt containing Pt catalyst	187.0 mW/m^2
	Toray carbon cloth	Toray carbon cloth	13.5 mW/m^2
	Graphite felt	Carbon fiber cloth	2572.8 mW/m^2
	Carbon felt	Carbon felt	24.4 mW/m^2
	Carbon felt	Carbon fiber cloth	2485.3 mW/m^3
	Carbon fiber brushes	Carbon cloth	5600.0 mW/m^3
	Graphite rod	Graphite rod	0.95 mW/m^2
	Carbon felt	Carbon fiber cloth	3720.0 mW/m^3
Chlorella sp.	Graphite carbon	Graphite carbon	3.35 mW/m^2
Lagoon (algae culture)	Plain carbon cloths	Plain carbon cloths	11.5 mW/m^2
Laminaria saccharina	Graphite felt	Graphite felt	250.0 Mw/m^2
Mixed algae culture	Carbon fiber brush	Carbon cloth coated with platinum	30.0 mW/m^2
Scenedesmus obliquus	Toraycarbon paper	Toray carbon paper	102.0 mW/m^2
Synechococcus leopoliensis	Black acrylic	Carbon fiber veil	42.5 mW/m^3

Polontalo et al. (2021) studied the performance of the MMFC system based on the influence of yeast (8 g L^{-1} and 4 g L^{-1}), "Batik wastewater" concentration (50 % and 100 %), and graphite electrodes (1:1 and 2:2). The MMFC system was carried out by filling anode chamber with "Batik" wastewater and the cathode with C. vulgaris. MMFC simulation was operated for 7 d. Concentration of 100 % "Batik" wastewater and 2:2 number of electrodes gave the best result in MMFC with voltage 0.115 Volt, algae absorbance 0.666. The COD decreased from 824 mg L^{-1} to 752 mg L^{-1} after the MMFC. The addition of 8 g L^{-1} yeast gave the optimum of bioelectricity production reached 0.322

Volt and the microalgae grew until the absorbance reached 1.031.

2.5. Biochar

Biochar is a carbon-rich charcoal made up by thermal decomposition (pyrolysis, hydrothermal liquefaction, and torrefaction) of different organic biomass under low oxygen and high temperature [44].

Pyrolysis is the thermal degradation of biomass in the absence of oxygen, resulting in the production of liquid (bio oil) and solid (biochar) residues, and gaseous products (pygas), effectively transforming wastes into valuable products [45].

Depending on heating velocity and residence time of the process, pyrolysis can be broadly classified as slow (conventional), or fast. Slow pyrolysis maximises solid fraction (biochar) production, and occurs at long residence times and slow heating rates, while liquid and gaseous energy-rich products (bio-oil or pygas) fractions are increased during fast pyrolysis [46]. An increase of pyrolysis temperature generally maximizes the gaseous fraction, minimizing the solid yield [47].

Properties of the solid residue (biochar) also vary in terms of carbon content and composition. Concerning energetic aspects, bio-oil and biochar could be used as fuels, meeting increasing needs for energy from non-fossil fuels sources [48].

However, biochar derived from sewage sludge generally presents high ash content and lower heating value, diminishing its energetic worth [49]. Biochar generally used as biofertilizer or absorbent for wastewater treatment, carbon sequester, etc. However, recent studies suggested that it can be used as a source of coal or coal fuel for the electricity generation [44].

High growth rate, cultivation ease, high lipid and low ash contents makes microalgae highly appealing, compared to other biomasses, with high yields in terms of both bio-oil and biochar [50], as determined with satisfactory results by numerous studies [51, 52, 53].

Microalgal biochar has lower carbon content than biochar from other feedstocks, lower surface area, and lower cation exchange capacity ,while pH, ash and nitrogen contents and extractable inorganic nutrients are high. These properties make it a useful additive to enhance soils characteristics and improve crop productivity, particularly for acidic soils [54]. Table 3 and 4 summarizes the fuel properties of different biochar derived from microalgal biomass and other biomass in dry and wet torrefaction, respectively [42].

Table 3. Fuel properties of different biochar derived from microalgal biomass.

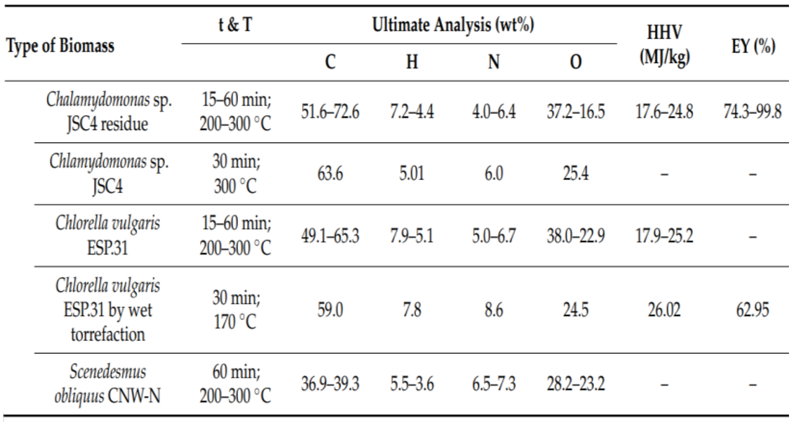

Type of Biomass	t & T	Ultimate Analysis (wt%)				HHV (MJ/kg)	EY (%)
		C	H	N	O		
Chalamydomonas sp. JSC4 residue	15–60 min; 200–300 °C	51.6–72.6	7.2–4.4	4.0–6.4	37.2–16.5	17.6–24.8	74.3–99.8
Chlamydomonas sp. JSC4	30 min; 300 °C	63.6	5.01	6.0	25.4	–	–
Chlorella vulgaris ESP.31	15–60 min; 200–300 °C	49.1–65.3	7.9–5.1	5.0–6.7	38.0–22.9	17.9–25.2	–
Chlorella vulgaris ESP.31 by wet torrefaction	30 min; 170 °C	59.0	7.8	8.6	24.5	26.02	62.95
Scenedesmus obliquus CNW-N	60 min; 200–300 °C	36.9–39.3	5.5–3.6	6.5–7.3	28.2–23.2	–	–

Note: t & T: temperature and time duration; HHV: higher heating value; EY: energy yield.

Table 4. Fuel properties of different biochar derived from other biomass.

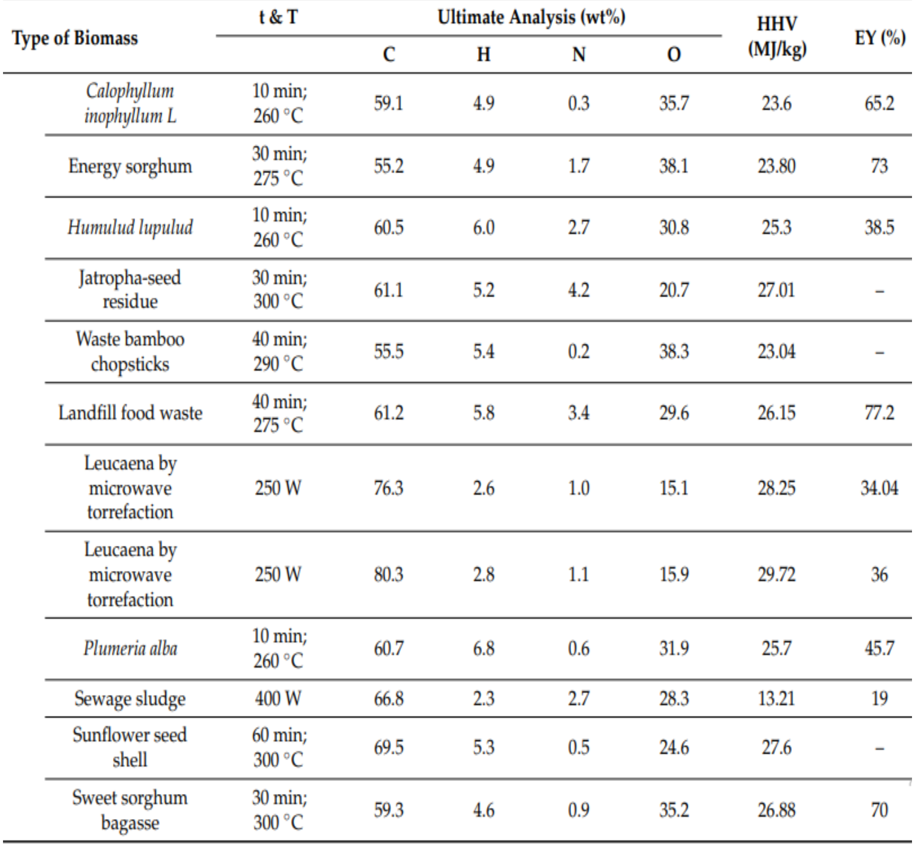

Type of Biomass	t & T	Ultimate Analysis (wt%)				HHV (MJ/kg)	EY (%)
		C	H	N	O		
Calophyllum inophyllum L	10 min; 260 °C	59.1	4.9	0.3	35.7	23.6	65.2
Energy sorghum	30 min; 275 °C	55.2	4.9	1.7	38.1	23.80	73
Humulud lupulud	10 min; 260 °C	60.5	6.0	2.7	30.8	25.3	38.5
Jatropha-seed residue	30 min; 300 °C	61.1	5.2	4.2	20.7	27.01	–
Waste bamboo chopsticks	40 min; 290 °C	55.5	5.4	0.2	38.3	23.04	–
Landfill food waste	40 min; 275 °C	61.2	5.8	3.4	29.6	26.15	77.2
Leucaena by microwave torrefaction	250 W	76.3	2.6	1.0	15.1	28.25	34.04
Leucaena by microwave torrefaction	250 W	80.3	2.8	1.1	15.9	29.72	36
Plumeria alba	10 min; 260 °C	60.7	6.8	0.6	31.9	25.7	45.7
Sewage sludge	400 W	66.8	2.3	2.7	28.3	13.21	19
Sunflower seed shell	60 min; 300 °C	69.5	5.3	0.5	24.6	27.6	–
Sweet sorghum bagasse	30 min; 300 °C	59.3	4.6	0.9	35.2	26.88	70

Note: t & T: temperature and time duration; HHV: higher heating value; EY: energy yield.

3. Challenges of Microalgal Biofuel Production and Future Perspectives

Third generation biofuels and high-value bioproducts produced from microalgal biomass have been considered promising long-term sustainable alternatives for energy and/or food production, potentially decreasing greenhouse gas emissions. Microalgae as a source of biofuels have been widely studied for bioethanol/biodiesel/biogas production [55].

Microalgae present positive impact also on carbon dioxide emissions, in fact they contain about 50% Cover dry weight derived mainly from atmospheric CO_2, therefore, production of 100 tons of microalgae allows fixation of about 183 tons of carbon dioxide [56].

A typical process for obtaining lipids from microalgae involves the following steps: cultivation in open ponds or photo-bioreactors followed by harvesting of algae using technologies like sedimentation, flocculation, filtration, centrifugation, etc. Depending on the process and conditions, primary harvesting concentrations in the range of 2–8 wt% solids are obtained [57]. This is generally followed by secondary harvesting using technologies like filtration or centrifugation. Algae concentrations after secondary harvesting are in the range of 20–27 wt %. Depending on specific technology chosen, feedstocks resulting from primary or secondary harvesting process steps are subject to lipid extraction. Most common methods for the extraction of lipids from microalgae include: solvent extraction, direct transesterification, and algae that secrete products directly into the growth medium (milking). Microalgae as a currently recognized bioenergy producing biomass, its liquid biofuels such as biodiesel and bioethanol have been widely studied [58].

However, there are several knowledge gaps and problems associated with biomass production and lower yield, high expenses, and lack in commercialization of algal bioprocess. To enhance the biomass productivity, high inputs of nitrogen source can be used to enhance the biomass productivity, while modern genetic engineering tools such as CRISPR-Cas9, TALEN, and ZFN-17 can be applied to alter the genome and metabolic pathways of microalgae to enhance the biomass productivity for biofuel production as well as synthesis of various bioactive compounds for various commercial applications. For the reduction of energy consumption during microalgae-based bio-fuel production, further strategies need to be explored. Therefore, several steps need to be integrated to achieve a sustainable low-cost bio-fuel production process [42].

4. Conclusions

Increasing industrialization, demographic expansion and expansion of the transportation and mobility sector worldwide, and especially in developing countries, are the cause of excessive conventional fossil fuels exploitation, leading not only to repeated energy shortages worldwide, but also to increasing global levels of greenhouse gases emissions [59].

Rapid industrial development, depletion of mineral oil reserves, and rise in atmospheric CO_2 require the development of carbon-neutral renewable alternatives. Biofuel production from microalgae is supposed to provide technical and economic feasibility that has the potential for CO_2 sequestration and is therefore, likely to get wide acceptance. Algal biofuels appear to be the only current renewable energy source that could meet the global demand for transport fuels [19].

Algae are one of the most primitive microorganisms on the Earth. They are small photosynthetic organisms that have an ability to completely replace the need of conventional fossil fuel for energy demand. They are robust microorganisms and can be grown in photo-bioreactors, open ponds, sewage or industrial waste without the need of arable land. Microalgal biomass can be converted to variety of biofuels via biochemical and thermochemical methods, they can also be used for the production of high value nutraceuticals at industrial scale [60].

Commercial production of microalgae biofuels remains a major constraint due to the higher cost of microalgae cultivation and biomass harvesting. Therefore, algal biomass should be investigated for potential application in various sectors, mainly marine industries and other sectors. By using microalgae biomass as an alternative raw material energy sources like biohydrogen, methane can be produced through fermentation and photosynthesis. Unlike solar energy, which has the disadvantages of low energy density, instability and difficulty in storage, biohydrogen and biogas are one of the novel ideal energy sources at present. The utilization of microalgae has various attractive prospects in their production due to its cost-effectiveness, renewable biomass and ease of scaling-up technology [61].

5. References

[1] Meghnani, R., (2013). *Microalgal Biofuels: A review*, Recent Research in Science and Technology. 5(5), p. 59-60.

[2] Amaro, H.M., Macedo, A.C. and Malcata, F.X., (2012). *Microalgae: An alternative as sustainable source of biofuels?* Energy, P.1-9.

[3] Pereira, L., (2021). *Algal Biofuels*. 1st Edition. ISBN 9780367782108. Published March 31, 2021 by CRC Press, Talor & Francis group, A science publishers book, p. 212.

[4] Suali, E. and Sarbatly, R., (2012). *Conversion of microalgae to biofuel*. Renewable and Sustainable Energy Reviews. 16(6), 4316–4342.

[5] Mehariya, S., Sharma, N., Iovine, A., Casella, P., Marino, T., Larocca, V., Molino, A., Musmarra, D., (2020). *An Integrated Strategy for Nutraceuticals from Haematoccus pluvialis: From Cultivation to Extraction,* Antioxidants, 9, 825.

[6] Sanchez Rizza, L., Coronel, C.D., Sanz Smachetti, M.E., Do Nascimento, M., Curatti, L., (2019). *A semi-closed loop microalgal biomass production-platform for ethanol from renewable sources of nitrogen and phosphorous*. J. Clean. Prod., 219, p. 217–224.

[7] Goswami, R.K., Mehariya, S., Verma, P., Lavecchia, R., Zuorro, A., (2021). *Microalgae-based biorefineries for sustainable resource recovery from wastewater*, J. Water Process. Eng., 101747.

[8] Solé-Bundó, M., Garfí, M., Ferrer, I., (2020). *Pretreatment and co-digestion of microalgae, sludge and fat oil and grease (FOG) from microalgae-based wastewater treatment plants*. Bioresour. Technol., 298, 122563.

[9] Prabandono, K. and Amin, S., (2015), *Biofuel production from microalgae, Handbook of marine microalgae,* Elsevier, Amsterdam, p. 145–158.

[10] Callegari, A., Bolognesi, S., Cecconet, D., Capodaglio, A.G., (2019). *Production technologies, current role, and future prospects of biofuels feedstocks: a state-of-the-art review*. Crit. Rev. Environ. Sci. Technol., 0, p. 1–53. doi:10.1080/10643389.2019.1629801.

[11] Pan, S.-Y., Snyder, S.W., Packman, A.I., Lin, Y.J., and Chiang, P.-C., (2018). *Cooling water use in thermoelectric power generation and its associated challenges for addressing water-energy nexus,* Water-Energy Nexus, 1, 26–41. doi: 10.1016/j.wen.2018.04.002.

[12] Asongu, S.A., Agboola, M.O., Alola, A.A., and Bekun, F.V., (2020). *The criticality of growth, urbanization, electricity and fossil fuel consumption to environment sustainability in Africa*, Sci. Total Environ., 712, 136376. doi: 10.1016/j.scitotenv. 2019.136376.

[13] IEA International Energy Agency, (2020). Available online at: https://www.iea.org/ (accessed November 28.

[14] Goswami, R.K., Agrawal, K., Mehariya, S., Molino, A., Musmarra, D., Verma, P., (2020a). *Microalgae-Based Biorefinery for Utilization of Carbon Dioxide for Production of Valuable Bioproducts. In Chemo-Biological Systems for CO_2 Utilization*, CRC Press: Boca Raton, FL, USA, p. 203–228.

[15] Goswami, R.K., Mehariya, S., Obulisamy, P.K., Verma, P., (2020b). *Advanced microalgae-based renewable biohydrogen production systems: A review*, Bioresour. Technol., 320, 124301.

[16] Ananthi, V., Raja, R., Carvalho, I.S., Brindhadevi, K., Pugazhendhi, A., Arun, A., (2021). *A realistic scenario on microalgae based biodiesel production: Third generation biofuel*, Fuel, 284, 118965.

[17] Sanz Smachetti, M.E., Coronel, C.D., Salerno, G.L., Curatti, L., (2020). *Sucrose-to-ethanol microalgae-based platform using seawater*. Algal Res., 45, 101733

[18] Garoma, T. and Nguyen, D., (2016). *Anaerobic Co-Digestion of Microalgae Scenedesmus sp. and TWAS for Biomethane Production*, Water Environ. Res., 88, p.13–20.

[19] Singh, N.K. and Dhar, D.W., (2011). *Microalgae as second generation biofuel. A review*. Agronomy Sust. Developm., 31, p. 605–629. DOI 10.1007/s13593-011-0018-0.

[20] Li, X., Hu, H.Y., Gan, K. and Sun, Y.X., (2010). *Effects of different nitrogen and phosphorus concentrations on the growth, nutrient uptake, and lipid accumulation of a freshwater microalga Scenedesmus sp. Bioresour*, Technol., 101, p. 5494–5500.

[21] Halim, R., Danquah, M.K. and Webley, P.A., (2012). *Extraction of oil from microalgae for biodiesel production: A review*. Biotechnology Advances. 30(3), 709-732.

[22] Behera, B., Acharya, A., Gargey, I.A., Aly, N.P.B., (2019). *Bioprocess engineering principles of microalgal cultivation for sustainable biofuel production*. Bioresour. Technol. Rep., 5, p. 297–316.

[23] Sharma, K.K., Schuhmann, H. and Schenk, P.M., (2012). H*igh lipid induction in microalgae for biodiesel production*, Energies 5, 1532–53.

[24] Weldy, C.S. and Huesemann, M., (2013). *Lipid production by Dunaliella salina in batch culture: Effect of nitrogen limitation & light*, US-DOE. Undergrad Research, www.scied.sceince. doe.gov/. accessed 1 November 2013.

[25] Zewdie, D.T. and Ali, A.Y., (2020). Cultivation of microalgae for biofuel production: coupling with sugarcaneprocessing factories. Energy, Sustainability and Society, 10, 27, p. 16. https://doi.org/10.1186/s13705-020-00262-5

[26] Mehariya, S., Patel, A.K., Obulisamy, P.K., Punniyakotti, E., Wong, J.W.C., (2018). *Co-digestion of food waste and sewage sludge for methane production: Current status and perspective*, Bioresour. Technol., 265, p. 519–531.

[27] Angelidaki, I., Treu, L., Tsapekos, P., Luo, G., Campanaro, S., Wenzel, H., Kougias, P.G., (2018). *Biogas upgrading and utilization: Current status and perspectives*, Biotechnol. Adv., 36, p.452–466.

[28] Marín, D., Posadas, E., Cano, P., Pérez, V., Blanco, S., Lebrero, R., Muñoz, R., (2018). *Seasonal variation of biogas upgrading coupled with digestate treatment in an outdoors pilot scale algal-bacterial photobioreactor*. Bioresour. Technol., 263, p.58–66.

[29] Limongi, A.T., Viviano, E., Luca, M.D., Radice, R.P., Bianco, G. and Martelli, G., (2021). *Biohydrogen from Microalgae: Production and Applications*, Applied Science, 11, 1616. P.14. https://doi.org/10.3390/app11041616.

[30] Khosravitabar, F., (2020). *Microalgal biohydrogen photoproduction: scaling up challenges and the ways forward*, Journal of Applied Phycology volume 32, p. 277–289.

[31] Sharma, A. and Arya, S.K., (2017). *Hydrogen from algal biomass: A review of production process*, Biotechnology Reports, Volume 15, September 2017, P. 63-69.

[32] Nagarajan, D., Dong, C., Chen, C., Lee, D., Chang, J.-S., (2020). *Biohydrogen production from microalgae—Major bottlenecks and future research perspectives*, Biotechnol. J., e2000124.

[33] Costa, C.D. and Hadiyanto, H., (2018). *Bioelectricity Production from Microalgae-Microbial Fuel Cell Technology (MMFC)*, MATEC Web of Conferences, 156, 01017. https://doi.org/10.1051/matecconf/201815601017

[34] Polontalo, N.F., Joelyna, F.A., Filardli, A.M.I., Hadiyanto, H. and Zakaria, Z.A., (2021). *Microalgae Microbial Fuel Cell (MMFC) using Chlorella vulgaris and "Batik" Wastewater as Bioelectricity.*

[35] Wang, C.-T., Huang, Y.-S., Sangeetha, T., Chen, Y.-M., Chong, W.-T., Ong, H.-C.; Zhao, F., Yan, W.-M., (2018). *Novel bufferless photosynthetic microbial fuel cell (PMFCs) for enhanced electrochemical performance*, Bioresour. Technol., 255, 8.

[36] Kakarla, R. and Min, B., (2019). *Sustainable electricity generation and ammonium removal by microbial fuel cell with a microalgae assisted cathode at various environmental conditions*, Bioresour. Technol., 284, 161–167.

[37] Xu, C., Poon, K., Choi, M.M., Wang, R., (2015). *Using live algae at the anode of a microbial fuel cell to generate electricity*, Environ. Sci. Pollut. Res., 22, 15621–15635.

[38] Cheng, H.-H., Narindri, B., Chu, H., Whang, L.-M., (2020). *Recent advancement on biological technologies and strategies for resource recovery from swine wastewater*, Bioresour. Technol., 303, 122861.

[39] Leng, L., Zhang, W., Leng, S., Chen, J., Yang, L., Li, H., Jiang, S., Huang, H., (2020). *Bioenergy recovery from wastewater produced by*

hydrothermal processing biomass: Progress, challenges, and opportunities, Sci. Total. Environ., 748, 142383.

[40] Kannah, R.Y., Kavitha, S., Karthikeyan, O.P., Kumar, G., Dai-Viet, N.V., Banu, J.R., (2021). *Techno-economic assessment of various hydrogen production methods—A review*,. Bioresour. Technol., 319, 124175.

[41] Jaiswal, K.K., Kumar, V., Vlaskin, M.S., Sharma, N., Rautela, I., Nanda, M., Arora, N., Singh, A. and Chauhan, P.K., (2020). *Microalgae fuel cell for wastewater treatment: Recent advances and challenges*, J. Water Process. Eng., 38, 101549.

[42] Mehariya, S., Goswami, R.K., Verma, P., Lavecchia, R. and Zuorro, A., (2021). *Integrated Approach for Wastewater Treatment and Biofuel Production in Microalgae Biorefineries*, Energies, 14, 2282. https://doi.org/10.3390/en14082282.

[43] Gurav, R., Bhatia, S.K., Choi, T.-R., Choi, Y.-K., Kim, H.J., Song, H.-S., Lee, S.M., Lee Park, S., Lee, H.S., Koh, J., et al., (2021). *Application of macroalgal biomass derived biochar and bioelectrochemical system with Shewanella for the adsorptive removal and biodegradation of toxic azo dye*, Chemosphere, 264, 128539.

[44] Gan, Y.Y., Ong, H.C., Show, P.L., Ling, T.C., Chen, W.H., Yu, K.L., Abdullah, R., (2018). *Torrefaction of microalgal biochar as potential coal fuel and application as bio-adsorbent*, Energy Convers. Manag., 165, p.152–162.

[45] Chorazy, T., Čáslavský, J., Žvaková, V., Raček, J., Hlavínek, P., (2019). *Characteristics of Pyrolysis Oil as Renewable Source of Chemical Materials and Alternative Fuel from the Sewage Sludge Treatment*, Waste and Biomass Valorization, doi:10.1007/s12649-019-00735-5.

[46] Paz-Ferreiro, J., Nieto, A., Méndez, A., Askeland , M.P.J., Gascó, G., (2018). *Biochar from biosolids pyrolysis: A review*, Int J Environ Res Public Health, 15. doi:10.3390/ijerph15050956.

[47] Inguanzo, M., Dominguez, A., Menéndez, J.A., Blanco, C.G., Pis, J.J., (2002). *On the Pyrolysis of Sewage Sludge: The Influence of Pyrolysis Temperature on Biochar, Liquid and Gas Fractions*, J Anal Appl Pyrolysis, 63, p.209–22. doi:10.4028/www.scientific.net/amr.518-523.3412.

[48] Capodaglio, A.G. and Callegari, A., (2018). *Feedstock and process influence on biodiesel produced from waste sewage sludge*, Journal of Environmental Management, 216, pp. 176-182. doi: 10.1016/j.jenvman.2017.03.089

[49] Callegari, A., Hlavinek, P., Capodaglio, A.G., (2018). *Production of energy (biodiesel) and recovery of materials (biochar) from pyrolysis of urban waste sludge*. Revista Ambiente e Agua, 13(2), p. 21-28. doi:10.4136/ambi-agua.2128.

[50] Yu, K.L., Show, P.L., Ong, H.C., Ling, T.C., Chi-Wei Lan, J., Chen, W.H., et al., (2017). *Microalgae from wastewater treatment to biochar – Feedstock preparation and conversion technologies*, Energy Convers Manag, 150, p.1–13. doi:10.1016/j.enconman.2017.07.060.

[51] Chisti, Y., (2008). *Biodiesel from microalgae beats bioethanol*, Trends Biotechnol, 26, p. 126–31. doi:10.1016/j.tibtech.2007.12.002.

[52] Reen, S., Chyuan, H., Wayne, K., Loke, P., Phang, S., Chuan, T., et al., (2018). *Sustainable approaches for algae utilisation in bioenergy production*, Renew Energy, 129, p.838–852. doi:10.1016/j.renene.2017.04.001.

[53] Chaiwong, K., Kiatsiriroat, T., Vorayos, N., Thararax, C., (2013). *Study of bio-oil and bio-char production from algae by slow pyrolysis*, Biomass and Bioenergy, 56, 600–6. doi:10.1016/j.biombioe.2013.05.035.

[54] Yang, C., Wang C., Li, R., Zhang, B., Qiu, Q., Wang, B., et al., (2019). *Pyrolysis of microalgae : A critical review*, 186, p.53–72. doi:10.1016/j.fuproc.2018.12.012.

[55] Rajagopal, R., Mousavi, S.E., Goyette, B. and Adhikary, S., (2021). *Coupling of Microalgae Cultivation with Anaerobic Digestion of Poultry Wastes: Toward Sustainable Value Added Bioproducts*, Bioengineering, 8, 57. P.13. https://doi.org/10.3390/bioengineering8050057.

[56] Sánchez, A., Garc, M.C.C., Contreras, A., Garc, F., Molina, E., Chisti, Y., (2003). *Shear stress tolerance and biochemical characterization of Phaeodactylum tricornutum in quasi steady-state continuous culture in outdoor photobioreactors*, 16, p. 287–97. doi:10.1016/S1369-703X(03)00072-X

[57] Milledge, j. and Heaven, S., (2013). *A review of the harvesting of micro-algae for biofuel production*. Reviews in Environmental Science and Bio/Technology, 12(2), p.165-178. DOI:10.1007/s11157-012-9301-z

[58] Oumer, A., Hasan, M., Baheta, A.T., Mamat, R., and Abdullah, A., (2018). *Biobased liquid fuels as a source of renewable energy: a review*. Renew. Sust. Energ. Rev., 88, p. 82–98. doi: 10.1016/j.rser.2018.02.022.

[59] Shuba, E.S. and Kifle, D., (2018). *Microalgae to biofuels: 'Promising' alternative and renewable energy, review*. Renew Sustain Energy Rev, 81, p. 743–55. doi:10.1016/j.rser.2017.08.042.

[60] Singh, D. and Gonzales-Calienes, G. (2021). Chapter 11: Liquid Biofuels from Algae. In book: Algae (pp. 243-279). Springer Nature Singapore Pte Ltd., DOI:10.1007/978-981-15-7518-1_11

[61] Wang, K., Shiong Khoo, K., Chew, K.W., Selvarajoo, A., Chen, W., Chang, J. and Show,

P.L., (2021). Microalgae: The Future Supply House of Biohydrogen and Biogas, Frontiers in Energy Research, 9, p. 10. https://doi.org/10.3389/fenrg.2021.660399.

[62] Chisti, Y., (2007). Biodiesel from microalgae, Biotechnol Adv., 25 (3), 294–306. doi:10.1016/j.biotechadv., 2007.02.001.

[63] Illman, A.M., Scragg, A.H., Shales, S.W., (2000). Increase in Chlorella strains calorific values when grown in low nitrogen medium, Enzym Microb Technol., 27,631–635.

[64] Khozin-Goldberg, I., Cohen, Z., Pimenta-Leibowitz, M., Nechev, J., Zilberg, D., (2006). Feeding with arachidonic acid-rich triacylglycerols from the microalga Parietochoris incisa increased recovery of guppies from infection with Tetrahymena sp., Aquaculture, 255,142–150.

[65] Metting F (1996). Biodiversity and application of microalgae, J Ind Microbiol Biotech., 17,477–489.

[66] Solovchenko, A.E., Khozin-Goldberg, I., Cohen, Z., Merzlyak, M.N., (2009). Carotenoid-to-chlorophyll ratio as a proxy for assay of total fatty acids and arachidonic acid content in the green microalga Parietochloris incise, J Appl Phycol., 29,361–366.

INTERNATIONAL JOURNAL OF
COASTAL & OFFSHORE ENGINEERING

IJCOE Vol.6/No.5 /Autumn 2021 (32-38) / **Special issue of "Marine Renewable Energy"**

Available online at: www. Ijcoe.org

Investigation and comparison of the physical models performance of energy extraction from salinity gradient (PRO and RED) in Arvand river estuary

Somayeh Khodadadian Elykai[1], Kamran Lari[2], Masoud Torabi Azad[3*], Abdolreza Sabetahd Jahromi[4], Afshin Mohseni Arasteh[2]

[1] *PhD student in Physical Oceanography, Islamic Azad University- North Tehran Branch, Tehran, Iran.*
[2] *Associate Professor Islamic Azad University- North Tehran Branch, Tehran, Iran.*
[3*] *Professor, Islamic Azad University-North Tehran Branch, Tehran, Iran, M_Azad@Iau-tnb.ac.ir*
[4] *Assistant Professor, Islamic Azad University- Jahrom Branch, Fars, Iran.*

ARTICLE INFO

Article History:
Received: 30 Apr. 2021
Accepted : 27 Nov. 2021

Keywords:
Reverse electro dialysis
Delayed osmosis pressure
Arvand River
Salinity gradient

ABSTRACT

In recent years, scientists have considered the development and utilization of sustainable and environmentally friendly energy resources to replace fossil fuels. One of the newest topics of new energies is the extraction of energy from salinity gradients in seas and oceans. One of the practical methods of energy extraction from salinity gradient is reverse electrodialysis and delayed osmosis pressure. These methods result from mixing two types of water with different salinity concentrations, which are one of the best places to extract energy in the river estuary, where freshwater is naturally mixed with seawater. In this study, using physical parameters measured in 3 hydrometric stations located in Arvand River, achievable Gibbs energy and electrical energy from reverse electro dialysis method and delayed osmosis pressure as physical model setup were investigated. The amount of Gibbs energy obtained using delayed osmosis pressure method from data from three hydrometric stations in Arvand River shows that Khorramshahr station has the highest amount of extractable energy with 0.75 MJ. By calculating the voltage of two heads of each inverse electrodialysis cell in the three studied stations on the Arvand River, it was found that the highest potential difference with the amount of 80 mV was related to Khorramshahr station. Also, the efficiency of the two devices and the selection of the appropriate geographical location for its location were examined.

1. Introduction

With the rapid economic and industrial growth of countries in the world in recent decades and their increasing and comprehensive development, the use of fossil energy resources has increased dramatically. The limitation of fossil fuel resources, diversification of energy resources, sustainable development and energy security and environmental problems resulting from fossil energy consumption on the one hand, and the clean and renewable of new energy resources, on the other hand, have led to the world has paid serious attention to the development and expansion of the use of renewable energies and increasing its share in the world's energy basket. Salinity gradient power (SGP) is one of the renewable and extractable energies from the sea. This potential is mostly in freshwater rivers estuary. Patel first presented the concept of energy production through the mixing of salty and fresh water in 1954, and he mentioned the existence of this energy source [9]. In 2014, a comprehensive and thorough study was conducted at IRENA Institute to investigate the energy gradient energy of salinity and examined how energy extraction and power generation were evaluated when the river flows into the sea by delayed osmosis pressure and electrodialysis methods [11]. He believed that the membrane is the most important factor in both approaches to increase productivity. Sabet Ahd Jahromi et al. (2015) evaluated a physical model based on the reverse electrodialysis method of power density and energy efficiency [14]. In 2016, Emadi et al. investigated the energy potential for energy generation from the intrinsic water of Zarrinehrud River to Urmia Lake and compared energy extraction processes with RED and PRO methods [10]. May et al. (2018) investigated recent developments in energy extraction by reverse electrodialysis method and considered the use of Nano membranes to increase energy and flow effectively [15]. In 2019, Young et al. investigated water treatment before entering different concentration solutions using ultrafiltration and Nano filtration membranes and increased the reverse osmosis pressure device's efficiency [12]. Iran also has several rivers along the Persian Gulf coasts with a suitable position to access this energy source. Therefore, this study aimed to investigate the salinity gradient in the estuary of Arvand River leading to the Persian Gulf and its energy absorption method, which will eventually lead to a laboratory model for energy extraction from the salinity gradient.

2. Materials and methods

2.1. Salinity gradient power (SGP)

Salinity gradient power is one of the renewable and extractable energies from the sea. This potential is mostly in freshwater rivers estuary. As shown in Figure 1, instead of direct discharge of river water into the sea, a cycle of energy generation is used by the salinity gradient's power process on its way, and electrical energy is extracted. The SGP method is based on spontaneous processes and membrane techniques. The automatic process is a kind of reaction carried out without receiving energy from an external source. For this purpose, a thermodynamic function is introduced. This function is called Gibbs' free energy (G) [6].

$$G = H - TS \qquad (1)$$

This energy follows enthalpy (H) and entropy (S). A thermodynamic process is possible when Gibbs' free energy changes are negative.

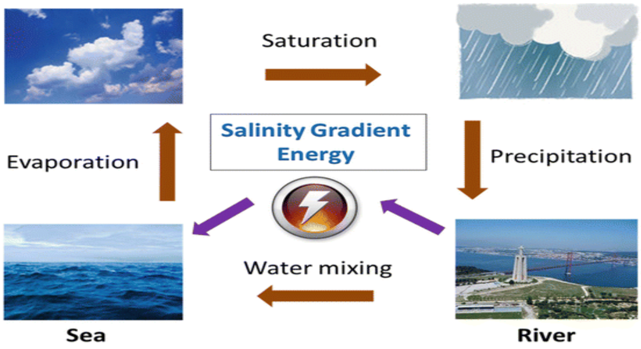

Figure 1: The location of salinity gradient power process in water cyclic for extraction of electrical energy [1]

Delayed osmosis pressure and reverse electrodialysis can be mentioned as energy extraction techniques.

2.2. The theory of delayed osmosis pressure process (PRO)

In the PRO process implementation, finding a stable process with constant pressure and energy production is one of the main energy extraction goals. The high-concentration lethal solution (higher salinity) enters the membrane modulus after passing through a pressure converter, which increases the pressure applied in the flow to reach a constant pressure. Feed flow is pumped at ambient pressure in the opposite direction of the membrane modules. Due to osmotic pressure difference throughout the membrane, which is larger than hydraulic pressure difference, water molecules move from feed solution to lethal solution, which increases concentration flow and dilution of concentration solution and decreases feed flow and concentrates of feed solution. The concentration solution is then pushed towards a current that passes through the turbine, creating a current that passes through the pressure transducer and transmits pressure and re-converts into concentration current [7]. Figure 2 describes a view of this process. Gibbs' energy from mixing two solutions with various concentrations in delayed osmosis pressure will be calculated according to 1 equation [5]. G_{mix} is the energy change of Gibbs energy, where G_S represents the energy from saline water and G_r denotes Gibbs energy from fresh water and G_B is the energy from the mixture of two water at different concentrations.

$$\Delta G_{mix} = G_B - (G_s - G_r) \qquad (2)$$

$$-c_{i,B} V_B \ln(x_{i,B})]$$

$$= RT \sum_i \left[C_{i.S} V_S \ln(x_{i,S}) + C_{i.r} V_r \ln(x_{i,r}) \right)$$

$$\Delta G_{mix} = \sum_i (G_{i,S} + G_{i,r} - G_{i,B})$$

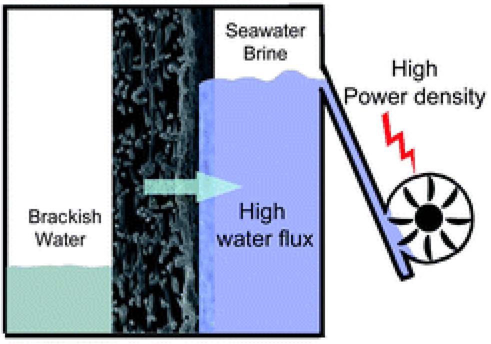

Figure 2: shows the delayed osmosis pressure process [2]

2.3. Inverse electrodialysis process theory (RED)

In this method, concentration difference between successive cells is used. In this case, after the membranes separate the ions, they enter the electrode chamber on both sides of the system, whereby performing oxidation-reduction reactions, an ion current becomes an electron current. This phenomenon causes a potential difference between the electrodes and leads to the charge of a battery. Two types of membranes are used in this battery. One is a cation exchanging membrane (CEM), and the other one is Anion exchanging membrane (AEM). By emitting ions through the membranes, an ion current is produced. This ion current is converted to electron current with suitable reduction reactions in electrodes [4]. Figure 3 describes a view of this process. The theoretical calculation of Gibbs energy derived from the entropy of mixing two solutions with different concentrations is calculated from the following relationship [8].

$$\Delta G = -2RT\left[C_S V_S \ln\frac{C_S}{C_M} + C_R V_R \ln\frac{C_R}{C_M}\right] \qquad (3)$$

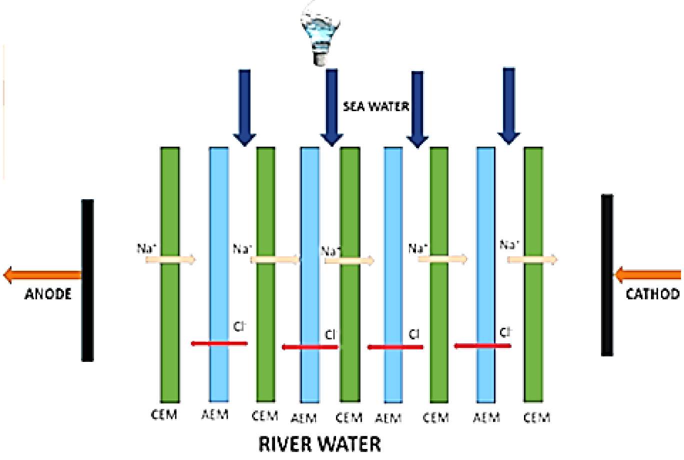

Figure 3: shows the reverse electrodialysis process [3]

One of the most important parameters for calculating the voltage of two heads of each cell is reverse electrodialysis. Using the Nerest equation and determining the ratio of seawater concentration (C_S) to river water (Cr) in different stations, the difference in potential created between the two ends of each cell in the reverse electrodialysis battery is calculated from this equation.

$$E = E^0 - \left(\frac{RT}{zF}\right)\ln\frac{C_S}{C_R} \qquad (4)$$

2.4. The site of study

Arvand River consists of joining the Tigris and Euphrates rivers in the Gharne near Basra city and then by connecting Karun river to it at a distance of 33 km from this city. This river flows into the Persian Gulf after a distance of 110 km. Arvand River basin covers an area of about 948375 km^2[14]. The location of the estuary is in the latitude N 25, 55, 29 ° N and the longitude E 33, 33 ´ 35, 48 °.

To investigate the amount of achievable energy from the average of 8 years data from 3 hydrometric stations of Khosrowabad, Dirifram and Khorramshahr located in Arvand River between 2010 and 2018 is used.

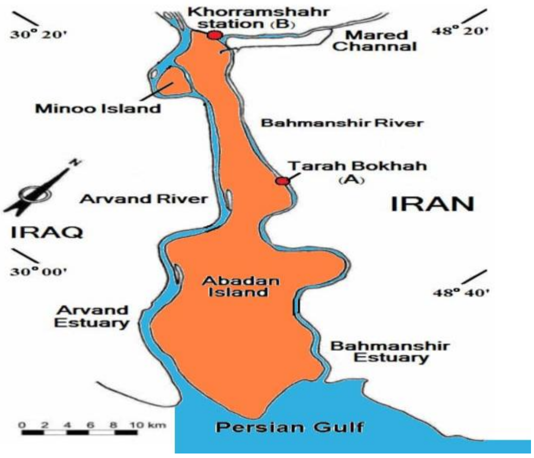

Figure 4: View of Arvand River [13]

3. Results

3.1. Gibbs energy calculation

First, we investigate the physical parameters of river water. These parameters include the total dissolved solids (TDS), electrical conductivity of water (EC) and river water flow. For this purpose, data from the last ten years (from 2010 to 2018) related to the nearest hydrometric station to the Arvandrud estuary were used. To calculate the concentration of river and seawater (C_r), the TDS parameter is divided into the mass of one mole of NaCl.

$$C_r = TDS/58.44\,(mol.m^{-3}) \qquad (5)$$

For the Persian Gulf, the study area showed that seawater salinity in this area is considerable. Its annual average in this area with an appropriate approximation is 40 ppt, which can be considered based on TDS equal to 40000 mg/lit. Therefore, seawater Concentration (CS) is:

$$C_S = \frac{TDS}{58.44} = \frac{40000}{58.44} \approx 684.46\,mol/m^3 \qquad (6)$$

To obtain Gibbs free energy, first, the concentrations of river and sea water were obtained in 3 hydrometric stations of Khosrowabad-Direfram and Khorramshahr in Arvandrud according to Table 1.

Table 1: Water Concentrations of Arvand River and the Persian Gulf from 2010-2018 in 3 Hydrometric Stations

Monitoring station	Latitude	Longitude	Year	$C_S = \frac{TDS}{58.44}(mol/m^3)$	$C_r = TDS/58.44$ $(mol.m^{-3})$	$C_M = \frac{C_S V_S + C_R V_R}{V_S + V_R}$
Khosroabad	30-09-53	48-24-48	2010-2018	684.46	187.0308	500.4
Dirifam	30-22-58	48-11-09	2010-2018	684.46	85.5462	307.14
Khoramshahr	30-26-36	48-08-26	2010-2018	684.46	64.1907	293.68

Gibbs energy in equations 2 and 3 is calculated with the river and sea concentration values. Since the amount of input and output volume is very important First, Gibbs free energy (ΔG) for combining different volumes of seawater (VS) and river (Vr) is investigated. In the combination of different sea and river water ratios, increasing the amount of river water compared to seawater has a more effective role in increasing the amount of Gibbs free energy extraction. Therefore, by obtaining the best volume of input and output of Gibbs energy in 3 hydrometric stations, it was calculated according to table 2. Since its value was negative, it shows that this is a spontaneous process.

Table 2: Gibbs energy in 3 hydrometric stations using two methods

Monitoring station	(PRO) ΔG (MJ)	(RED) ΔG (MJ)
Khosroabad	-0.33	-1.11
Dirifam	-0.66	-1.32
Khoramshahr	-0.75	-1.88
T=298K V_s=1.46m^3 Vr=0.74m^3 C_s~684.46mol/m-3		

3.2. The physical model of PRO

To design and construct a physical model based on delayed osmosis pressure method, a plate with a diameter of 11 cm was initially considered. Then, 34 holes with an approximate area of 1 cm per hole were created. The membrane retaining plate was also cut on a 3 mm thick Plexi-glass plate using a laser cutting machine. In PRO, the active membrane layer encounters a high concentration solution (seawater) and porous support with feed solution (river water). PRO membranes are characterized by their intrinsic membrane properties such as water permeability, solute permeability, and the support layer's structural parameter. The membrane used in the physical model of TFC membrane is a nanostructure that can improve system performance by increasing the process speed and reducing sedimentation. In figure (5) the schematic design of the physical model made is shown.

To test the physical model of pure water without ion and then the solution of different concentrations was made. These solutions consisted of three different concentrations, including 50 ppm, 25 ppm, and 35 ppm, considered saltwater of the sea. Also, water with a concentration of 10 ppm was prepared under the title of river water (freshwater).

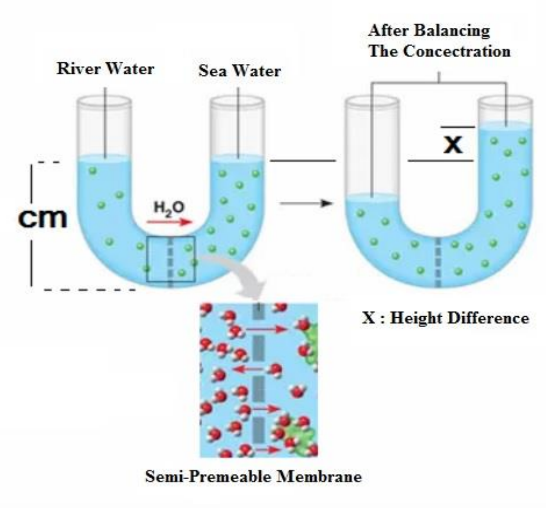

Figure 5: Schematic design of physical model PRO

Then, 3 different seawater concentrations with river water were placed alternately to test the physical model. The volume of each solution is 4000 cc. Both waters with different concentrations were placed on either side of the semi-permeable membrane with an involved surface area of 34 cm^2. In vitro and in different periods, the difference in height created in saline water solution column for different concentrations was obtained according to the table (3). The results showed that the highest height created in the mixing conditions is 50 ppm in seawater and 10 ppm in river water.

Table 3: the difference created by mixing

	25 ppm	35 ppm	50 ppm
Time(min)	H(cm)	H(cm)	H(cm)
0	0	0	0
30	1	1.2	1.5
60	1.6	2.3	4.1

90	2.4	4.1	6.2
120	3.9	5.4	7.7
150	4.6	6.3	8.2
180	4.9	6.7	8.7
210	5.2	6.9	9
240	5.6	7.3	9.2

The difference in height between the two columns of water in the U-shaped tube compared to the time for different salinity gradients shows that the height difference at the concentration of 50ppm has increased with increasing time.

Using the created height difference and increasing the water source volume with a high concentration of turbine has moved and produced flow. The higher the height difference, the higher the reservoir's energy potential and the output current from the mini-generator increases. Table 4 shows the flow rate obtained from the water micro-generator.

Table 4: the flow rate obtained from the height difference created by the salinity gradient

Current taken from a water micro-generatorI(mA)	Reservoir potential energyU(J)	Tank emptying timer(s)	Outlet flow from the tank drain valve Q(cm2/s)	Draining valve cross sectionA(cm2)	Water discharge rate from Drain valveV(cm/s)	The volume of water in the tank V(cm3)	Water tank cross section A(cm2)	Maximum height of the water columnH(cm)	Salinity gradient ppm
25.35	0.65	6.85	105.41	0.785	134.28	722.20	78.5	9.2	50
17.67	0.41	6.10	93.90	0.785	119.62	573.05	78.5	7.3	35
11.69	0.24	5.25	82.24	0.785	104.77	431.75	78.5	5.6	25

3.3. RED physical model

To evaluate the performance of designed reverse electrodialysis battery, the reverse electrodialysis battery chambers are filled with a volume of seawater Vs and river water Vr with different salt concentrations. In this system, an ion process is produced converted to electron current by reduction-oxidation reactions in electrodes. This process continues until the concentration of the solutions becomes identical on both sides. The membrane used in the physical model of nanostructure membrane. The aim of selecting nano-membranes is to help increase the process speed and reduce sedimentation.

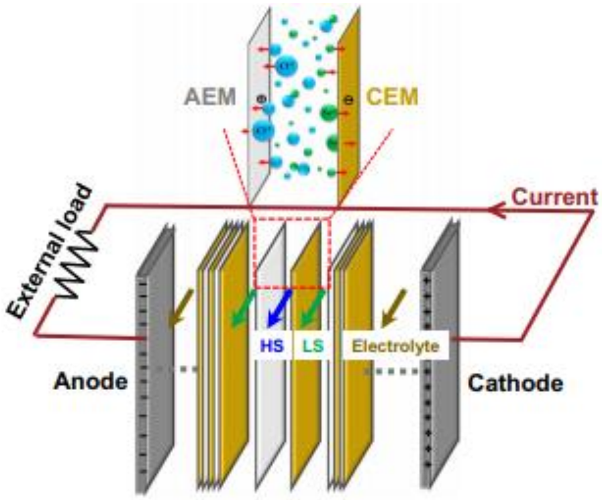

Figure (6): shows the performance of the reverse electrodialysis battery [15]

In this study, first, 4 liters of each of the diluted and thick salt solutions and electrolyte solutions were prepared. The concentration of these solutions is specified in the table (5). By injecting electrolyte solutions into the electrode chamber, dilution and thick solutions were injected into the membranes at two flux rates. In both cases, first, the system entrances are opened for a few seconds so that the salty and sweet water cells are fully filled. In this case, the system exits are completely closed. The time it takes for the system to be filled with ten ml/s flux rate is 32 seconds, and for the flux rate of 20 ml/s, it is 24 seconds.

Table 5: the concentration of used solutions

Number	Solution	Concentration
1	Dilute solution (river water)	0.017M (gNaCl / lit.)
2	Concentrated solution (sea water)	0.4 M (gNaCl / lit.30)
3	Electrolyte solution (CuSO4)	0.01 M

In table (5), the amount of potential difference between the two heads of each cell in the reverse electrodialysis system is calculated theoretically and according to the ratio of seawater to river water concentration for each hydrometric station.

Table 6: Potential difference between the two heads of each cell in the battery

River	Station	$V(mV)$
Arvand	Khosrowabad (A)	48
	Dirifram (B)	55
	Khorramshahr (C)	80

4. Conclusion and discussion

Arvand River is the largest and most important river in the Persian Gulf, so the study of gradient power is of special importance.

The amount of Gibbs energy obtained using delayed osmosis pressure method from data of three hydrometric stations in Arvand River shows that Khorramshahr station with 0.75 MJ has the highest amount of extractable energy. Since this negative value is obtained, it can be said that salinity gradient energy is a spontaneous process from which energy can be extracted. Since the investigation of energy extraction methods from salinity gradient is a new method for generating electrical energy; therefore, the results were obtained by establishing the physical model of PRO. Initially, with increasing the volume of water with high concentration, the highest height difference created in the physical model PRO with a height difference of 9.2 cm was related to the concentration of sea salinity of 50 ppm and river concentration of 10 ppm. The highest generated flow was 9.2 cm in height and ten ppm salinity concentration, which produced 26.35 mA.

Arvand River is the largest and most important river in the Persian Gulf, so the study of gradient power is of special importance. The amount of Gibbs energy obtained using delayed osmosis pressure method from data of three hydrometric stations in Arvand River shows that Khorramshahr station with 0.75 MJ has the highest amount of extractable energy. Since this negative value is obtained, it can be said that salinity gradient energy is a spontaneous process from which energy can be extracted. Since the investigation of energy extraction methods from salinity gradient is a new method for generating electrical energy; therefore, the results were obtained by establishing the physical model of PRO. Initially, with increasing the volume of water with high concentration, the highest height difference created in the physical model PRO with a height difference of 9.2 cm was related to the concentration of sea salinity of 50 ppm and river concentration of 10 ppm. The highest generated flow was 9.2 cm in height and ten ppm salinity concentration, which produced 26.35 mA.

In the reverse electrodialysis method, Gibbs energy obtained from three hydrometric stations in Arvand River shows that this river has the highest amount of extractable energy in Khorramshahr station with 88.1 MJ. For the theoretical voltage of two heads of each cell, reverse electrodialysis in a RED system in three stations on the Arvand River shows that the greatest potential difference with 80 mV is related to Khorramshahr station.

By examining and comparing these two methods, it can be said that both processes can be done spontaneously, and Khorramshahr station has the best efficiency. The advantage of RED over PRO is that the electrical energy generated occurs at a lower salinity gradient, while in the PRO process, a higher salinity gradient difference is required. Therefore, placement of PRO device next to Khorramshahr desalination plant is an important step towards energy extraction. Another advantage of RED compared to PRO is that turbines are needed for electrical production in the delayed osmosis pressure method. Still, in the reverse electrodialysis method, an ion current is produced by emitting ions among the membranes.

4.1. Suggestions

The results show that the membrane system covers 50-80% of the cost of making the device according to the salinity difference level. Therefore, further development in membrane technology and identification of suitable membranes will significantly impact the possibility of processing and pathway to the market. As membrane permeability is determinative, the interaction between fluid and membrane is important in the system's permeability, so it is suggested that carbon nanotubes be used in the model in subsequent research. The physical model test in areas with output potential such as Lake Urmia; and using a delayed osmosis simultaneously with other devices related to salinity gradients, can be effective as well.

References

[1] Sylwin PawlowskiJoão CrespoSvetlozar Velizarov, 2015, "*Sustainable Power Generation from Salinity Gradient Energy by Reverse Electrodialysis*" https://link.springer.com/book/10.1007/978-3-319-20179-5, pp 57-80

[2] Xiaoxiao Song, Zhaoyang Liu and Darren Delai Sun,2013," *Energy recovery from concentrated seawater brine by thin-film nanofiber composite pressure retarded osmosis membranes with high power density* "Energy &Environmental Science, 2013,6, 1199-1210

[3] Mukesh Sharma1, Arun Chakraborty, Jayanarayanan Kuttippurath and Atul Kumar Yadav, 2018," *Potential Power Production from Salinity Gradient at the Hooghly Estuary System*" Innovative Energy & Research,.

[4] Veerman, J., "Reverse Electro-dialysis: Performance of a Stack with 50 Cells on the Mixing of Sea and River Water", Vol. 327, Journal of Membrane Science, 2009, pp. 136-144.

[5] Han, Sui Zhang, Xue Li, Tai-Shung Chung, *Progress in pressure retarded osmosis (PRO) membranesfor osmotic power generation*,(2015), Progress in Polymer Science July

[6] Zemansky, M. W., Dittman, R., 1981. "*Heat and Thermodynamics*", sixth edition, Mc Graw-Hill, pp. 233-267.

[7] Anthony P. Straub, Akshay Deshmukh and Menachem Elimelech, 2016," *Pressure-retarded*

osmosis for power generation from salinity gradients: is it viable?” Energy & Environmental Science, Cite this: Energy Environ. Sci., 2016, 9, 31, DOI: 10.1039/c5ee02985f

[8] Sabetahd Jahromi AR , 2014. “*Study of salinity gradients in the Persian Gulf and an experimental model for electric energy extraction from them using nano-membranes* (Doctoral dissertation, Islamic Azad University, Science and Research Branch, Tehran).

[9] Pattle, R.E., 1954. "*Production of electric power by mixing fresh and salt water in the hydroelectric pile*", Nature , Vol. 174, pp.660.

[10] Arash Emdadi, PetrosGikas, Maria Farazaki, YunusEmami, 2016, “*Salinity gradient energy potential at the hyper saline Urmia Lake e ZarrinehRud River system in Iran*”, Renewable Energy 86,154e162

[11] IRENA Ocean Energy Technology Brief 2, *salinitygradient energy technology brief*, June 2014

[12] TianshiYangChun, FengWanJun, YingXiongTai-ShungChung, 2019,” *Pre-treatment of wastewater retentate to mitigate fouling on the pressure retarded osmosis (PRO) process*”.

[13] http://www.gpsnauticalcharts.com/

[14] Sabetand Jahromi, A. (2014). *Study of salinity gradients in the Persian Gulf and an experimental model for electric energy extraction from them using nano-membranes* (Doctoral dissertation, Islamic Azad University, Science and Research Branch, Tehran).

[15] Ying Mei, Chuyang Y. Tang, 2018,” *Recent developments and future perspectives of reverse electrodialysis technology: A review*”, Desalination, 425. 156-174.

INTERNATIONAL JOURNAL OF
COASTAL & OFFSHORE ENGINEERING

IJCOE Vol.6/No.5 /Autumn 2021 (39-50)/ **Special issue of “Marine Renewable Energy”**

Available online at: www. Ijcoe.org

The Application of Energy Absorbers to Harness Wave Energy in the Caspian Sea: A Feasibility Study

Mohammad Hossein Jahangir [1*], Mehran Mazinani [2], Zahra Ranji[3]

[1*] *Associated Professor, Faculty of New Sciences and Technologies, University of Tehran, Iran; mh.jahangir@ut.ac.ir*
[2] *MSc. Student, Faculty of New Sciences and Technologies, University of Tehran, , Iran; mzn.mehran@gmail.com*
[3] *MSc. Student, Faculty of New Sciences and Technologies, University of Tehran, , Iran; zahra.ranji@ut.ac.ir*

ARTICLE INFO

Article History:
Received: 06 Feb. 2021
Accepted: 1 Sep. 2021

Keywords:
Wave Energy Converter
Energy Absorbers
Caspian Sea
Feasibility Study

ABSTRACT

Since renewable energy can be a good solution to respond to oil crises, the disadvantages of using them and increasing energy demand in a sustainable way in the future, and because the oceans cover two-thirds of the earth's surface, harnessing the energy of the oceans can be a source of green energy for coastal areas. At present, the generation of electricity from ocean waves by wave energy converters is considered as a potential future energy source in many countries. Currently, the electricity generation from ocean waves by wave energy converters is considered as a potential future energy source in many countries. Therefore this study aims to investigate the potential of wave energy in the Caspian Sea from the Iranian perspective, and in the next step, propose a framework to select an absorber to harvest this energy. Although there are studies to assess the potential of wave energy in this region,but none of them considered more than one type of absorber in the models. To this aim, the wind data samples of the European Center for Medium-Range Weather Forecasts are used to model the Caspian sea by implementing Mike 21 software from which the power and height of waves data are obtained within the years 2001 to 2015. Based on the results of this phase and the geographical conditions, a weighting framework is applied to select an absorber for harvesting wave energy. The results indicate that the best technology to harness energy in the Caspian Sea is the WEPTOS absorber. This technology benefits from low complexity while offering high efficiency.

1. Introduction

The oil crisis in the 1970s prompted the world to explore alternatives for fossil fuels [1]. Furthermore, it is expected that the world's energy demand will increase by 30 percent from 2010 to 2040 [2,3]. Renewable energies could be a solution to meet demand in a sustainable way in the future [4] and since the oceans cover two-thirds of the Earth's surface, harnessing ocean energy could be a green energy supply for coastal regions [5]. Currently, the electricity generation from ocean waves by wave energy converters (WECs) is considered as a potential future energy source in many countries [6,7]. Fluctuated power generation due to inherently fluctuations of renewables such as wind and solar electricity supplies could cause instability in energy systems. This instability comes from a mismatch between the electricity production pattern and electric load profile. Wave energy converters (WECs) can produce electricity from the waves with a lower rate of power fluctuation and higher capacity factor compared to wind and solar supplies, which have the capacity factors around 30% and 20%, respectively [8–11]. Moreover, the wave resources compared to other variable renewable resources generate energy with advantages including, predictability, availability, and less land acquisition [12–17]. Although numerous research regarding renewable energies utilization has been conducted in Iran, the wave energy harvesting has been studied the least. In this study, we intend to evaluate the Caspian sea shoreline wave energy potentials and to propose the most befitting wave energy converter (WEC) technology to harness this energy. Table 1 provides the details of these projects. [18].

Table 1. Specification of renewable energy projects of Iran

Renewable energy	Project name	Capacity of project (Mw)
Wind	111 installed turbines in Manjil 43 installed turbines in Binalud 4 installed turbines in Tabriz	61.18 28.38 0.67
Solar	Darbid Yazd and SarKavir Semnan Power plant development Solar water heater in Yazd, Khorasan, Sistan and Baluchestan and Isfahan Shiraz solar plant (Vapor phase)	0.012 – 0.017 4.312 0.25
Geothermal	Meshkinshahr geothermal power plant(Conduct exploration drilling, production and injection) in Ardabil Construction 3–5 MW package in Ardabil	50 3 - 5
Biomass and Biogass	Manufacture of semi-industrial stack Vanadium redox battery in Alborz(Energy reservation) Feasibility study for installing of biomass power plant in Fars and Khorasan(Survey potential-land fill) Construction biomass power plant in Shiraz and Mashhad(Land fill) Feasibility study for manufacturing of Biogas in Saveh	0.001 1.06 – 0.65 1.2 – 0.66 0.6
Fuel cell and Hydrogen	Purchase, installation and operation of 25 kW fuel cell polymer and Accessories in Alborz Semi-industrial scale pilot projects in hydrogen technology in Alborz	0.025 0.2

Although the first wave energy converter (WEC) was created in 1799 in France by Gerard and his son, Masuda can be recognized as the father of the modern wave energy. He launched a navigation buoy equipped with an air turbine, which is now called the OWC converter. In recent years, the WEC technologies have improved and developed significantly [19–23]. Moreover, studies [24] tested the commercial size of WECs in the oceans to harvest energy from waves. The value of the wave energy hinges on the wavelength and wave height [25]. As a result, studies [26] in this field mostly focused on the aforementioned features to assess the energy characteristics of wave energy resources. Studies [25] investigated the potential of wave energy resources in the Caspian Sea, the Persian Gulf, and the Gulf of Oman and found a large number of hotspots with high energy potential Iran. Previous studies [27], with the same regions of study, proposed three districts in Iran (Qeshm, Chabahar, and Anzali) as the best candidate for deployment of wave energy stations using 3-h wind data from 2010. Other studies [28] found two districts in Iran, including Noshahr and Babolsar, as attractive locations to install wave energy converters. Studying 11-year wind data of the Caspian Sea using the (Simulation Wave Numerical) SWAN software [29] depicted that the central zone of this region has the highest wave energy potential while the northern zone has the lowest potential. In other studies [30], the same software, SWAN software, is used to model wave energy resources in the Gulf of Oman in the south of Iran, indicating 2.8 kW/m annual energy for this region. Studies found a range of 0.2 and 1.2 kW/m annual energy for the wave energy resources in the Caspian Sea (Anzali port coast), showing that the wave power is more considerable in winter and spring than summer and autumn.

The WECs are divided into four main categories: Wave Bodies Active (WAB) [31], Oscillating Water Column(OWC) [32], Point Absorbers [33] and Overtopping [34] that can be placed from the shore to the sea.

Although there are studies [35,36] to assess the potential of wave energy around the world, there is a gap in the scope of studies to fully investigate the different types of absorbers. In Iran, so far, no energy converters have been installed for capturing the energy of the Caspian Sea. Therefore, the aim of this study, initially, is to model the waves characteristics of this sea, and subsequently choose an energy converter system by evaluating the characteristics of the sea waves and examining the dynamic and geographical features of the Caspian Sea.

2. Model Description

Numerous software can be used to simulate and determine the wave energy. in the present study, MIKE software was selected and implemented. Initially, we model the waves of Caspian sea using the third generation of Mike 21 SW software. This version is one of the latest MIKE 21 software modules, replaced the OSW (Off Shore Wave) module. The SW model is a third-generation wavelength spectral model which is used to simulate the production, growth, decay and transformation of wind-generated waves and swell offshore and coastal areas [37]. The basic conservation equations are formulated in either Cartesian coordinate for a small-scale application. To generalize the governing equation in geographical and spectral space, the cell centered finite volume method is applied. An unstructured mesh technique is used in the geographical domain. The time integration is performed using a fractional step approach where a multi-sequence explicit is applied to the propagation of wave action.

The dynamics of the gravitational waves are described by the transport equation for wave action density. The wave action density spectrum is a function of two wave phase parameters (varies in time and space). The two wave phase parameters can be the wave direction, θ, and either the relative (intrinsic) angular frequency, or the absolute angular frequency. Alternatively, the wave phase parameters can be also the wave number vector, $\vec{k}$ with magnitude, k and direction, θ. The relative angular frequency, σ ,and the wave direction, θ., have been chosen to formulate the dynamics of the gravitational waves in the current model.

The action density relates to the energy density by:

$$N = \frac{E}{\sigma} \tag{1}$$

where in Eq.(1) N (σ, θ) and E (σ, θ) stand for action density and energy density, respectively.

For wave propagation over gradually varying depths and currents, the relation between the relative angular frequency and the absolute angular frequency, are described by the linear dispersion relation:

$$\sigma = \sqrt{gk\tanh(kd)} = \omega - \vec{k}.\vec{U} \tag{2}$$

Where in Eq.(2) g is the acceleration of gravity, d is the water depth, ω is absolute angular frequency, and $\vec{U}$ is the current velocity factor. The magnitude of the group velocity of the wave energy relative to the current, c_g, is described by:

$$c_g = \frac{\partial_\sigma}{\partial_k} = \frac{1}{2}\left(1 + \frac{2kd}{sinh(2kd)}\right)\frac{\sigma}{k} \tag{3}$$

Where in Eq.(3) c describes the phase velocity of the wave relative to the current follows:

$$c = \frac{\sigma}{k} \tag{4}$$

A range between a minimum frequency, σ_{min} limits the frequency spectrum which is split up into a deterministic prognostic part for frequencies lower than a cut-off frequency and analytical diagnostic part for frequencies higher than the cut-off frequency. Based on WAMDI Group (1988) and Komen et al. (1994), a dynamic cut-off frequency depending on the local wind speed and mean frequency is used as in the WAM Cycle 4 model.

The governing equation, based on Komen et al. (1994) and Young (1999), is defined as the wave action balance equation which has been formulated in either Cartesian of spherical coordinate.

2.1. Cartesian coordinates

The conservation equation for wave action, in horizontal Cartesian coordinate, can be describes as:

$$\frac{\partial N}{\partial t} + \nabla.(\vec{v}N) = \frac{S}{\sigma} \tag{5}$$

Where in Eq.(5) N($\vec{x}.\sigma.\theta.t$) depicts the action density and t shows the time, $\vec{x} = (x.y)$ is the Cartesian co-ordinates, S is the source term for the energy balance equation, and $\vec{v} = (c_x, c_y, c_\sigma, c_\theta)$ refers to the propagation velocity of a wave in the four-dimensional phase space $\vec{x}$, σ and θ. ∇ is the four-dimensional differential operator in the $\vec{x}$, σ, θ-space. The four characteristic propagation speeds are described by:

$$(c_x.c_y) = \frac{\overrightarrow{dx}}{dt} = \vec{c_g} + \vec{U} \tag{6}$$

$$c_\sigma = \frac{d\sigma}{dt} = \frac{\partial\sigma}{\partial d}\left[\frac{\partial d}{\partial t} + \vec{U}.\nabla_{\vec{x}}d\right] - c_g\vec{k}.\frac{\partial\vec{U}}{\partial s} \tag{7}$$

$$c_\theta = \frac{d\theta}{dt} = -\frac{1}{k}\left[\frac{\partial\sigma}{\partial d}\frac{\partial d}{\partial m} + \vec{k}.\frac{\partial\vec{U}}{\partial m}\right] \tag{8}$$

Where in Eq.(7) s represents the space coordinate in wave direction θ, and in Eq.(8) m is a coordinate perpendicular to s. $\nabla_{\vec{x}}$ Is the two-dimensional differential operator in the $\vec{x}$-space.

2.2. Spherical coordinates

The conserved property is spherical coordinates, is the action density $\hat{N}(\vec{x},\sigma,\theta,t)$. Here, $\vec{x}$= (ϕ,λ) is the spherical co-ordinates, where ϕ is the latitude and λ is the longitude. The action density $\hat{N}$ is related the normal action density N (and normal energy density E) while $\hat{N}d\sigma d\theta d\phi d\lambda = Nd\sigma d\theta dxdy$, or:

$$\hat{N} = NR^2\cos\phi = \frac{ER^2\cos\phi}{\sigma} \tag{9}$$

Where in Eq.(9) R shows the radius of the earth. The wave action balance equation in spherical polar coordinates is following:

$$\frac{\partial\hat{N}}{\partial t} + \frac{\partial}{\partial\phi}c_\phi\hat{N} + \frac{\partial}{\partial\lambda}c_\lambda\hat{N} + \frac{\partial}{\partial\sigma}c_\sigma\hat{N} + \frac{\partial}{\partial\theta}c_\theta\hat{N} = \frac{\hat{S}}{\sigma} \tag{10}$$

Here in Eq.(10) $\hat{S}$($\vec{x}$,σ,θ,t)=S$R^2\cos\phi$ is the total source and sink function. S is the energy source term which depicts the superposition of source function describing various physical phenomena:

$$S = S_{in} + S_{nl} + S_{ds} + S_{bot} + S_{surf} \tag{11}$$

Here in Eq.(11) S_{in} represents the generation of energy by wind, S_{nl} is the wave energy transfer due to non-linear wave-wave interaction, S_{ds} is the dissipation of wave energy because of white-capping, S_{bot} is the dissipation because of bottom friction and S_{surf} is the dissipation of wave energy because of depth-induced breaking.

The spectral moment of order ith for the calculation of spectral wave parameters is computed by the equation in mike 21 SW model:

$$m_i = \int_0^{2\pi}\int_0^{\infty} E(f.\theta) f^i df d\theta \qquad (12)$$

Where in Eq.(12) E(f,θ) is the direct spectrum of wave energy and f is the wave frequency. Thus, the height characteristics of the wave Hs, the wave period Te and the mean period of time Tm are obtained from the following equations:

$$H_s = 4\sqrt{m_0}$$

$$T_e = \frac{m_{-1}}{m_0} \qquad (13)$$

$$T_m = \frac{m_0}{m_1}$$

The flux of energy per unit length, so-called wave power, P, is defined by equation (14):

$$P = \rho g \int_0^{2\pi}\int_0^{\infty} c_g(f.\theta) E(f.\theta) df\, d\theta \qquad (14)$$

Where in Eq.(14) ρ is the density of the seawater as follows. In deep water(d$> 0.5L$) follows equation (15):

$$P = \frac{\rho g^2}{64\pi} H_s^2 T_e \approx (0.49) H_s^2 T_e \;\; kW/m \qquad (15)$$

2.3. Model setup

Data from monitoring wind for 6 hours at a distance of 10 meters from the ECMWF (European Center for Medium-Range Weather Forecasts) was used with a resolution of 0.75×0.75 square kilometers in order to model the sea waves. To validate this model, results are compared with the measured data of buoys on the Anzali coast with geographical coordinates of 49.52 degrees north and 37.55 degrees eastern within May 2003 to June 2003 as well as city of Neka with geographical coordinates of 51.51 degrees north and 37.87 degrees east from October 2006 to May 2007.

2.4. Model Validation

The model validation is done using the aforementioned parameters and periods. For a more accurate evaluation of the accuracy of the validation results, for each of the courses, the scatter results are plotted and the statistical parameters that represent the accuracy of the matching two series of data are presented. These parameters include: Model skill (Ia), Scattering Index (SI), Correlation Coefficient (CC), BIAS and Root Mean Square Errors (RMSE).

Each of the above parameters are described in the following statistical relationships where x is the statistical series for results of the measurements, y is the statistical series of the results of the mode, $\bar{x}$ and $\bar{y}$ are mean of each of these two series and n is the total number of data in the statistical series. The results of the final validation are described in detail in Table 2.

$$I_a = 1 - \frac{\sum (x_i - y_i)^2}{\sum \left(|x_i - \bar{x}| + |y_i - \bar{y}|\right)^2} \qquad (16)$$

$$SI = \frac{\sqrt{\frac{1}{n}\Sigma((y_i - \bar{y}) - (x_i - \bar{x}))^2}}{\bar{x}}$$

$$CC = \frac{\Sigma(x_i - \bar{x})(y_i - \bar{y})}{\sqrt{\Sigma(x_i - \bar{x})^2 \Sigma(y_i - \bar{y})^2}}$$

$$Bias = (\bar{y} - \bar{x})$$

$$RMSE = \sqrt{\frac{1}{n}\Sigma(y_i - x_i)^2}$$

Table 2. Summary of error values obtained at the Caspian Sea Validation Station

	$\boldsymbol{H_s\ (m)}$				
	$\boldsymbol{I_a}$	$\boldsymbol{SI}$	$\boldsymbol{CC}$	$\boldsymbol{BIAS(m)}$	$\boldsymbol{RMSE(m)}$
Anzali	0.89	0.89	0.82	0.11	0.33
Neka	0.93	0.45	0.89	0.15	0.37
	$\boldsymbol{T_p\ (s)}$				
Anzali	0.79	0.34	0.76	0.86	1.38
Neka	0.89	0.21	0.79	0.01	1.11

As can be seen in Figures 1a and 1b for port of Anzali and Figures 2a and 2b for port of Neka as well as Table 2, the modeling results show a good fit based on the measurement values in the mentioned time periods. Thus, the modeling of the Caspian Sea for 15 years from 2001 to 2015 is performed using the proposed model.

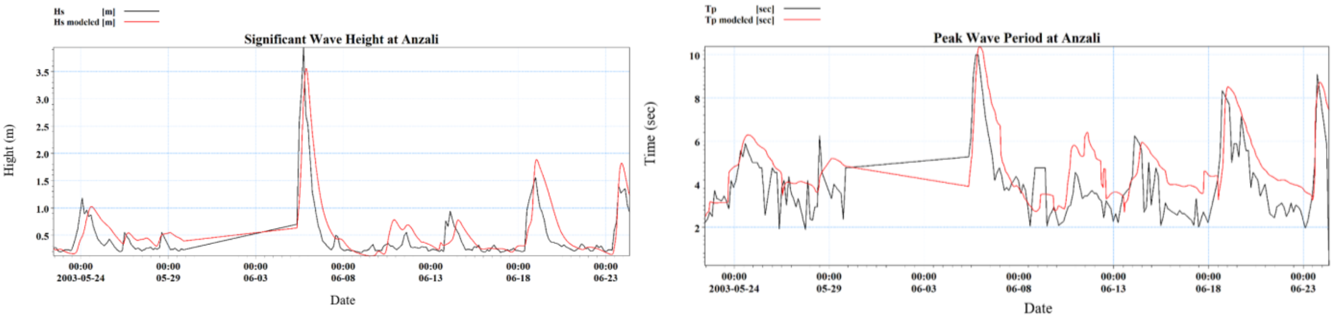

Figure 1. wave characteristics of port of Anzali in 2003

Figure 2. wave characteristics of port of Neka in 2003

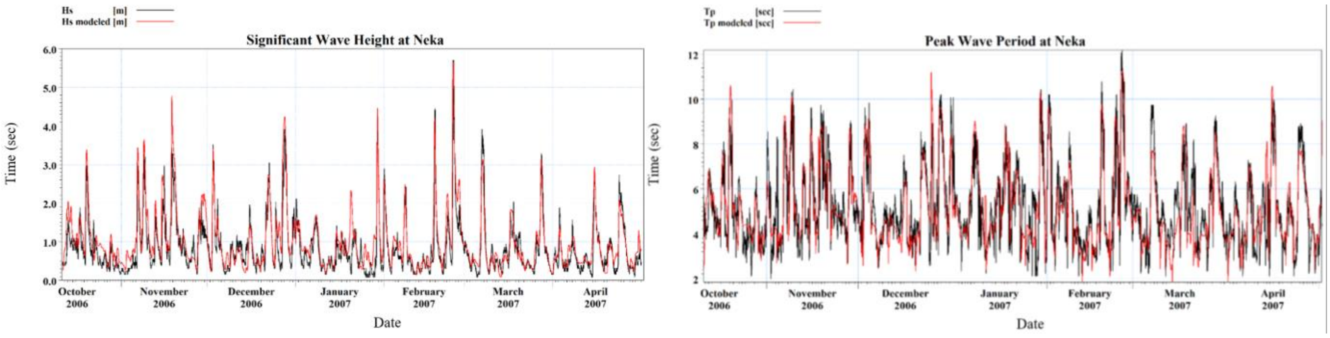

3. The simulation of the Caspian Sea waves

3.1. Caspian Sea Wave

In this section, we provide details about modeling Caspian Sea for 15 years (from 2001 to 2015). Figure 3 shows the location of the Caspian Sea which is located between the 47.13 and 36.34 latitudes and 46.43 and 54.51 longitudes. The Caspian Sea ,with 7000 km shoreline, is the largest lake around the world surrounded by Iran in the south, Kazakhstan and Turkmenistan in the east and Russia in the north and North West and Azerbaijan in the west.

Figure 3. Location of Caspian Sea

The associated counter related to the wave heights in 2015 is shown in Figure 4 and Figure 5. As it can be seen, due to the low wind speeds in the spring, the average wave height is about 1 meter in the first season of the year for April to May months. Though, with the arrival of the summer season, due to the high temperature variation within day and night, the wind Speed has increased and the average wave height increased slightly and reached about 2 meters, around twice that of the spring. In the autumn, the wave height values in the Caspian Sea peak, and this amount decreases slightly in winter, but with thesecontours, it can be seen that the highest wave height values occur in the autumn and winter seasons.

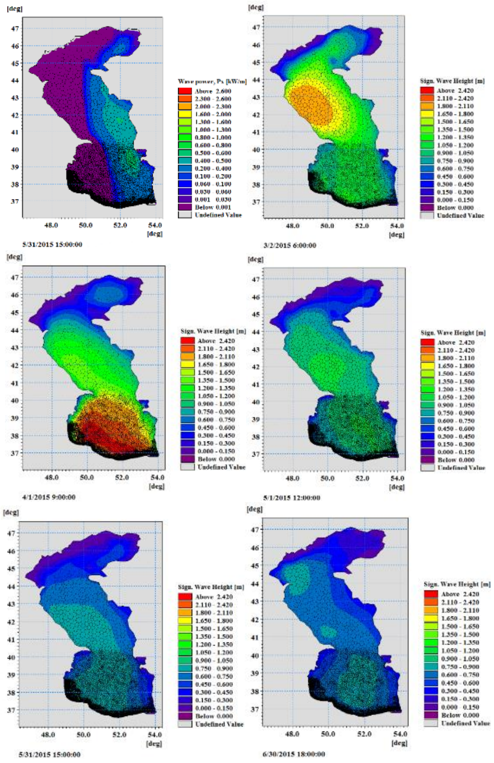

Figure 4. Counter of the Caspian Sea wave peaks in the first half of the year

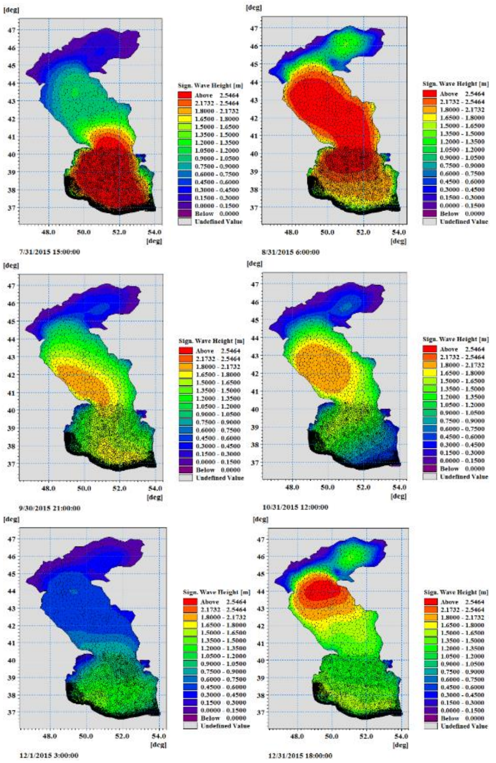

Figure 5. Counter of the Caspian Sea wave peaks in the second half of the year

Figure 6 depicts the locations which has been chosen for further investigation on the southern coast of the Caspian Sea. The main criteria for choosing these points is their importance based on harbor activities. Therefore, in commercial or fishery ports, the results of modeling and statistical analysis are presented with higher accuracy than the other points. These 23 stations are represents of the region of the case study which are described in Table 3.

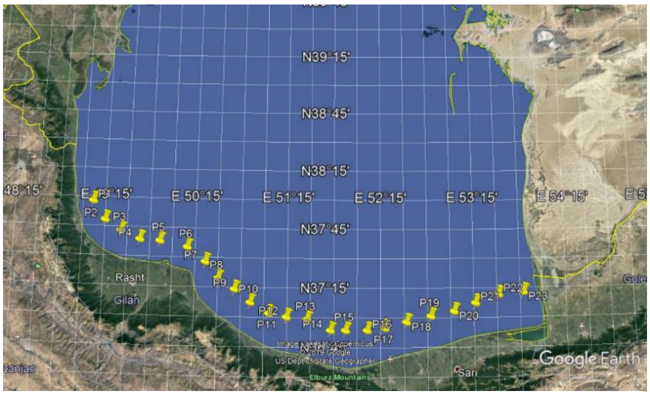

Figure 6. Location of the Chosen Stations

Table 3. The characteristics of the selected wave stations

Selected point	Coordinates (Lon/Lat)(°)	Water depth(m)	Closest urban centers
P1			
P2			
P3	49.09 N, 37.90 E	-15.5	Talesh
P4	49.23 N, 37.74 E	-26	Paresar
P5	49.41 N, 37.65 E	-56	Sangachin
P6	49.62 N, 37.58 E	-235	Hassanroud
P7	49.84 N, 37.57 E	-287	Hagi Bekandeh
P8	50.14 N, 37.52 E	-272	Mohsen Abad
P9	50.34 N, 37.40 E	-250	Amirabad
P10	50.48 N, 37.26 E	-366	Rudsar
P11	50.66 N, 37.17 E	-380	Oshiyan
P12	50.83 N, 37.06 E	-349	Ramsar
P13	51.03 N, 36.97 E	-471	Tonekabon
P12	51.22 N, 36.94 E	-551	Nashtarud
P13	51.44 N, 36.92 E	-584	Namakabrud
P12	51.69 N, 36.83 E	-499	Nowshahr
P13	51.85 N, 36.83 E	-488	Tooskatok
P14	52.08 N, 36.83 E	-467	Nur
P15	52.27 N, 36.85 E	-379	Mahmudabad
P16	52.50 N, 36.90 E	-392	Sorkhroud
P17	52.76 N, 36.95 E	-213	Babolsar
P18	53.01 N, 36.99 E	-176	Khazarabad
P19	53.24 N, 37.06 E	-95	Zeynaroud
P20	53.49 N, 37.13 E	-21	Emamadeh
P21	53.76 N, 37.15 E	-10	Bandar Torkaman
P22			
P23			

The result of the modeling is presented as wave characteristics and wave roses graphs. The simulation was performed for the selected stations and the mean results for fifteen years were presented in Figure 7. As it can be seen in this Figure, the selected stations P6 to P19 have the highest amount of wave power in the central-southern side of the Caspian sea which makes them suitable locations to harness wave energy. This potential wave energy in the west-southern and east-southern sides is lower compared to the central side (the eastern side has the lowest wave power potential). In the spring, due to low-speed wind blowing in the Caspian Sea, the wave power reaches its minimum (see Figure 7 (a)). This power increases in the summer by raising the wind speed and then reaches its highest value in the autumn. The wave power in the winter and autumn is almost twice the power in the summer and spring for the region of the case study (see Figure 7).

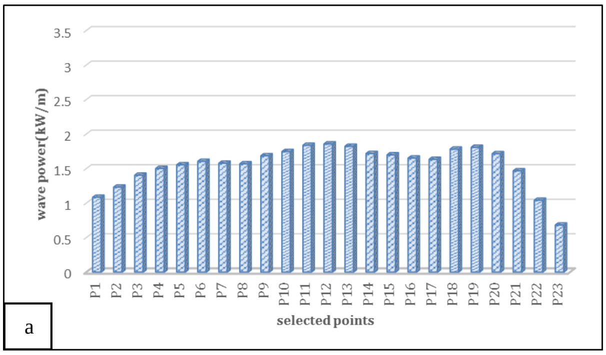

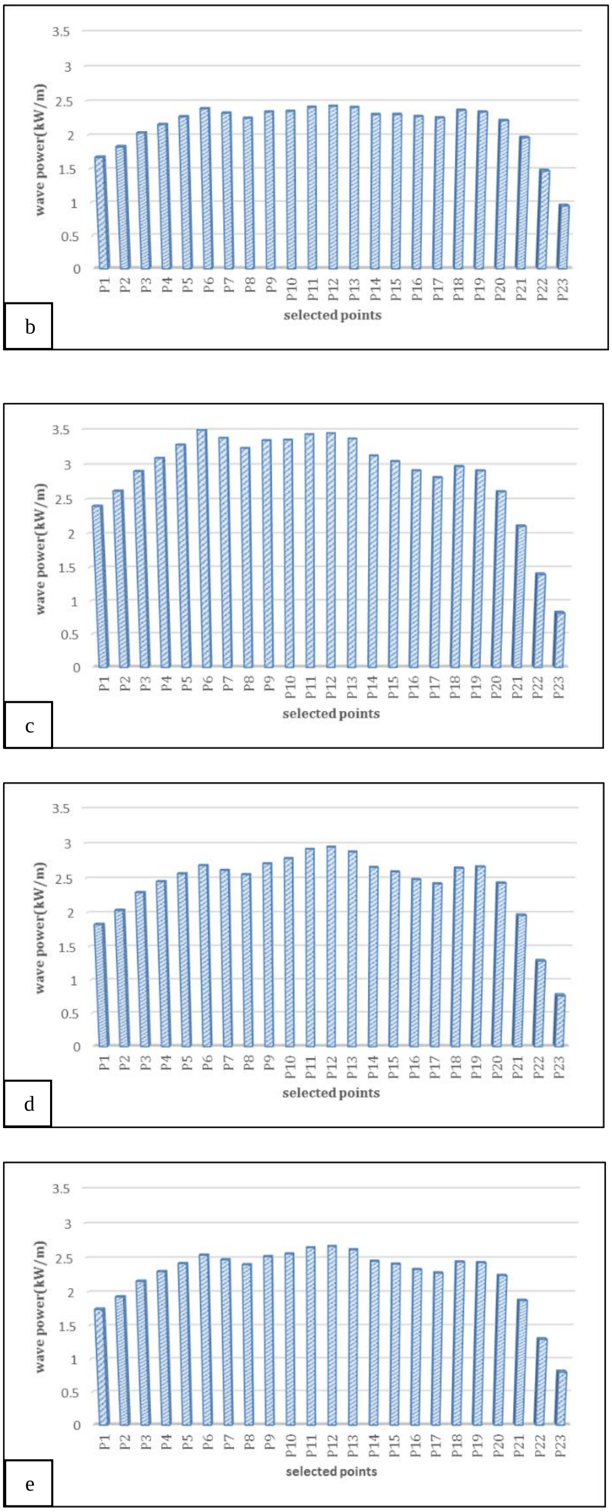

Figure 7. The measured mean wave power within the 15 years period for the selected stations in: (a) spring, (b) summer, (c) autumn, (d) winter and (e) annual

Figure 8 represents the wave rose, wind rose and power rose charts of the selected stations during the period of 15 years. Each unit in the x and y axis correlate to 10% of the total surface. The efficiency of the WECs highly hinges on the wave direction which should be consider in the installation procedure. The simulation results show that the direction of the waves, on the southern coast of the Caspian Sea, is towards north-east for the west side, towards the north in the middle side, and towards north-east for the east side.

4. Wave Energy Converters

4.1. Technologies

To select the best converter for the Caspian Sea wave energy recovery, a variety of wave energy converters are evaluated in the next section. There are currently about 80 technologies for wave energy conversion. Wave energy converter systems can be categorized into four main categories, including wave-activated bodies, point absorbers, oscillating wave columns and overtopping systems. These categorizations are based on installation and deployment on shoreline, offshore, or on the sea bed and a brief description of each provided in this subsection [38–41].

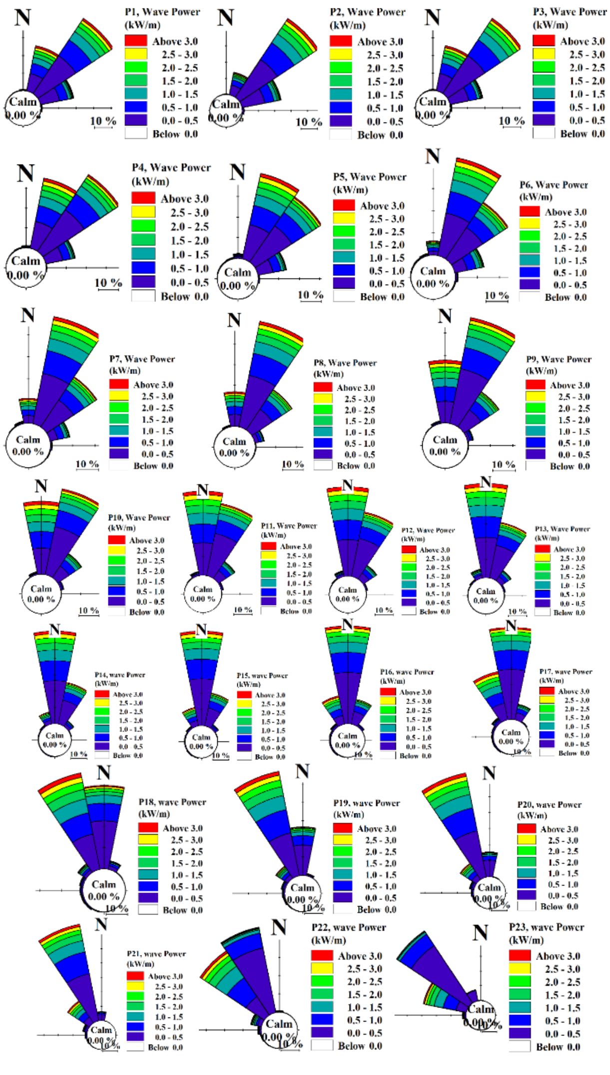

Figure 8. wave rose diagrams from the fifteen-years modeling

Active devices operate by moving relative oscillation bodies from the wave motion. These devices include an unbreakable reference that the absorbing body can fluctuate towards, and the energy is constrained by the power transmission system via dipping or resisting movement of these objects. The converters are Pelamis [42], DEXA [43], WEPTOS [44], Anaconda [45], SEAREV [46], Salter Duck [47], McCabe [48], WaveRoller [49], Oyster [50], and BioWave [51], the characteristics of which are given in Table 4.

Table 4. Characteristics of WAB devices

Device	Type	Water Depth (m)	Average Wave Power (KW/m)	Output Power (kW)
Pelamis	Floating on sea surface	50	40-70	750-2250
DEXA	Floating on sea surface	50	10	160
WEPTOS	Fixed on sea surface	16.3	39	925
Anaconda	Floating on sea surface	75	50	1000
SEAREV	Fixed on sea surface	50	40	500
Salter Duck	Floating on sea surface	2-30	24	375
McCabe	Floating on sea surface	30-40	53	257
WaveRoller	Fixed on sea coast	10-15	40	300
Oyster	Fixed on seabed	20	19	200
BioWave	Fixed on seabed	25-40	35-50	250

4.1.2 Point Absorbers

Point absorbers are devices that move their relative oscillation bodies via wave motion. These devices include an unbreakable reference that the absorbing body can fluctuate towards, and the energy is constrained by the power transmission system by dipping or resisting movement of these objects. OPT Power [52], AquaBuoy [53], WaveBob [54] and Archimedes Wave Swing [55] are of a variety of converters, and their characteristics are described in Table 5.

Table 5. Characteristics of Point Absorber devices

Device	Type	Water Depth (m)	Average Wave Power (KW/m)	Output Power (kW)
OPT Power	Floating on sea surface	30-60	50	40-500
AquaBuoy	Fixed on sea surface	45-76	20-50	250
WaveBob	Fixed on sea surface	21-24	70-80	131
Archimedes Wave Swing	Fixed on seabed	43	30-40	221

4.1.3. Oscillating Water Column (OWC)

Oscillating Water Column is an offshore deep water converter which compresses the air above the surface of the water and the swells cause the water column to force the air through an air turbine, resulting in the movement of the turbine. This method is considered to be the most efficient method, since its efficiency is about 80% with a relatively simple mechanism and is resistant to storms. The characteristics of these converters can be found in Table 6 which include OSPREY [56], Limpet [57], Mutriku [58] and Mighty Whale [59].

Table 6. Characteristics of OWC devices

Device	Type	Water Depth (m)	Average Wave Power (KW/m)	Output Power (kW)
OSPREY	Floating on sea surface	14.5	50	500
Limpet	Fixed on coast	6	20	113
Mutriku	Fixed on coast	5	26	68.5
Mighty Whale	Fixed on sea surface	40	15	110

4.1.4. Overtopping Devices

These systems are partly dipped in water, which uses wave energy to transfer seawater into a sloping canal and fill a reservoir. Using the height difference, low height turbines move and generate energy. The characteristics of Wave Dragon [60], Tapchan [61] and Sea Slot-Cone Generator (SSG) [62] are described in Table 7.

Table 7. Characteristics of Overtopping devices

Device	Type	Water Depth (m)	Average Wave Power (KW/m)	Output Power (kW)
Wave Dragon	Fixed on sea surface	20-40	60	625-940
TAPCHAN	Fixed on coast	20	20-30	350
SSG	Fixed on coast	6-18	14-16	49-62

4.2. WEC Selection Framework

The factors affecting the selection of a wave energy converter in the Caspian Sea are divided into two main parts; the first part is related to the physical conditions associated with the Caspian Sea, and the second part is related to the structural properties of the wave power converter. Having considered all these criterions, the most suitable energy converter for Caspian sea is selected.

- **Wave energy potential:** As shown in Figures 7 and 8, the waves of the Caspian Sea have a characteristic wave height of 0 to 2 meters and a potential power average of 1 to 4 kilowatt-per-meter near the coast.
- **The converters power output:** The amount of power generated by a device that is normalized according to mass, volume, and capital cost. This factor is the most important decision making parameter. Each wave power converter

system is rated on a scale of 1 and 10 points based on its power generation potential.

- **Sea-bed conditions:** Wave energy converters that are hooked to the seabed cannot be deployed in the Caspian Sea due to its relatively unstable seabed. Hence we assign a score of 1 for systems that are fixed onto the seabed, a Score 4 for systems that are fixed on the shore, a score of 7 for systems floating on the surface of the water, and a score of 10 for converters that do operations without need of seabed.
- **The development of wave power converter devices:** Wave energy converters vary in terms of technology advancements and development. Figure 9 depicts the share of each technology in worldwide wave power generation [24]. Therefore, score 10 for point absorber buoy converters, 6 for WABs, 3 OWCs, and 2 scores for overtopping converters are assigned, respectively.

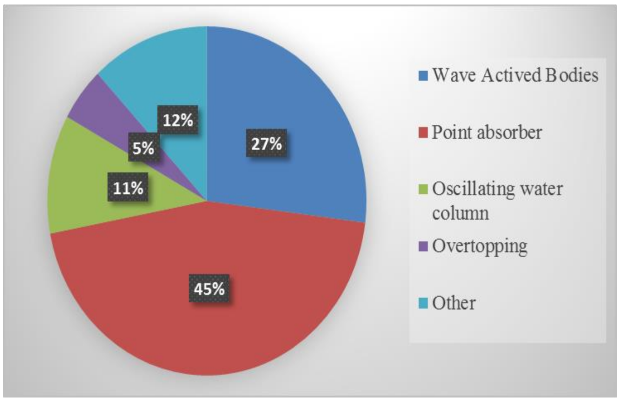

Figure 9. The share of each WEC in the worldwide wave power generation [24]

Based on the above factors, the specific scores for each technology of the available wave energy converters are given in Table 8 based on which the total score of each device is calculated and shown in Figure 10. As it can be seen, the best technology to harness energy in the Caspian Sea is the WEPTOS device which benefits from low complexity while offering high efficiency.

Table 8. Related parameter scores for wave energy absorbers to be used in Caspian sea

Device	Device Progress	Sea Condition	Power
Pelamis	6	7	10
DEXA	6	7	6
WEPTOS	6	10	9
Anaconda	6	7	7
SEAREV	6	10	5
Salter Duck	6	7	6
McCabe	6	7	2
WaveRoller	6	4	3
Oyster	6	1	4
BioWave	6	1	2
OPT Power	10	7	2
AquaBuoy	10	10	3
WaveBob	10	10	1
Archimedes Wave Swing	10	1	2
OSPREY	3	7	4
Limpet	3	4	2
Mutriku	3	4	1
Mighty Whale	3	10	3
Wave Dragon	2	7	7
TAPCHAN	2	4	5
SSG	2	4	2

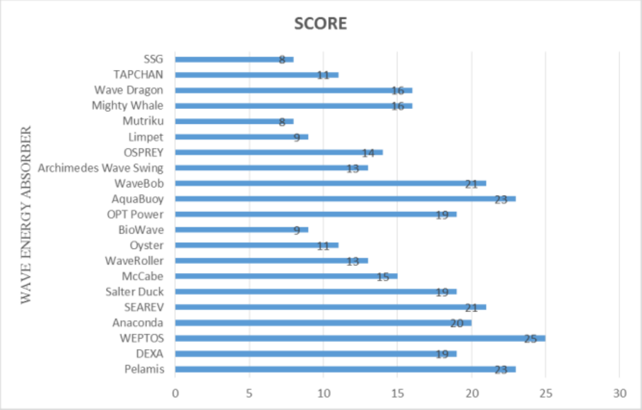

Figure 10. Evaluation of the wave energy absorbers

The structural shape of the WEPTOS device is similar to the letter A. This converter is comprised of two symmetrical arms, each of which consists of 20 separate rotors [63]. The rotors on each arm are connected to a separate generator. The transfer of torque from arm to the generator is carried out through a gear mechanism. The angle of the arms varies depending on the weather conditions. In less extreme near shore climates, the arm length increases in order to harvest the maximum wave energy from a wide range of ocean waves. This enhances the energy produced and covers a wider range of waves, which significantly increases the average annual energy received from the waves. Furthermore, in extreme storm condition, the angle between the arms decreases to prevent structure damage due to the force applied through the waves. In such a situation, minimizing cross-sectional area of the device exposed to the waves, the maximum force from the maximum force applied to the device in the normal state does not exceed. This device has the following distinctive features that distinguish it from other converters [64]:

- High efficiency
- Low capital cost
- Scalability of the device (depending on the conditions, adding or lowering the rotor modules can reduce or increase the capacity of the converter)
- Suitable for low height of waves (for example, for waves with Hs between 0 and 3 meters and Tp between 3 and 7 seconds [44])

5. Conclusions

This study aimed to investigate the potential of wave energy in the Caspian Sea from the Iranian perspective, as a baseline for a framework to select an absorber to harvest this energy. To this aim, the wave power potential was evaluated using the 15-year period annual, seasonal, and monthly wind data from ECMWF for 23 selected stations on the southern side of the Caspian Sea. Furthermore, these results, from the simulation performed by MIKE, were validated based on real data for two stations, including the Anzali and The Neka stations. The error measurement factors such as RMSE and BIAS factors showed great goodness of fit to simulate the wave energy in the region of the case study.

In the next step, a framework is proposed to select an absorber for harvesting the wave energy on the southern coast of the Caspian Sea based on the results of this phase and the geographical conditions. The results indicate that the best technology to harness energy in the Caspian Sea is the WEPTOS absorber. This technology benefits from low complexity while offering high efficiency.

6. References

[1] S. Foteinis, J. Hancock, N. Mazarakis, T. Tsoutsos, and C. E. Synolakis, “A comparative analysis of wave power in the nearshore by WAM estimates and in-situ (AWAC) measurements. The case study of Varkiza, Athens, Greece,” *Energy*, vol. 138, pp. 500–508, Nov. 2017.

[2] “Outlook for Energy: A perspective to 2040 | ExxonMobil.” [Online]. Available: https://corporate.exxonmobil.com/Energy-and-environment/Looking-forward/Outlook-for-Energy/Outlook-for-Energy-A-perspective-to-2040#Buildingaperspective. [Accessed: 15-Sep-2020].

[3] S. M. Mortazavi, A. Maleki, and H. Yousefi, “Analysis of robustness of the Chinese economy and energy supply/demand fluctuations,” *Int. J. Low-Carbon Technol.*, vol. 14, no. 2, pp. 147–159, 2019.

[4] E. Ahmadi, B. McLellan, S. Ogata, B. Mohammadi-Ivatloo, and T. Tezuka, “An integrated planning framework for sustainable water and energy supply,” Sustain., vol. 12, no. 10, 2020.

[5] J. C. S. Barstow, G. Mørk, D. Mollison, “*The Wave Energy Resource,*” Ocean wave energy, Springer, pp. 93–132, 2008.

[6] O. Langhamer, K. Haikonen, and J. Sundberg, “Wave power-Sustainable energy or environmentally costly? A review with special emphasis on linear wave energy converters,” *Renew. Sustain. Energy Rev.*, vol. 14, no. 4, pp. 1329–1335, 2010.

[7] A. F. de O. Falcão, “Wave energy utilization: A review of the technologies,” *Renew. Sustain. Energy Rev.*, vol. 14, no. 3, pp. 899–918, Apr. 2010.

[8] B. Drew, A. R. Plummer, and M. N. Sahinkaya, “A review of wave energy converter technology,” vol. 223, pp. 887–902, 2009.

[9] R. Pelc and R. M. Fujita, “Renewable energy from the ocean,” *Mar. Policy*, vol. 26, no. 6, pp. 471–479, 2002.

[10] M. Mohammadi, R. Ghasempour, F. Razi Astaraei, E. Ahmadi, A. Aligholian, and A. Toopshekan, “Optimal planning of renewable energy resource for a residential house considering economic and reliability criteria,” *Int. J. Electr. Power Energy Syst.*, vol. 96, no. September 2017, pp. 261–273, 2018.

[11] N. Ghorbani, A. Kasaeian, A. Toopshekan, L. Bahrami, and A. Maghami, “Optimizing a hybrid wind-PV-battery system using GA-PSO and MOPSO for reducing cost and increasing reliability,” *Energy*, vol. 154, pp. 581–591, 2018.

[12] M. Leijon, H. Bernhoff, M. Berg, and O. Ågren, “Economical considerations of renewable electric energy production—especially development of wave energy,” *Renew. Energy*, vol. 28, no. 8, pp. 1201–1209, 2003.

[13] A. Rashid and S. Hasanzadeh, “Status and potentials of offshore wave energy resources in Chahbahar area (NW Omman Sea),” *Renew. Sustain. Energy Rev.*, vol. 15, no. 9, pp. 4876–4883, 2011.

[14] S. M. Mortazavi and S. Garoosi, “Role of Energy Supply and demand Fluctuations in Macroeconomic Development of Iran,” vol. 1, no. 1, pp. 85–92, 2019.

[15] S. C. Pryor and R. J. Barthelmie, “Climate change impacts on wind energy: A review,” *Renew.*

Sustain. Energy Rev., vol. 14, no. 1, pp. 430–437, 2010.

[16] M. Mehrpooya, M. Mohammadi, and E. Ahmadi, "Techno-economic-environmental study of hybrid power supply system: A case study in Iran," *Sustain. Energy Technol. Assessments*, vol. 25, no. September 2016, pp. 1–10, 2018.

[17] G. Iglesias, M. López, R. Carballo, A. Castro, J. A. Fraguela, and P. Frigaard, "Wave energy potential in Galicia (NW Spain)," *Renew. Energy*, vol. 34, no. 11, pp. 2323–2333, 2009.

[18] M. Bahrami and P. Abbaszadeh, "An overview of renewable energies in Iran," *Renew. Sustain. Energy Rev.*, vol. 24, no. 2013, pp. 198–208, 2013.

[19] M. A. Mustapa, O. B. Yaakob, Y. M. Ahmed, C. K. Rheem, K. K. Koh, and F. A. Adnan, "Wave energy device and breakwater integration: A review," *Renew. Sustain. Energy Rev.*, vol. 77, no. September 2015, pp. 43–58, 2017.

[20] A. Al-Habaibeh, D. Su, J. McCague, and A. Knight, "An innovative approach for energy generation from waves," *Energy Convers. Manag.*, vol. 51, no. 8, pp. 1664–1668, 2010.

[21] F. He, Z. Huang, and A. W. Law, "An experimental study of a floating breakwater with asymmetric pneumatic chambers for wave energy extraction," *Appl. Energy*, vol. 106, pp. 222–231, 2013.

[22] J. M. B. P. Cruz and A. J. N. A. Sarmento, "Sea state characterisation of the test site of an offshore wave energy plant," *Ocean Eng.*, vol. 34, no. 5–6, pp. 763–775, 2007.

[23] J. P. Kofoed, P. Frigaard, E. Friis-Madsen, and H. C. Sørensen, "Prototype testing of the wave energy converter wave dragon," *Renew. Energy*, vol. 31, no. 2, pp. 181–189, Feb. 2006.

[24] I. López, J. Andreu, S. Ceballos, I. Martínez de Alegría, and I. Kortabarria, "Review of wave energy technologies and the necessary power-equipment," *Renew. Sustain. Energy Rev.*, vol. 27, pp. 413–434, Nov. 2013.

[25] D. Khojasteh, D. Khojasteh, R. Kamali, A. Beyene, and G. Iglesias, "Assessment of renewable energy resources in Iran; with a focus on wave and tidal energy," *Renew. Sustain. Energy Rev.*, vol. 81, no. December 2016, pp. 2992–3005, 2018.

[26] S. Hadadpour, A. Etemad-Shahidi, E. Jabbari, and B. Kamranzad, "Wave energy and hot spots in Anzali port," *Energy*, vol. 74, pp. 529–536, 2014.

[27] M. Majidi Nezhad, D. Groppi, and G. Piras, "Nearshore Wave Energy Assessment of Iranian Coastlines," pp. 1–8, 2018.

[28] R. Alamian, R. Shafaghat, S. S. Hosseini, and A. Zainali, "Wave energy potential along the southern coast of the Caspian Sea," *Int. J. Mar. Energy*, vol. 19, pp. 221–234, 2017.

[29] B. Kamranzad, A. Etemad-Shahidi, and V. Chegini, "Sustainability of wave energy resources in southern Caspian Sea," *Energy*, vol. 97, pp. 549–559, 2016.

[30] A. Saket and A. Etemad-Shahidi, "Wave energy potential along the northern coasts of the Gulf of Oman, Iran," *Renew. Energy*, vol. 40, no. 1, pp. 90–97, 2012.

[31] T. Whittaker and M. Folley, "Nearshore oscillating wave surge converters and the development of Oyster," *Philos. Trans. R. Soc. A Math. Phys. Eng. Sci.*, vol. 370, no. 1959, pp. 345–364, 2012.

[32] D. P. Cashman, M. G. Egan, and J. G. Hayes, "Modelling and Analysis of an Offshore Oscillating Water Column Wave Energy Converter," *Measurement*, pp. 1–10, 2009.

[33] L. Wang, A. Kolios, L. Cui, and Q. Sheng, "Flexible multibody dynamics modelling of point-absorber wave energy converters," *Renew. Energy*, vol. 127, pp. 790–801, 2018.

[34] Bevilacqua.G and Zanuttigh.B, "Overtopping Wave Energy Converters : general aspects and stage of development," *Int. Coast. Eng. Proc.*, no. 1, p. 21, 2011.

[35] L. Rusu and C. Guedes Soares, "Wave energy assessments in the Azores islands," *Renew. Energy*, vol. 45, pp. 183–196, 2012.

[36] G. Kim, W. M. Jeong, K. S. Lee, K. Jun, and M. E. Lee, "Offshore and nearshore wave energy assessment around the Korean Peninsula," *Energy*, vol. 36, no. 3, pp. 1460–1469, 2011.

[37] Danish Hydraulic Institute (DHI), "Mike 21 Wave Modelling," *Dhi*, pp. 1–18, 2009.

[38] L. B. M. Andersen M, Argyriadis K, Butterfield S, Fonseca N, Kuroiwa T, "Ocean Wind and Wave Energy Utilization," vol. 2, no. August, 2006.

[39] M. Previsic, "Wave power technologies," Proc. 2005 *Int. Conf. Futur. power Syst. IEEE*, 2005.

[40] S. M. Polinder H, "Wave energy converters and their impact on power systems," *Proc. 2005 Int. Conf. Futur. power Syst.*, pp. 1–9, 2005.

[41] A. Clément et al., “Wave energy in Europe: current status and perspectives,” *Renew. Sustain. Energy Rev.*, vol. 6, no. 5, pp. 405–431, 2002.

[42] C. Retzler, “Measurements of the slow drift dynamics of a model Pelamis wave energy converter,” *Renew. Energy*, vol. 31, no. 2, pp. 257–269, Feb. 2006.

[43] J. Peter and P. Bak, “Near-Shore Floating Wave Energy Converters,” *Coast. Eng.*, 2011.

[44] A. Pecher, J. P. Kofoed, and T. Larsen, “Experimental Study of the Weptos Wave Energy Converter,” *31th Int. Conf. Ocean. Offshore Arct. Eng. OMAE*, pp. 1–11, 2012.

[45] V. Heller, J. Chaplin, and F. Farley, “Physical model tests of the anaconda wave energy converter,” *Proc. 1st IAHR Eur. Congr.*, vol. 1, pp. 3–8, 2000.

[46] M. Ruellan, H. Ben Ahmed, B. Multon, C. Josset, A. Babarit, and A. H. Clément, “Design Methodology for a SEAREV Wave Energy Converter,” *IEEE Trans. Energy Convers.*, vol. 25, no. 3, pp. 760–767, 2010.

[47] S. Duck, “Edinburgh Wave Power Group, Salter Duck.” [Online]. Available: http://www.mech.ed.ac.uk/research/wavepower/.

[48] T. W. Thorpe, “A Brief Review of Wave Energy,” *Tech. Rep. ETSU-R120*, no. May, p. 200, 1999.

[49] T. Mäki, M. Vuorinen, T. Mucha, and T. Waveroller, “WaveRoller – One of the Leading Technologies for Wave Energy Conversion,” *5th Int. Conf. Ocean Energy*, no. November, pp. 4–6, 2014.

[50] T. Whittaker, D. Collier, M. Folley, M. Osterried, and A. Henry, “The development of Oyster - A shallow water surging wave energy converter ,” *7th Eur. Wave Tidal Energy Conf.*, no. January 2017, 2007.

[51] F. Zabihian and A. S. Fung, “Review of marine renewable energies: Case study of Iran,” *Renew. Sustain. Energy Rev.*, vol. 15, no. 5, pp. 2461–2474, 2011.

[52] B. S. Holmes B, “State of the Art Analysis - A Cautiously Optimistic Review of the Technical Status of Wave Energy Technology,” *EU Proj. Rep.*, pp. 1–111, 2009.

[53] M. Previsic, R. Bedard, and G. Hagerman, “E2I EPRI Assessment Offshore Wave Energy Conversion Devices,” *E2I EPRI WP – 004 – US – Rev* 1, pp. 1–52, 2004.

[54] J. Weber, F. Mouwen, a. Parish, and D. Robertson, “Wavebob – Research & Development Network and Tools in the Context of Systems Engineering,” Ewtec, no. *Proc. of the 8th European Wave and Tidal Energy Conf.*, Uppsala, Sweden, pp. 416–420, 2009.

[55] M. Prado, “Archimedes wave swing (AWS),” *Ocean wave energy, Springer, Berlin*, pp. 297–304, 2008.

[56] J. F. Childs, “THE ROLE OF CONVERTERS & THEIR CONTROL IN THE RECOVERY OF WAVE & WIND ENERGY,” *Proc. IEE Colloq. power Electron. Renew. energy*, vol. 43, no. 1, pp. 23–25, 1997.

[57] T. J. T. Whittaker, W. Beattie, M. Folley, C. Boake, a Wright, and M. Osterried, “The Limpet Wave Power Project – The First Years Of Operation,” *Scottish Hydraul. Study Gr. - Semin. Hydraul. Asp. Renew. Energy*, no. 1997, pp. 1–8, 2004.

[58] Y. Torre-Enciso, I. Ortubia, L. I. López de Aguileta, and J. Marqués, “Mutriku Wave Power Plant: from the thinking out to the reality,” *8th Eur. Wave Tidal Energy Conf.* (EWTEC 2009), pp. 319–328, 2009.

[59] Y. Washio, H. Osawa, and T. Ogata, “The open sea tests of the offshore floating type wave power device ‘mighty whale’ - Characteristics of wave energy absorption and power generation,” *Ocean. Conf. Rec.*, vol. 1, pp. 579–585, 2001.

[60] J. P. Kofoed, P. Frigaard, E. Friis-Madsen, and H. C. Sørensen, “Prototype testing of the wave energy converter wave dragon,” *Renew. Energy*, vol. 31, no. 2, pp. 181–189, 2006.

[61] de O. F. A. Evans DV, *Hydrodynamics of ocean wave-energy utilization*. 1985.

[62] D. Vicinanza, L. Margheritini, J. P. Kofoed, and M. Buccino, “The SSG wave energy converter: Performance, status and recent developments,” *Energies*, vol. 5, no. 2, pp. 193–226, 2012.

[63] G. Mattiazzo and A. Gulisano, “Wave energy future,” 2016.

[64] “WEPTOS Company Website.” [Online]. Available: http://www.weptos.com/.

INTERNATIONAL JOURNAL OF
COASTAL & OFFSHORE ENGINEERING

IJCOE Vol.6/No.5 /Autumn 2021 (51-63)/ **Special issue of "Marine Renewable Energy"**

Available online at: www. Ijcoe.org

Wave Energy Assessment in Dumaran Island, Palawan, Philippines.

Arinah Mariam Aminudin[1*], Teh Hee Min[2], Jonathan Pacaldo[3]

[1*] *BEng. student, Civil and Environmental Engineering Department, Universiti Teknologi PETRONAS; arinahaminudin@gmail.com*
[2] *Senior Lecturer, Civil and Environmental Engineering Department, Universiti Teknologi PETRONAS; heemin.teh@utp.edu.my*
[3] *Senior Lecturer, Civil Engineering Department, Palawan State University; j_pacaldo@psu.palawan.edu.ph*

ARTICLE INFO

Article History:
Received: 25 Sep. 2021
Accepted: 28 Nov. 2021

Keywords:
Dumaran
Palawan
MSLWW3TC
Wave energy
Wave height

ABSTRACT

Wave energy harvesting, if viable, is a potential energy resource for remote islands like Dumaran Island, Philippines. However, absence of high-resolution wave energy resource information in Dumaran waters hinders the development of Wave Energy Converter (WEC) to overcome current unsustainable means of supplying power, prolonging energy insecurity among its locals. The focus of this study is to assess wave energy densities for Dumaran Island using high-resolution and validated wave data for the selected sites in Sulu Sea within 100 km radius from the island by using statistical analysis. This was achieved by generating 3-hourly hindcast wave data for 40-year study period (1978 – 2018) in 6 selected sites, using MetOcean Solutions Ltd WW3 Tolman Chalikov (MSLWW3TC) numerical wave model. The wave model was then validated with MIKE 21 Spectral Wave Model FM (MIKE21SW), which generated 3-hourly wave energy data at 14 sites for 5-year study period. Subsequently, wave energy flux time-series was computed and statistically analysed. The validated wave model resulted in low RMSE and high CC results, which indicate good model performance. The study area has low wave energy content, with the average wave energy range less than 4.5 kW/m. High but unstable wave energy was observed during Northeast Monsoon across all sites, and reduction of wave energy near coastal areas due to sheltering effect of Palawan and offshore islands. The hotspot for wave energy is found in the northeast and southeast of Dumaran deep offshore waters, with average annual wave energy of 4.43 kW/m. As mean wave energy at the site is insufficient and grid connection is absent WEC implementation in Dumaran waters is not viable.

1. Introduction

With increasing energy demand in the 21st century, off-grid rural islands like the Dumaran Island face unique challenges to energy accessibility and sustainability. In the Philippines, accessibility to sustainable energy has been a long-standing goal especially as it faces unique challenges as an island country. Nevertheless, the nation had delivered 94.6% electrification rate by 2018 [1]. Despite the significant progress, energy poverty is still a matter of great concern in the Philippines.

The Dumaran Island is located northeast of the Palawan province, grouped under the Luzon Island group, as shown in Figure 1 below. The island is enclosed within the Sulu Sea with an approximate area of 435km^2, and a total coastline length of 166.17km [2]. Considering the majority coastal communities, renewable energy generated from wave power farms may make an excellent candidate as a resource base [3]. Despite this, wave energy has remained untapped and largely delayed in terms of its development of estimating potential wave resource. The absence of high-resolution wave energy resource information in Dumaran waters hinders the development of Wave Energy Converter (WEC) to overcome current unsustainable means of supplying power to the island, since the potential location for optimal deployment of WEC could not be identified nor quantify the wave energy density in its vicinity.

Figure 1 Location of Dumaran Island, Palawan, Philippines [9].

Hence, the project aims to further assess statistical analysis of wave energy resources using high-resolution wave data particularly within Dumaran waters with respect to previous literature studies of nearby locations for wave energy assessment methodology, as follows:

1) To assess wave energy densities for Dumaran Island using high-resolution wave data for the selected sites in Sulu Sea within 100 km radius from the island using statistical analyses.
2) To validate the statistical results with the MIKE21 numerical results.

There is insufficient high-resolution wave energy resource information in semi-enclosed seas, and the effects of Palawan Island during monsoon seasons. The global wave power resource map by Mørk and others [4] can be compared to a similar study by Cornett [5]. Global wave energy resources had been derived similarly for 10-year period from 1997 to 2006. In this literature, WAVEWATCH-III (NWW3) wind-wave model was used to derive the analysis of wave climate predictions. the wave energy distribution in Dumaran waters differ between the two literatures. Accordingly, average annual wave energy near Dumaran waters generally ranges within 10 kW/m [5], and 5 kW/m [4]. There are some discrepancies between the resource map as wave climate predictions had not been accounted for semi-enclosed inland seas. Furthermore, the author admits the inability of the grid to properly account shallow water effects near most coastlines, making the results less reliable. As WEC deployment near coastline would also like to be considered, the above wave energy flux becomes less reliable.

Literatures in South China Sea also shows sheltering effects and monsoon seasonal winds effects on wave energy, which pattern is not known in Dumaran waters. The presence of offshore islands obstructs the wave propagation, which is referred as sheltering effect. In effect, it reduces the significant wave height [6] which greatly influences the wave energy flux. In the context of Dumaran Island, this sheltered effect could be induced by the presence of Palawan Island itself as well as several other offshore islands within the Sulu Sea. Similar effects could be exemplified within the South China Sea, whereby the presence of small offshore islands tend to decrease wave energy. Several sheltered areas in the South China Sea in a study by Mirzae and others [7] found to be less energetic and has lower probability for the wave power to exceed 5 kW/m at any season. Seasonality throughout the monsoon cycles affects the wave power distribution and stability in the study area. This is important because the stability of wave energy is also a prerequisite to optimize WEC efficiency and performance [8], and the stability of wave power findings in South China Sea may pave the way to acquire information on wave power stability in Dumaran waters. The consistent findings between literatures [7-10], shows that wave energy flux are the highest during winter due to stronger northeaster wind. The central catalyst of this study is based on Quitoras and others [11], in which the technical and economic feasibility of wave energy resource farming were studied across 47 sites in 5 regions in Philippines; The result of the research shows that 10 – 20 kW/m wave energy flux across various Philippines' Northeast coasts. Nevertheless, the authors had acknowledged the limitations to this finding, as it relied on forecasts of publicly available wave profile data sets. need for measures to refine the data with longer data source. Improvements can be made by taking 10 years or more data source with 3 hours interval per day to increase reliability of the results, as authors push forward more research to be done for more detailed wave resource maps.

Based on the literature review, research gap includes the discrepancies between global wave energy resource maps, constraints in numerical wave models to account enclosed seas, and lack of information regarding precise wave energy near Dumaran Island and seasonality and sheltering effects on waves in Sulu Sea.

2. Methodology

The assessment methodology is based on International Energy Commission Technical Specification of Wave Energy Resource Assessment and Characterisation (IEC TS 62600-101), to ensure standardised and accurate wave energy resource estimation [12]. Procedure flowhart is shown in Figure 3.

2.1 Site Selection

The number and identification of reference sites, or data points, depends of the spatial variability of the study area [13] in terms of spatial variation includes distance to shore, difference in water depths, and presence of offshore islands. Nevertheless, the identification of the reference sites is practically an iterative procedure [13], as spatial variation of study area and its corresponding wave parameters could only be identified after defining the reference sites. Thus, descriptive statistical analysis was conducted to check whether there is sufficient variability after wave data sets acquired [14]. The statistical difference was evaluated using R whether there are any similarities in terms of mean, standard deviation (SD), maximum (Max.), range, skew, kurtosis of the wave data and whether the wave data at the corresponding sites overlap with each other from the correlation matrix [14]. All reference sites are within 100 km radius to ensure that sites are accessible to the island, shown in Figure 2. The terms also indicate shallow water, less than 100m, and deep water, ranging from 100 – 1000 m, respectively. Overall, there are total of 14 sites selected. Among the reference sites, the wave data at 6 offshore sites, denoted as sites 1 – 6, were acquired from MSL WW3 TC numerical wave model. More data points were taken due to the large variation in water depth and other geographical factors in the study site. Subsequently, to account several nearshore and offshore areas, sites A – H were selected. The corresponding coordinates, distance to shore, water depth and data source are summarised in Table 1.

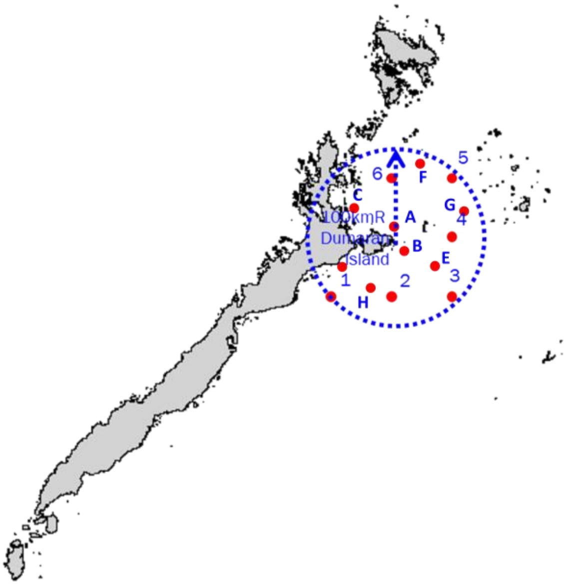

Figure 2 Reference site locations map

Table 1 Reference site location and data source details.

Site	Coordinates		Distance to shore	Depth (m)	Data source
	Lat.	Long.			
1	10˚00’05”	119˚29’57”	Offshore	< 50	MSL WW3 TC
2	10˚00’03”	119˚59’58”		> 500	
3	10˚00’05”	120˚30’01”		> 1000	
4	10˚30’03”	120˚29’58”		< 100	
5	11˚00’01”	120˚29’58”		< 100	
6	11˚00’05”	119˚59’54”		< 100	
A	11˚00’05”	119˚59’54”	Near-shore	< 100	MIKE21SW
B	11˚00’05”	119˚59’54”		< 100	
C	10˚38’25”	119˚44’04”		< 100	
D	10˚22’43”	119˚43’12”		< 50	
E	10˚18’46”	120˚14’15”	Offshore	> 1000	
F	11˚02’17”	120˚14’49”		< 100	
G	10˚52’44”	120˚28’08”		< 100	
H	10˚05’53”	119˚48’35”		> 250	

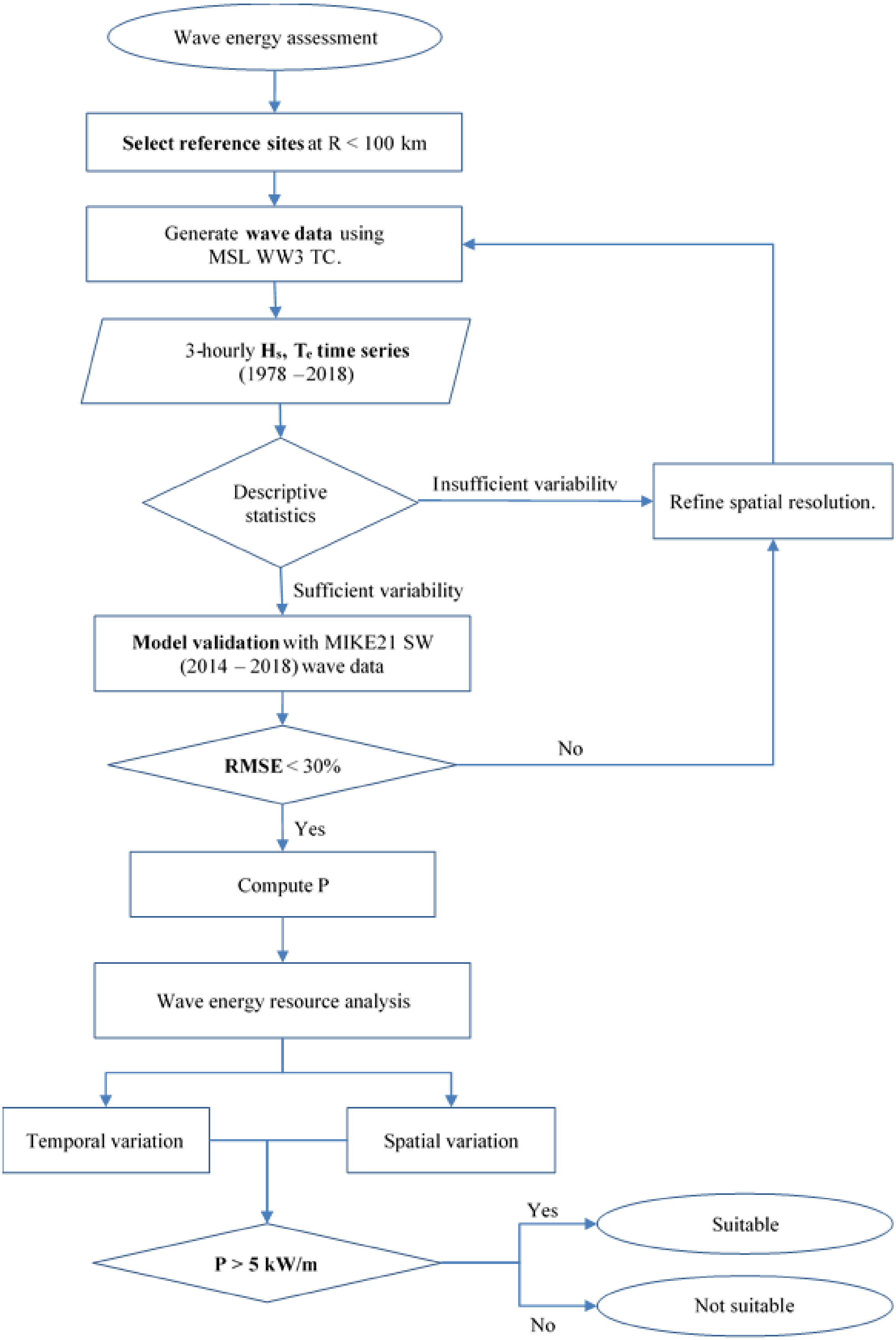

Figure 3 Flowchart for wave energy assessment in Dumaran waters.

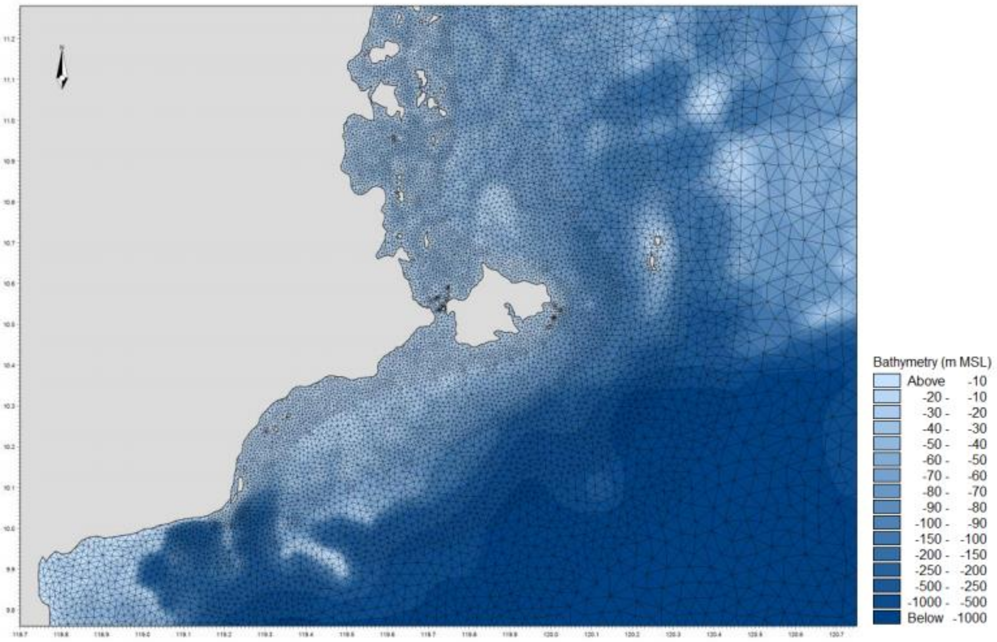

Figure 4 Dumaran waters' bathymetry based on Dr. Nik and Associates

2.2 Wave model and validation

In this study, the wave parameters such as significant wave height and energy period generated using MetOcean Solutions Ltd WW3 Tolman Chalikov (MSL WW3 TC) numerical wave model was provided by Palawan State University. Accordingly, the wave simulation was carried out for 40-year period between 1978 – 2014, and setup to output 3-hourly significant wave height, mean wave period and mean wave direction for the entire simulation period. Meanwhile, the MSL WW3 TC also had high spatial resolution of about 38 km [7]. The wave model was forced by high resolution NOAA Climate Forecast System Reanalysis (CFSR) winds of approximately 38 km and using the ETOPO2 bathymetry [7].

To ensure the MSL WW3 TC wave model had accurately estimated the wave conditions in Dumaran waters, the wave data were validated using MIKE21 SW, since the measured wave buoy data was unavailable. Accordingly, the wave parameters used to validate the MSL WW3 TC numerical model is significant wave height and wave power, whereby the wave data outputs 3-hourly for 5-year study period between years 2014 – 2018 at the corresponding 6 offshore sites (1 – 6), for model validation purposes. It is important to note that, the temporal coverage of 5 years was selected to reasonably estimate inter-annual variability of average wave power [13] and reduce uncertainties from the MSL WW3 TC wave model.

In terms of the means of model validation, comparison could be made between the two numerical wave models as the spatial resolution of the MIKE21SW model is much more refined. The wave model was set up with an unstructured triangulated mesh was generated with varying spatial resolution that progressively increases from offshore boundaries towards the study area. The wave model has a resolution of approximately 5 km at the offshore boundaries and increased to about 1 km in the vicinity of Dumaran Island.

Like the MSL WW3 TC, the wave model was also forced by Climate Forecast System Reanalysis (CFSR) wind field with spatial resolution of approximately 0.2° x 0.2°. Bathymetry data of the wave model was obtained from the General Bathymetric Chart of the Oceans (GEBCO) gridded bathymetric data set with resolution of approximately 900 m. Therefore, wave data generated from MIKE21SW model may be more accurate to validate MSL WW3 TC wave data with, due to its refined spatial resolution. The comparison between the wave models could be represented in hindcast wave height time-series of both models between January 2018 to December 2018 as a case study. Nevertheless, the RMSE and CC for wave height and period from the numerical models was computed for the 5-year model validation study period, in which the maximum allowable RMSE for Class 2 wave energy assessment is 30% [12]. The RMSE and CC equation is as follows in Equation (1) and (2) whereby x_i refers to the wave parameter at ith time from MSL WW3 TC, and y_i refers to the wave parameter at ith time from MIKE21 SW.

While further discussion regarding statistical differences between sites 1 – 6 as found in Section

0, the sites (A – H) are included as reference sites for the purpose of fully refining spatial variability of wave energy resource within Dumaran waters and accounting locations that are nearshore and with more variable in water depths.

$$CC = \frac{\sum_{i=1}^{n}(x_i - \bar{x})(y_i - \bar{y})}{\sqrt{\sum_{i=1}^{n}(x_i - \bar{x})^2 \sum_{i=1}^{n}(y_i - \bar{y})^2}} \tag{1}$$

$$RMSE = \sqrt{\frac{1}{n}\sum_{i=1}^{n}(x_i - y_i)^2} \tag{2}$$

2.3 Wave energy resource assessment

The numerical wave models generate important parameters, that is significant wave height and energy period, to compute wave power. To give brief context on how these parameters are generated within the linear wave theory framework, vertical wave elevation $\boldsymbol{\eta(r,t)}$ at time t and at any point $\boldsymbol{r(x,y)}$ on the sea surface level, is assumed as superposition of various regular waves to depict random waves [15]. This may also be depicted as being composed of many waves of different frequencies, amplitudes and directions [16]. Meanwhile, wave energy resource is originated from the energy transported from local and distant winds blowing over the ocean surface [15], where more than 95% of the energy transported is found [17].

Relating back to the surface elevation, the spectral density S(f) was derived using Fast Fourier Transform algorithm. Hence, the energy period and significant wave height of the sea state can be computed in Equation (3) and (4) [18]. Accordingly, significant wave height, is denoted as Hm0. In particular, the significant wave height is defined as the average of the one-third of the highest wave height [19]. The variables such as variance density spectrum is denoted as $\boldsymbol{E(\omega,\theta)}$, whereas $\boldsymbol{\omega}$ is denoted as absolute radian frequency. Both parameters are determined by Doppler-shifted dispersion relationship [16]. It must be noted that the significant wave height may be also be assumed as the wave height in the energy domain [11], as shown in Equation (5).

Meanwhile, the energy Period, denoted as Te, refers to the mean period of non-directional variance density spectrum. However, as the spectral shape is not provided, relationship between Te with the peak period, Tp, is shown in Equation (6), whereby α is 0.86 which is the coefficient in relation to the Pierson-Moskowitz spectrum [20]. This assumption may result to more conservative wave power but are less significant than errors in wave height as $\boldsymbol{P \propto T_e H_s^2}$. Hence, the energy domain wave height and wave period are derived from the numerical wave models, in the form of hindcast historical time series.

$$H_s = 4\sqrt{\int_0^{2\pi}\int_0^{\infty} E(\omega,\theta)\,d\omega d\theta} \tag{6}$$

$$T_e = 2\pi \frac{\int_0^{2\pi}\int_0^{\infty} \omega^{-1}E(\omega,\theta)\,d\omega d\theta}{\int_0^{2\pi}\int_0^{\infty} E(\omega,\theta)\,d\omega d\theta} \tag{3}$$

$$H_{m0} \sim H_s \tag{4}$$

$$T_e \sim \alpha T_p \tag{5}$$

Hence, the wave power is expressed in terms of energy flux per unit crest of wave spectrum. This quantity is a unit of measurement to represent the energy content at respective locations, and is a function of significant wave height and energy period as shown in Equation (7). The equation had been simplified under deep water condition [7] and is justified, considering that all water depths at all extraction points exceed 10 m from the shore [20]. Thus, the wave energy flux can be calculated as follows:

$$P = \frac{\rho g}{64\pi} H_{m0}^2 T_e = 0.491 H_{m0}^2 T_e \tag{7}$$

It is important to note that, for the amount of available wave energy resource to be harvestable, the supply must be sufficient and steady [5]. While there is no particular consensus on minimum wave energy resource that would be deemed as ‘harvestable’, generally considers wave energy flux less than 5 kW/m to be low, thus WEC deployment is not viable [21]. Hence, as the annual average wave power is derived for each site, a viable site for WEC deployment should generally have higher that 5 kW/m of wave energy flux. Otherwise, WEC implementation is not recommended. Besides, the temporal variation of wave energy resource in this study is also represented in terms of the steadiness of wave energy flux, to consider any extreme wave events. The daily and annual variation of wave energy flux variation across the study period was assessed based on the Coefficient Variation (CV). Hence, CV was calculated to check the stability of the wave energy resource supply, based on the ratio of annual standard deviation of the wave power time series, $\sigma[P(t)]$, and the annual average wave power, $\mu[P(t)]$ as shown in Equation (8) [5].

Overall, the temporal variation of wave energy resource in this study is represented in the form of wave energy flux time-series to acquire daily and annual average wave energy flux as well as the coefficient of variability.

$$CV = \frac{\sigma[P(t)]}{\mu[P(t)]} \tag{8}$$

3. Results and Discussion

Overall, based on the descriptive statistics conducted on the 6 offshore sites, the significant wave height datasets at spatially distant sites vary considerably, but does not account for nearshore areas. Based on the wave model validation at sites 1 – 6, RMSE for significant wave height and peak wave period are generally low and high correlation coefficient, which indicates good simulation performance in exception to site near the presence of offshore islands. Based on the temporal variability of wave energy resource, higher wave energy flux occurs during Northeast Monsoon. Based on the spatial variability of wave energy resource provided by DNA, there is higher wave energy resource in the offshore regions northeast and southeast of Dumaran Island as opposed to nearshore coastal regions. Despite this, the highest amplitude of average wave energy can only reach up to 3.5 kW/m. Hence, the wave energy flux acquired is compared to the global wave energy distribution [5] [4] and in nearby regions in Philippines [11]. Ultimately, the impact on wave energy harvesting viability in Dumaran waters is further discussed.

3.1. Statistical comparison between wave data

Accordingly, the statistical differences for the wave data reveals the extent of variability between the sites. Hence, wave height data at the 6 sites, as generated from MSL WW3 TC, were evaluated whether there are sizable differences between each site based on descriptive statistics and correlation matrix, ensuring that the extraction points represent the spatial variability of the site.

The summary of descriptive statistics is shown in Figure 5, whereas the correlation matrix is shown in Figure 6. The corresponding descriptive statistical analysis using R presents the statistical comparison between sites based on the mean, SD, maximum (Max.), range, skew, and kurtosis of significant wave heights at each site in Table 2. Overall, significant wave heights between the sites are generally varied but show some correlation to other sites in its vicinity due to the similarities in water depth, distance to shore and presence of offshore islands.

Table 2 Summary of descriptive statistics at Site 1-6

Site	Mean	SD	Max.	Range	Skew.	Kurtosis
1	0.47	0.46	4.10	4.10	1.44	2.31
2	0.59	0.56	5.40	5.40	1.35	1.94
3	0.60	0.56	6.60	6.60	1.37	2.45
4	0.62	0.57	7.30	7.30	1.22	1.77
5	0.69	0.61	7.10	7.10	0.94	0.62
6	0.47	0.46	4.10	4.10	1.44	2.31

Some statistical similarities can be observed for sites that are subject to similar distance to shore and subject to similar sheltering effects. This can be observed based on the mean of significant wave heights across the sites, whereby it varies between 0.47 m to 0.69 m. Notably for site 1 and site 6, both sites have similarly low mean significant wave height and lowest standard of deviation. This might be due sheltering effect from the presence of the Palawan Island and offshore islands, respectively. Consequently, both sites are less prone to be subject to extreme peak wave heights. This is corroborated by their low range, positive skewness, and positive kurtosis.

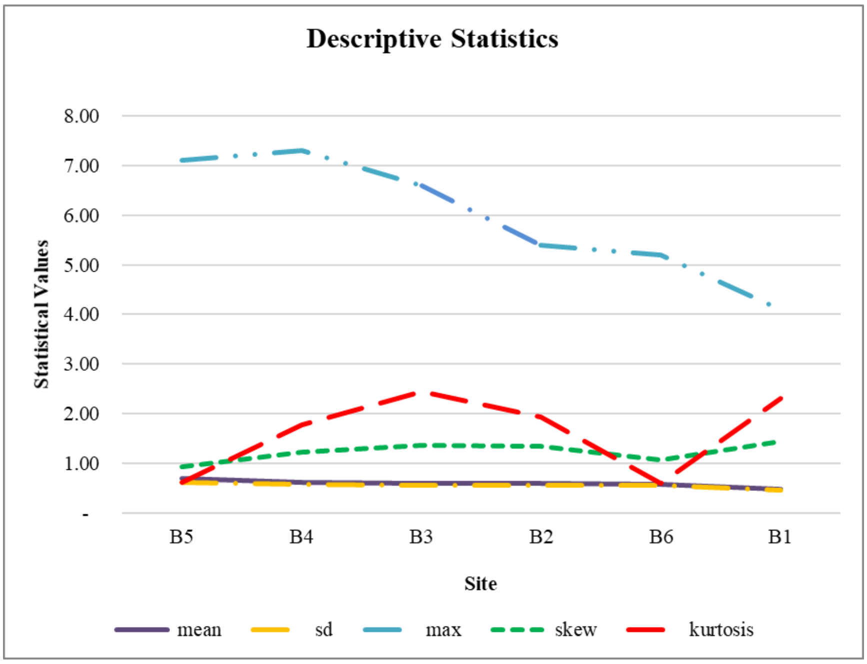

Figure 5 Descriptive statistics at each site

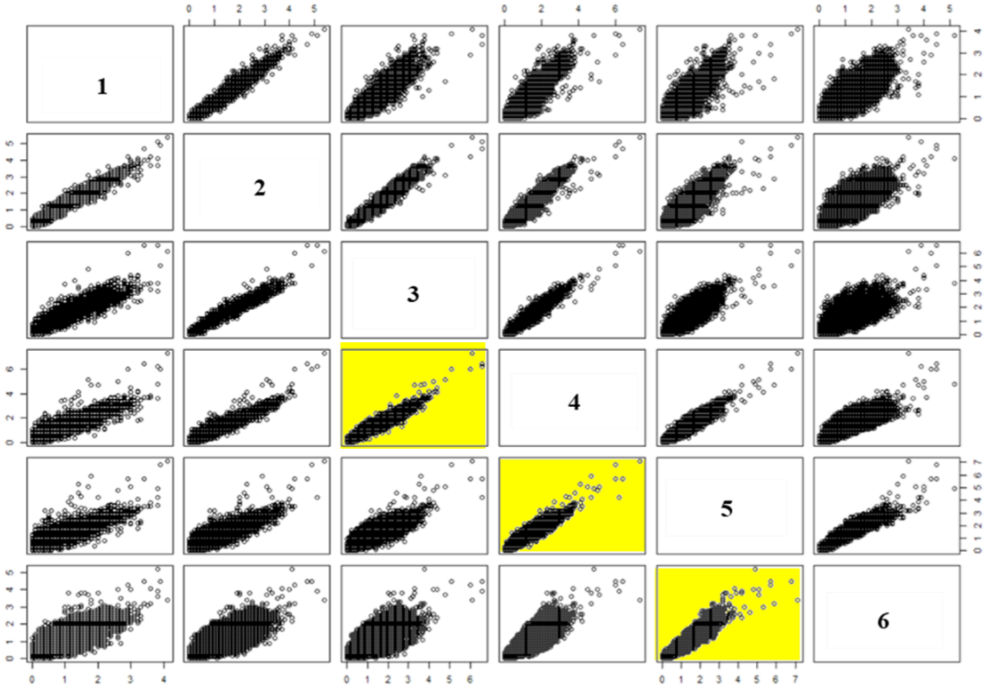

Figure 6 Correlation matrix of wave heights (bottom left) and wave period (top right) at site 1 – 6 for 40 years.

The highlighted cells, namely between site 3 and 4, site 4 and 5 alongside site 5 and 6, shows high correlation of significant wave heights. Site 3, 4, and 5 may correlate as it has similar water depth. However, due to the presence of offshore islands near both sites 4 and 6, it is important to consider this geographical variability. Essentially, there are some correlation and statistical similarities between the sites that are either in proximity to each other, or subject to similar water depth and sheltering effects from offshore islands. Nevertheless, the sites differ in other factors thus is important to be represented in the assessment. It was also noted that sites 1 – 6 had not represent area near coastal, thus the additional reference point using MIKE21SW (A – H) was justified.

3.2. Wave model validation

With exception to site 6, the MSL WW3 TC model simulation corresponds well with the more extensive simulation by MIKE21SW in terms of Root-Mean-Square error (RMSE) and correlation coefficient (CC). The corresponding RMSE and CC for significant wave height and wave period is present in Table 3 and Table 4. Overall, the RMSE values for significant wave height ranges between 0.26 m to 0.42 m. Whereas the CC for significant wave height corresponds very well ranging between 90% to 93%. As for the peak wave period, the RMSE values range between 1.25 s to 1.38 s and CC ranges between 62% to 74% for site 1 – 5. On the other hand, it is observed that there are high uncertainties in site 6 for both wave height and wave period. The high uncertainty especially for wave period at site 6 also results to high RMSE at 1.83 s. This high uncertainty may be due to the location of site 6 at relatively shallower seabed and subject to surrounding offshore islands.

To visualise the comparison between the wave models, time-series comparison for hindcast significant wave height and wave period generated between MSL WW3 TC and MIKE21SW, as shown in Figure 7. Overall, considering the RMSE, CC and time-series comparison to MIKE21SW, the MSL WW3 TC model shows good correlation in terms of wave height and wave period. This indicates good model performance and is reliable for the wave energy assessment.

Table 3 RMSE and CC values for significant wave height, Hm0.

Site	RMSE (m)	CC (%)
1	0.26	91
2	0.34	93
3	0.32	93
4	0.36	93
5	0.40	93
6	0.42	90

Table 4 RMSE and CC values for peak wave period Tp

Site	RMSE (s)	CC (%)
1	1.25	66
2	1.38	62
3	1.25	72
4	1.21	74
5	1.29	68
6	1.83	48

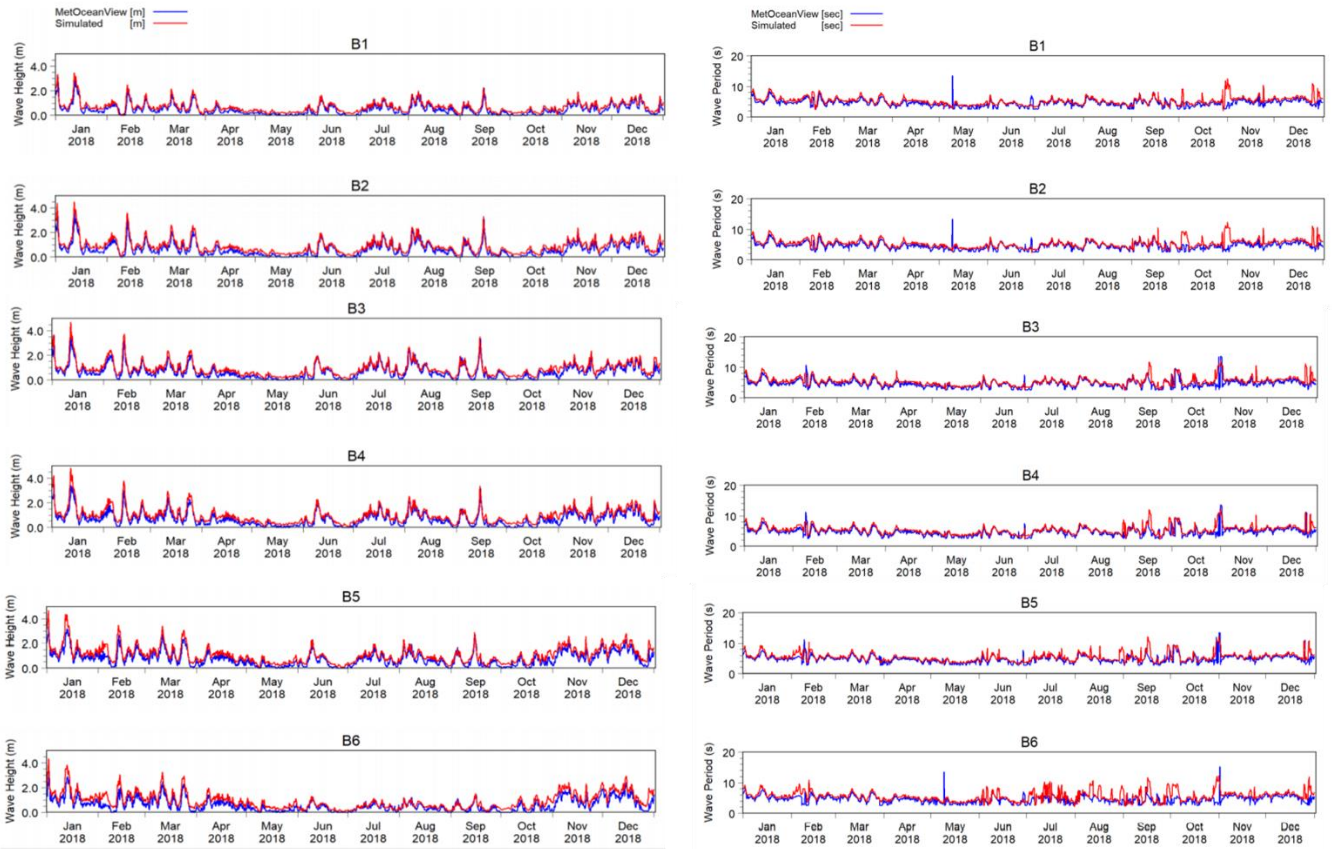

Figure 7 Comparison of hindcast significant wave height and wave period between MSL WW3 TC and MIKE21SW.

3.3 Wave energy resource temporal variability

Wave energy in Dumaran waters was found to be generally low, stable from year to year but extreme during winter monsoon season. As wave data was generated, its corresponding time series delineates how it varies inter-annually and intra-annually within the study period [13], indicating its mean value as summarised in Table 5 and in bar chart Figure 8, together with the inter-annual SD and CV.

The overall wave energy flux at these sites tends to be low between 0.77 kW/m to 4.43 kW/m. Based on Figure 9 – 11, wave energy at all sites can be described as ‘choppy’ throughout 40-year study period. This is because the wave energy rise and fall quickly and remains low, which may be due to the larger scale of sheltering effects from surrounding terrains [6], as the Sulu sea is semi-enclosed. For sites nearshore or near small offshore islands, this effect may cause the wave energy to be much lower. Namely, based on the time series of sites A, B, C and D which are located nearshore in Figure 12, it experiences even and low wave energy during summer monsoon. In effect, their respective mean annual wave energy are lower in comparison to the other sites, at 2.93, 2.96, 1.59 and 0.77 kW/m respectively. Site C and D are in the southwest coast of Dumaran Island, thus experience sheltering effect from the Palawan terrain which significantly reduces wave energy.

Notably though, certain sites experience more drastic peaks during the northeast monsoon, namely sites E, F and G. At these sites, the peaks which occur during the winter season ranges between 30 kW/m to 80 kW/m. In fact, a very drastic increase of wave energy is observed in Dumaran waters during the Northeast Monsoon season. Though maximum wave energy does not govern the WEC deployment, it is equally clear that extreme wave conditions may cause damage to WEC, therefore should not be underestimated.

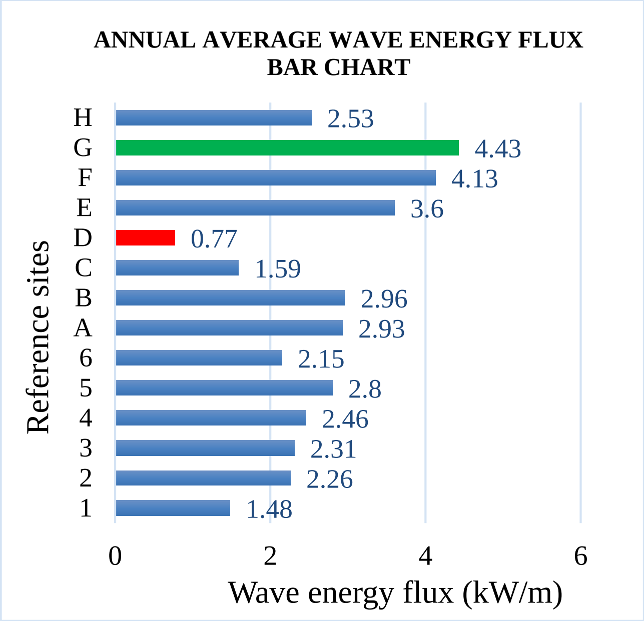

Figure 8 Bar chart of the annual average wave energy flux across all sites.

Table 5 Summary of annual average wave energy flux, maximum wave energy flux, coefficient variation and standard deviation.

Site	Pavg (kW/m)	Pmax (kW/m)	CV (%)	SD
1	1.48	35.46	3%	0.047
2	2.26	50.60	2%	0.043
3	2.31	67.00	2%	0.063
4	2.46	80.24	1%	0.039
5	2.80	57.06	6%	0.196
6	2.15	42.75	4%	0.076
A	2.93	72.58	6%	0.18
B	2.96	71.39	1%	0.04
C	1.59	28.00	8%	0.13
D	0.77	22.09	6%	0.05
E	3.60	90.98	5%	0.17
F	4.13	79.37	6%	0.24
G	4.43	89.92	1%	0.06
H	2.53	66.32	2%	0.05

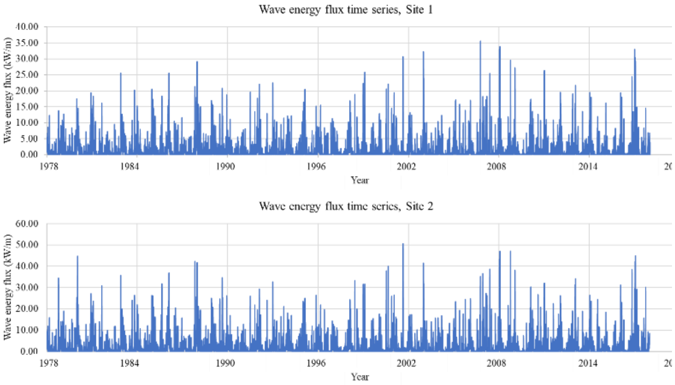

Figure 9 Wave energy flux variation across 40 years (1978 – 2018) at Site 1 and 2.

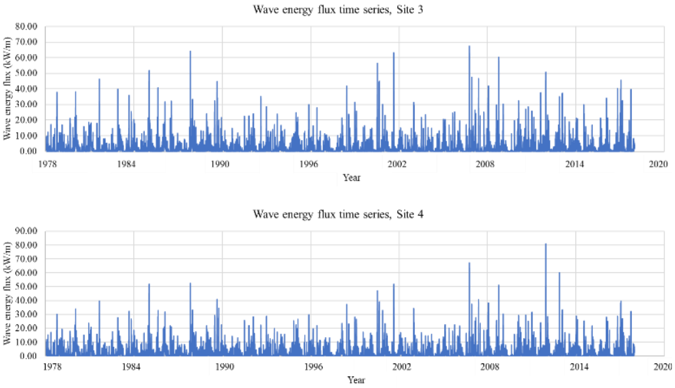

Figure 10 Wave energy flux variation across 40 years (1978 – 2018) at Site 3 and 4.

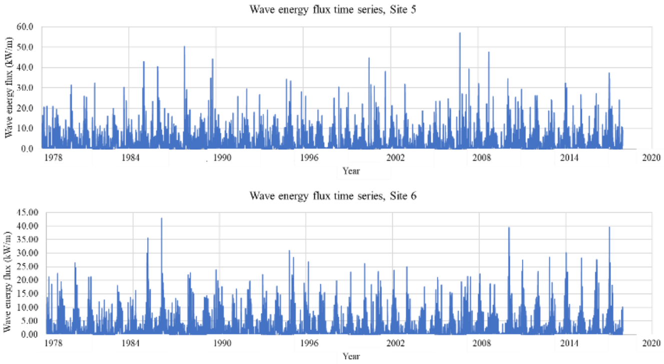

Figure 11 Wave energy flux variation across 40 years (1978 – 2018) at Site 5 and 6.

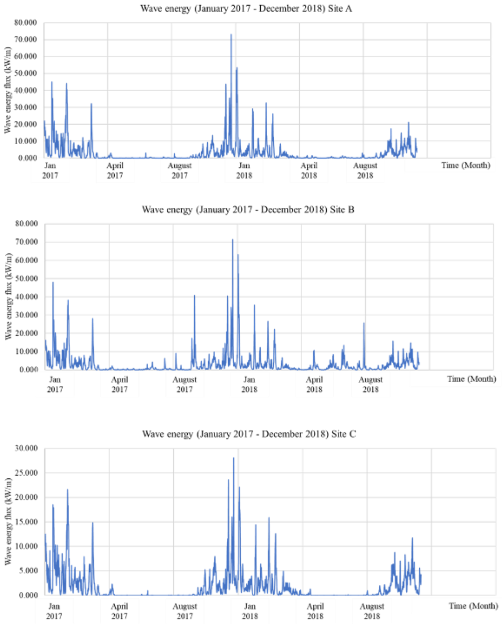

Figure 12 Wave energy flux variation across January 2017 to December 2018 at Site A – C.

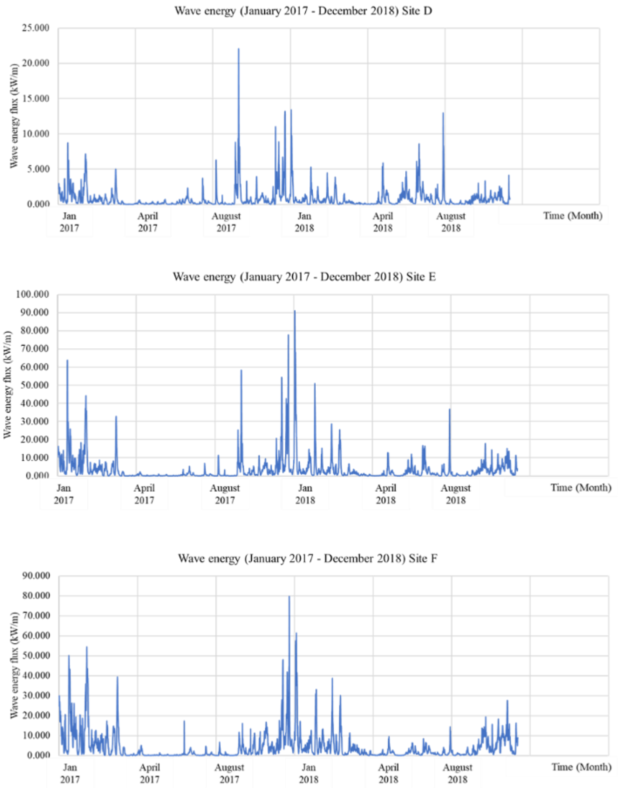

Figure 13 Wave energy flux variation across January 2017 to December 2018 at Site D – F.

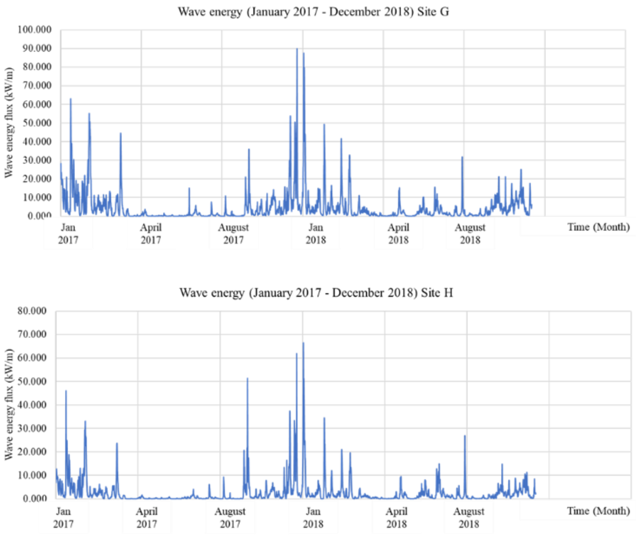

Figure 14 Wave energy flux variation across January 2017 to December 2018 at Site G – H.

3.5 Feasibility of wave energy harvesting in Dumaran waters

Based on the previous analysis, site G was identified with the highest and most stable wave energy flux. The average wave energy that can be harvested in the site is 4.43 kW/m. While there is no consensus on the minimum wave energy flux that is considered harvestable, wave energy flux of greater that 5 – 15 kW/m are usually adopted to be recommended as having potential of WEC [21]. Hence, although site G was the most viable relative to the other sites, there are several challenges in implementing the WEC due to economic and technical issues.

Namely, the technology itself requires high capital expenditures (CAPEX) [11]. This is because the technology is still in its early development stage. While the local demand and price of electricity may drive the profitability of the project [11], this may demand great electricity output from the WEC to ensure that it is economical. With current development of WEC efficiency of 38% for pressure differential WEC at best [23]. Thus, further extraction of energy is not feasible, considering that current wave energy resource is less than 5 kW/m. The wave energy flux at the study site is significantly low in comparison to commonly recommended areas for wave energy generation, which as an average of 15 kW/m of wave energy potential [14]. Other technical and economical challenge also involve the existing infrastructures to connect WEC. However, in this case where the site proposed is in remote offshore, it requires grid connectivity infrastructure. The installation of such grid had been excluded in CAPEX estimation, therefore would incur very high cost.. In practice, without grid connectivity, the WEC deployment in rural regions are simply not viable [24]. Therefore, the lack of grid connection further strains the economics for WEC implementation. Consequently, WEC is not viable within 100 km of Dumaran waters.

4. Conclusions

Pertaining assessment of wave energy density, this study has demonstrated the average annual wave power in Dumaran waters to be below 4.5 kW/m, whereby site G located in offshore northeast of the island was the highest at 4.43 kW/m and the most stable (CV=1%). While the year-to-year variation is generally predictable, the intra-annual variation of wave energy shows uneven extreme peaks during northeast monsoon. On the other hand, deep water offshore regions in the northeast and southeast experience the highest wave energy flux, but only reaches up to 3.6 kW/m – 4.43 kW/m of average annual wave energy. Due to insufficient wave energy flux ($P < 5$ kW/m) and unavailable grid connection, WEC deployment is not economically and technically viable in Dumaran Island.

Meanwhile, the study concluded the model validation by using MIKE21SW numerical results showing good correspondence. The corresponding RMSE and CC values calculated based on significant wave heights and wave periods datasets between MSL WW3 TC and MIKE21SW showed overall good model performance, as RMSE values are less than 30% for both wave height and wave period as per IEC guideline. Conclusively, this study had contributed comprehensive analysis for wave energy density in Dumaran waters with validated wave data

Essentially, this study can be improved by validation of wave model with measured buoy data, expanding study area and research considerations of other marine renewable energy. The buoy measurements were not acquired in this study due to time constraints but is required by IEC standards. While model validation across most sites shows good model performance, areas in shallow seabed areas have higher uncertainties. Thus, should be validated with buoy data. This measure in future works into would further improve the study's reliability.

Besides, further study should be conducted to assess wave energy beyond 100km radius from Dumaran Island. This is recommended as higher wave energy was observed in further and deeper waters located northeast and southeast of the island. Furthermore, as the further offshore sites are far from Palawan terrain and offshore islands, less sheltering may be observed which could result in higher energy content. Consequently, extending the study area, if permitted with availability of grid connectivity infrastructure, may provide sufficient wave energy to Dumaran Island. Otherwise, another approach is venturing to other marine renewable wave energy. Namely, technologies such as OTEC should be researched further for the context of Dumaran waters. Considering the deep basin observed from bathymetry provided, the large depth variation may be favourable for OTEC developments. Hence, further research to venture into the viability of these technologies in Dumaran Island is recommended to overcome energy insecurity of its people. Altogether, further research is necessary in terms of data validation with buoy data, extending study area beyond 100km and consideration of other marine renewable energy technologies.

8. References

[1] W. Bank. "Access to electricity (% of population)." https://data.worldbank.org/indicator/EG.ELC.ACCS.ZS (accessed 14 March, 2021).

[2] PhilAtlas, "Dumaran." [Online]. Available: https://www.philatlas.com/physical/islands/dumaran.html.

[3] D. L. McCollum *et al.*, "Connecting the sustainable development goals by their energy inter-linkages," *Environmental Research Letters,* vol. 13, no. 3, p. 033006, 2018/03/01 2018, doi: 10.1088/1748-9326/aaafe3.

[4] G. Mørk, S. Barstow, A. Kabuth, and M. Pontes, *Assessing the Global Wave Energy Potential*. 2010.

[5] A. Cornett, *A Global Wave Energy Resource Assessment*. 2008.

[6] S. Ponce de Leon, "On the sheltering effect of islands in ocean wave models," *Journal of Geophysical Research,* vol. 110, 09/08 2005, doi: 10.1029/2004JC002682.

[7] A. Mirzaei, F. Tangang, and L. Juneng, "Wave energy potential assessment in the central and southern regions of the South China Sea," *Renewable Energy,* vol. 80, pp. 454-470, 2015/08/01/ 2015, doi: https://doi.org/10.1016/j.renene.2015.02.005.

[8] Y. Lin, S. Dong, Z. Wang, and C. Guedes Soares, "Wave energy assessment in the China adjacent seas on the basis of a 20-year SWAN simulation with unstructured grids," *Renewable Energy,* vol. 136, pp. 275-295, 2019/06/01/ 2019, doi: https://doi.org/10.1016/j.renene.2019.01.011.

[9] G. Lin *et al.*, "Assessment of Wave Energy in the South China Sea Based on GIS Technology," *Advances in Meteorology,* vol. 2017, pp. 1-9, 02/20 2017, doi: 10.1155/2017/1372578.

[10] C.-w. Zheng, J. Pan, and J.-x. Li, "Assessing the China Sea wind energy and wave energy resources from 1988 to 2009," *Ocean Engineering,* vol. 65, pp. 39-48, 2013/06/01/ 2013, doi: https://doi.org/10.1016/j.oceaneng.2013.03.006.

[11] M. R. D. Quitoras, M. L. S. Abundo, and L. A. M. Danao, "A techno-economic assessment of wave energy resources in the Philippines," *Renewable and Sustainable Energy Reviews,* vol. 88, pp. 68-81, 2018/05/01/ 2018, doi: https://doi.org/10.1016/j.rser.2018.02.016.

[12] V. Ramos, R. Carballo, and J. Ringwood, "Assessing the utility and effectiveness of the IEC standards for wave energy resource characterisation," in *Progress in Renewable Energies Offshore: Proceedings of the 2nd International Conference on Renewable Energies Offshore (RENEW2016), Lisbon, Portugal, 24-26 October 2016*: CRC Press, 2016, pp. 27-36.

[13] M. Folley, A. Cornett, B. Holmes, P. Lenee-Bluhm, and P. Liria, *Standardising resource assessment for wave energy converters*. 2012.

[14] J. Doorga *et al.*, "Assessment of the wave potential at selected hydrology and coastal environments around a tropical island, case study: Mauritius," *International Journal of Energy and Environmental Engineering,* vol. 9, 01/18 2018, doi: 10.1007/s40095-018-0259-7.

[15] L. Cuadra, S. Salcedo-Sanz, J. C. Nieto-Borge, E. Alexandre, and G. Rodríguez, "Computational intelligence in wave energy: Comprehensive review and case study," *Renewable and Sustainable Energy Reviews,* vol. 58, pp. 1223-1246, 2016/05/01/ 2016, doi: https://doi.org/10.1016/j.rser.2015.12.253.

[16] B. Liang, F. Fan, Z. Yin, H. Shi, and D. Lee, "Numerical modelling of the nearshore wave energy resources of Shandong peninsula, China," *Renewable Energy,* vol. 57, pp. 330-338, 2013/09/01/ 2013, doi: https://doi.org/10.1016/j.renene.2013.01.052.

[17] B. Drew, A. R. Plummer, and M. N. Sahinkaya, "A review of wave energy converter technology," *Proceedings of the Institution of Mechanical Engineers, Part A: Journal of Power and Energy,* vol. 223, no. 8, pp. 887-902, 2009, doi: 10.1243/09576509jpe782.

[18] A. Osinowo, X. Lin, D. Zhao, and Z. Wang, "Long-Term Variability of Extreme Significant Wave Height in the South China Sea," *Advances in Meteorology*, vol. 2016, pp. 1-21, 01/01 2016, doi: 10.1155/2016/2419353.

[19] R. G. Dean and R. A. Dalrymple, *Water Wave Mechanics For Engineers And Scientists*. World Scientific Publishing Company, 1991.

[20] J. R. S. Doorga *et al.*, "Assessment of the wave potential at selected hydrology and coastal environments around a tropical island, case study: Mauritius," *International Journal of Energy and Environmental Engineering*, vol. 9, no. 2, pp. 135-153, 2018/06/01 2018, doi: 10.1007/s40095-018-0259-7.

[21] ADB, *Wave Energy Conversion and Ocean Thermal Energy Conversion Potential in Developing Member Countries*. Asian Development Bank, 2014.

[22] S. Saincher and J. Banerjee, "Influence of wave breaking on the hydrodynamics of wave energy converters: A review," *Renewable and Sustainable Energy Reviews*, vol. 58, pp. 704-717, 2016/05/01/ 2016, doi: https://doi.org/10.1016/j.rser.2015.12.301.

[23] L. Mofor, J. Goldsmith, and F. Jones, "Ocean Energy: Technology Readiness, Patents, Deployment Status and Outlook," 2014.

[24] S. A. Sannasiraj and V. Sundar, "Assessment of wave energy potential and its harvesting approach along the Indian coast," *Renewable Energy*, vol. 99, pp. 398-409, 2016/12/01/ 2016, doi: https://doi.org/10.1016/j.renene.2016.07.017.

INTERNATIONAL JOURNAL OF
COASTAL & OFFSHORE ENGINEERING

IJCOE Vol.6/No.5 /Autumn 2021 (64-75) / **Special issue of "Marine Renewable Energy"**

Available online at: www. Ijcoe.org

Evaluation of SSG breakwaters on the southern shores of the Caspian Sea to produce sustainable energy

Milad Raoufi[1], Payam Zanganeh Ranjbar[2*], Mirabdolhamid Mehrdad[3]

[1] *MSc in civil engineering, Department of Civil Engineering, Faculty of Engineering, University of Guilan, P.O. 3756, Rasht, Guilan, Iran; R.milad24@gmail.com*
[2*] *Assistant Professor, Department of Civil Engineering, Faculty of Engineering, University of Guilan, P.O. 3756, Rasht, Guilan, Iran; P.zanganeh@guilan.ac.ir*
[3] *Associate Professor, Department of Civil Engineering, Faculty of Engineering, University of Guilan, P.O. 3756, Rasht, Guilan, Iran; Mehrdad@guilan.ac.ir*

ARTICLE INFO

Article History:
Received: 02 July 2021
Accepted: 10 Oct 2021

Keywords:
Caspian Sea
SSG breakwater
Wave energy
Marine energy

ABSTRACT

In this research, objecting to the use of a lesser-known type of energy source, marine wave potential, the application of Sea-wave Slot-cone Generator (SSG) breakwater was investigated in the Caspian Sea. This study had two main objectives. 1) Investigation of the conditions of each of the selected waves in terms of speed factor in the face of this breakwater 2) Investigation of the scattering of different waves in the Bandar Anzali area on the southern shores of the Caspian Sea. About the first goal, eight waves with different characteristics were selected and applied. According to the simulation results, the wave with a height of 2.825 meters and speed of 6.56 m/s and waves with a height of 0.5 and 2.825 meters and speed of 13.02 m/s, with an efficiency of more than 50%, had the highest efficiency among the simulated waves. Nevertheless, in connection with the second goal, by examining the wave height diagram and the diagram of the specified wave period, most of the waves that occurred in the Bandar Anzali region in 100 days are close to the wave with a height of 0.5 meters and speed of 6.56 m/s with an efficiency of about 7%. It does not have an opinion, and the number of waves that occurred with favorable conditions is less than expected. Therefore, it was found that the use of SSG breakwater in Anzali port located on the southern shores of the Caspian Sea is not economically viable.

1.Introduction

The world has always needed more energy resources as it progresses. Humankind has tried to use knowledge to reduce these destructive effects, as exemplified by renewable energy use. Energies such as wind energy, solar energy, marine energy, etc., are examples of these efforts. Unlike fossil fuels, these energies are much less polluting and more stable than they are. In all societies, sustainable energy sources are essential because sustainable development will cover these sustainable sources.

One group of renewable energies that is less studied than other energies is marine energy. Oceans, seas, lakes, rivers, etc., are considered as sources of this energy. Among the types of energies related to marine energy, we can mention the energy of sea currents, wave energy, geothermal energy, tidal energy, salinity gradient energy, etc.

In this study, the use of SSG breakwater has been investigated. This breakwater has different types such as three-tank, two-tank, and single-tank models. These models have also been studied on different slopes. In this research, the three-tank model has been used.

This study aims to evaluate the feasibility of using SSG breakwater in the Bandar Anzali region on the southern shores of the Caspian Sea. In the first part, the general situation of the Caspian Sea is explained. The second part deals with building a model for the desired simulation and the explanations around it. In the third section, the results obtained from each simulation step are discussed. Also, sections four and five deal with the discussion and conclusions about the issues raised.

In 2005, j.kofoed experimentally tested a three-tank model of the SSG breakwater installed on an island in Norway[1]. Larsen and Kofoed investigated surface loads caused by waves in the SSG breakwater, exposed to high waves[2]. In a study, Kofoed et al. Examined the wave conditions at the SSG breakwater prototype's installation site in the Kuwaiti region of

Norway. The MildSim computer model was also used in this study to obtain a realistic combination of wave conditions[3]

In 2006, Kofoed et al. Investigated dynamic wave loading on the SSG breakwater, which observed two types of behavior. Behavior on the sloping front plates was accompanied by a surge and an action on the vertical rear walls in the upper tank associated with a weak water jet[4]

Jensen et al. Presented a report in 2006 for the SSG breakwater, which was a series of overflows in tanks and power generated by turbines. This report aimed to enable the user to optimize the geometry and program of the turbine. Simulate, and in fact, this report was like a manual guide to generating power from the SSG breakwater[5]. In another study, Beseau investigated the application of computational fluid dynamics (CFD) to wave loading in SSG breakwaters, and the CFX10 method was used to generate strong waves[6]. In a 2007 study, Margheritini investigated the general forces acting on an SSG converter structure in 3D. The results were presented in terms of maximum forces in three different directions and application points related to the system[7]. In an article, Borgorino and Kofoed reported on the steps in setting up an SSG converter at a Lisle site[8]. Margheritini et al. Wrote an article in 2009 describing the status and performance of the SSG breakwater. Finally, three tanks were provided for it. Besides, the front panels have an angle of 35 degrees[9]. In a 2014 study, Alamian et al. Examined different converters to find suitable converters for the Caspian Sea[10]. Oliviera et al. Investigated the effect of wave focuses walls on an SSG converter's performance. These members concentrate the energy of the random waves and thus increase the overtopping phenomenon[11]

Mariano Buccino et al. in their research Used computational fluid dynamics (CFD) in SSG converters in 17 experiments[12]. In another study in 2017, Musa et al. Validated numerical models against physical experiments[13]. Yazid Maliki et al. Examined the possibility of using CFDs for large-scale wave converter (WEC) simulations. This study aimed to validate the use of CFD simulation[14]. Salimi et al. Examined the possibility of using this breakwater in the Oman Sea and the Persian Gulf[15]. In another 2019 study, Rodriguez Delgado et al. Examined the effects of rising sea levels on a wave farm's performance to protect the coast from shoreline erosion, in which they explored several scenarios[16]. Di Lauro et al. in 2020 analyzed a model of an overpass breakwater called the OBREC-V that examined hydraulic efficiency and response stability against hydraulic loads[17]. In a study, Hernandez-Fontes et al. Examined social, economic, and environmental factors surrounding ocean energy use in areas without electricity[18] Gonçalves et al .in 2020, using 30-year hindcast and previous studies in the Canary Islands to study the wave climate for more ccurate wave energy information to get a more comprehensive view of the energy sources of the waves[19]. Ribal et al. in a research explored the high potential of wave energy off the coast of Indonesia[20]. In 2020, Alizadeh et al. Examined the spatiotemporal variability of wave power in the Persian Gulf by the end of the 21st century[21]. Jahangir et al. Also investigated an energy/wind turbine/wave converter system in the Iranian seas[22].

1. Caspian sea

With 371,000 square kilometers, the Caspian Sea is located between southeastern Europe and Asia at latitudes of 47.13 and 36.34 latitude and 46.43 and 54.51 longitude. Countries around the Caspian Sea include Russia, Azerbaijan, Iran, Turkmenistan, and Kazakhstan. In terms of climate, the Caspian Sea generally has a windy environment that provides ideal wave energy potential.

In terms of depth, the Caspian Sea rises from north to south. Also, the average depth of the northern part is less than 10 meters, and the middle part varies from 180 to 788 meters, and for the southern part of the sea, the depth varies between 960 to 1025 meters.

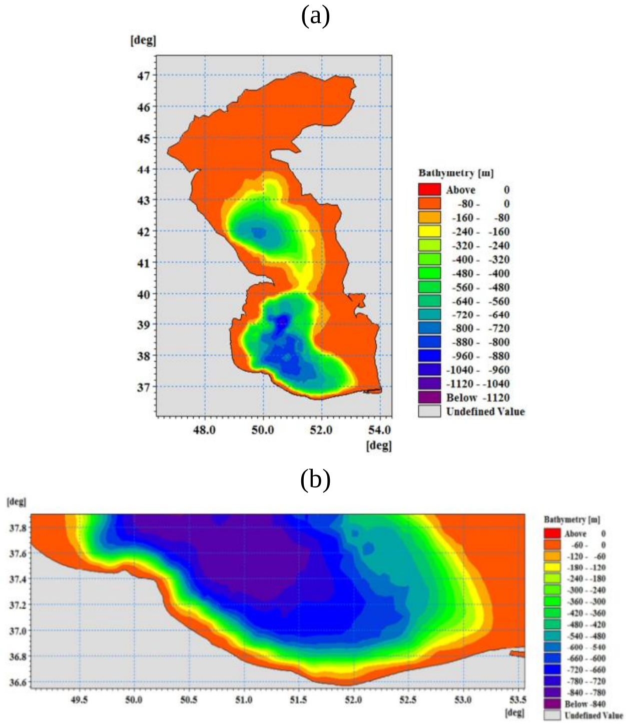
(a)

(b)

Figure 1. (a) Depth variation in the Caspian Sea.

(b) Magnified view of the variety of depths in the Caspian

Sea[23] According to researches on wave power in the Caspian Sea in different seasons, it has been found that the wave power is low in spring, which increases slightly in summer. Also, this amount reaches its maximum in autumn and winter. The maximum wave power in autumn is 3.5 kW / m in autumn, and the minimum wave power is 1.5 kW / m in spring[23].

(a)

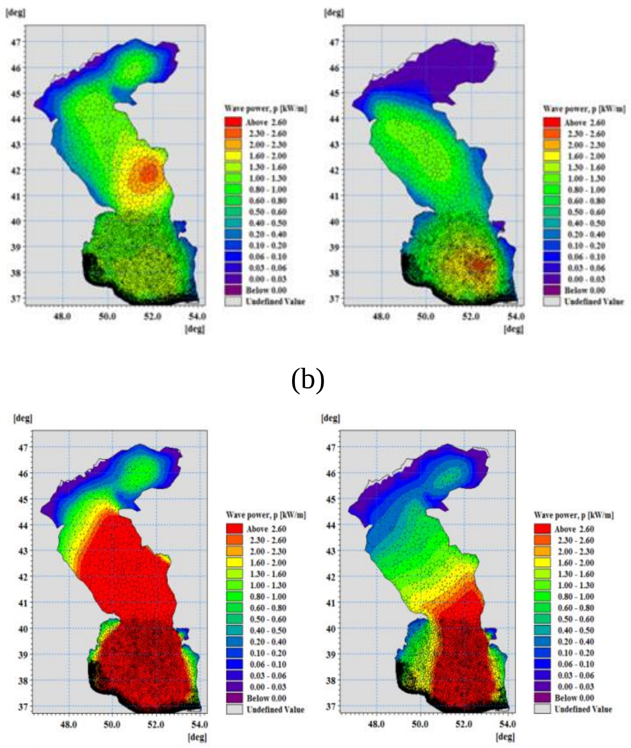

Figure 2. (a) Wave power in the Caspian Sea in spring (left) and summer (right)

Regarding the wind characteristics in the Caspian Sea, in the southern part of the sea, the number of days with storms (wind speed more than 15 m/s) does not exceed 20 to 30 per year. On the other hand, in the northern parts of the Caspian Sea and the eastern parts of its central section, between 30 and 40 storms are observed annually.

About 10 to 12 percent of the northwest and southeast winds have a speed of about 5 to 9 m/s (moderate wind), which increases somewhat in summer. On the other hand, strong winds at speeds of more than 10 m/s are not more than 4 to 6 percent. But winds of more than 25 m/s are rare and do not exceed a few per year. The average annual wind speed over the entire Caspian Sea is 5.7 m/s. The highest average wind speed of 6 to 7 m/s is observed in the Caspian Sea's central part. On the entire east coast, the average annual wind speed is approximately 5 to 6 m/s, and the maximum is observed on the Mangishlak Peninsula. In the southern Caspian Sea, where strong winds are rare, the average annual wind speed is 4.4 m/s [24].

2. Materials and methods

The model is based on research conducted at the University of Aalborg by j. Kofoed, who has done most of the research on the device[1]. The initial model was made according to the study's dimensions and on a laboratory scale in Solidworks software and transferred to ANSYS workbench software.

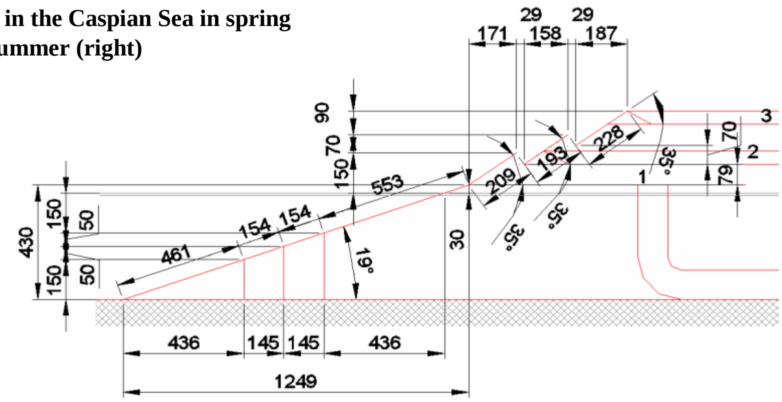

Figure 3. Dimentions provided by j.kofoed[1]


(a)
(b)

Figure 4. (a), (b) Model made in solidworks software based on research laboratory sizes

But on the other hand, according to Margheriniti's research on this breakwater, one of the things Margheriniti considered when using this breakwater was the issue of water height in front of the structure because things like sediment problems can reduce the efficiency of the system. According to research, the water's height should be at least 15 meters to avoid sediment issues when using this breakwater[9]. On the other hand, this model is designed for a water height of about 6 meters. According to the changes made, this breakwater is about 60 meters long, about 20 meters high, and about 9 meters wide, according to the figure below, without any changes in principal dimensions.

Figure 5. The model is in real size after applying changes to the top in solidworks software

Since the built model is not suitable for simulation and appears as a surface in the ANSYS SpaceClaim, some changes are made in this space on the built model.

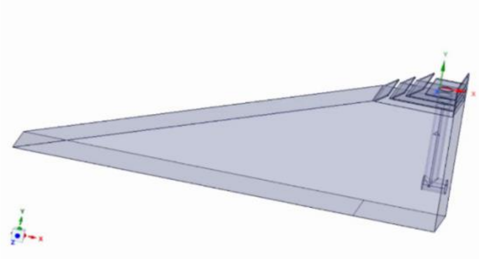

Figure 6. Model after modifications

Finally, the designated sections for water were created in the simulation to prepare the model for data entry.

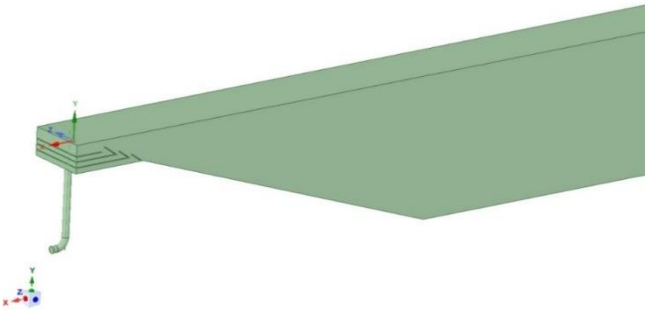

Figure 7. The final model of break water

In the ANSYS meshing, to start in the physics preference section, select the CFD option, and then in the solver preference section, the fluent solver type was placed. Also, the kind of policy used in this study is the Cutcell mesh.

In the next step, naming on different sections and by doing so, various inputs and their types, walls, outputs, etc., were determined.

This study had two types of inputs, Water and air inlet. This model also had two outputs, one of them is the path output installed, and the other is the output of the air part in this model. Another thing was to specify the part where the fluids are in contact with each other, and finally, the other parts were called walls.

With the naming done and each section's name specified, the mesh was inserted for each section with the appropriate size, in such a way that the parts had smaller meshes than the other parts because of their greater importance.

In the model made by creating a body sizing in the mesh settings, the part related to the mix section, a combination of two phases of climate, was applied with more delicate elements in the range of 0.08 meters. Also, for the air part, like the mix part, another body sizing was created, and a mesh with a 0.5-meter element was applied to it, and the other parts have a mesh element with a size of 1 meter.

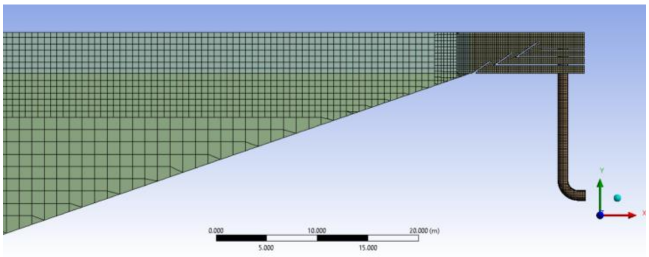

Figure 8. Overview of the created mesh for model

In the ANSYS fluent, the model was imported, and the desired data such as wave specifications and simulation conditions were defined for it. To speed up the simulation, the model was imported in two dimensions in fluent.

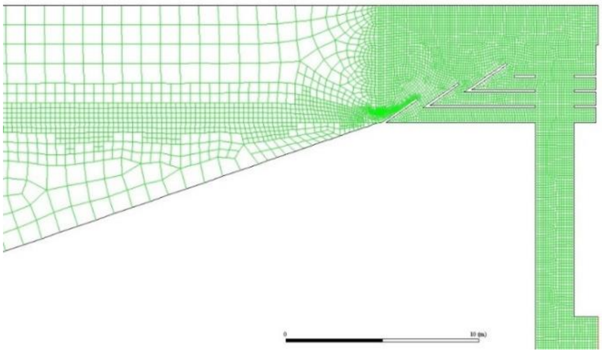

Figure 9. 2D view imported in ANSYS fluent

In this simulation, data from one of the articles related to the South Caspian Sea coasts study have been used. The elevations obtained from the report are 0.06, 0.5, and 2.825, respectively, and the periodicities obtained are 1.7, 4.2, and 8.3, respectively[25]. The following table provides information on possible scenarios for simulation in Anzali port using that information:

Table1. information about waves for simulation

Wave speed (C)m/s	Wavelength (L)m	Wave period (Ts) s	Wave height (Hs)m	Count possible situations
2.6	4.5	1.7	0.06	(1
2.6	4.5	1.7	0.5	(2
6.56	27.55	4.2	0.06	(3
6.56	27.55	4.2	0.5	(4
6.56	27.55	4.2	2.825	(5
13.02	107.6	8.3	0.06	(6
13.02	107.6	8.3	0.5	(7
13.02	107.6	8.3	2.825	(8

In this study, the vote of a more detailed study of waves, each simulation was performed as a single wave to study each wave's effects on the breakwater more accurately.

The average wave power (W/m) of the SSG wave-energy extraction device can be computed based on the height and period of the wave as:

$$P_{wave=\rho g^2 H_S^2 T_e/64\pi} \qquad (1)$$

where *r* is the water density; *g* is gravity acceleration; *Hs* is the significant wave height, and the energy period *Te* is estimated—here simply set to be Tp/1.15 (Tp: wave peak period). Also, the average potential water overpasses power (W/m) can be computed as:

$$P_{Hyd} = \sum_{j=1}^{n=3} \rho g q_{ov,j} R_{C,J} \qquad (2)$$

Where $q_{ov;j}$ is the average volume of incoming water per width in the tank number *j*, and $R_{c;j}$ is the crest height of the wave in the tank number *j*, and N_{Res} is the total number of tanks in the SSG breakwater.[3] To calculate $q_{ov;j}$, the following equation has been used.:

$$q_{ov,j} = \int_{R_{c,j}}^{R_{c,j+1}} \frac{dq}{dz} dz = \left(\Pi_j \lambda_j\right) \times \sqrt{g \times H_S^3} \times \frac{A}{B} \times e^{C\frac{R_{C,1}}{H_{m_0,t}}} \times \left[e^{B\times\frac{R_{C,j+1}}{H_{m0,t}}} - e^{B\times\frac{R_{C,j}}{H_{m0,t}}}\right] \qquad (3)$$

Parameters *A*, *B*, and *C* in equation (8) are experimental coefficients for a standard design. The geometrical difference between a new design and the standard one can be expressed as the correction coefficient (k_j).

Referring to the previous researches, these empirical coefficients (*A*, *B*, and *C*) can be considered as follows

$$\begin{cases} A = \ \ 0.197 \\ B = -1.753 \\ C = -0.408 \end{cases} \qquad (4)$$

According to experimental tests, the best $R_{c;j}$ for the reservoir crest height from the sea water level obtained were $R_{c,1} = 1.5$ m , $R_{c,2} = 2.5$ m and $R_{c,3} = 4.5$ m

It should be mentioned that λ_j is also a combination of three different coefficients including discharge coefficient (λ_{dr}), area coefficient ($\lambda_{\alpha r}$), and crest coefficient (λ_s).

$$\lambda_{dr} = 1 - k\frac{Sinh\left(2K_p h\times\left(1-\frac{d_r}{h}\right)\right)+\left(2K_p h\right)\times\left(1-\frac{d_r}{h}\right)}{Sinh\left(2K_p h\right)+\left(2K_p h\right)} \qquad (5)$$

In the above-mentioned equation, *k* is a control coefficient for the incoming wave into the submerged area of the breakwater. It is usually considered to be 0.4. d_r in equation (5) is the distance between average sea level and the lower edge of the lowest breakwater's ramp, and K_p is the maximum wave number of the wave with the maximum wavelength (L_p).

As mentioned, $\lambda_{\alpha r}$ can be derived using equation (6) :

$$\lambda_{\alpha r} = \cos^3(\alpha_r - 30) \qquad (6)$$

where α_r is the angle of ramp under mean sea level and its optimal value was considered to be 30°. This value simplifies equation (6) as $\lambda_{\alpha r} = 1$.λ_s coefficient can be obtained using following equation:

$$\lambda_s = \begin{cases} 0.4\, sin\left(\frac{2\pi}{3}R\right) + 0.6 & For\ R < 0.75 \\ 1 & For\ R \geq 0.75 \end{cases} \qquad (7)$$

In which $R = R_c / H_s$

The whole mass of water which enters to the SSG breakwater can be calculated from the below experimental formulas

$$\frac{\sum_{j=1}^{N} q_{ov,j}}{\lambda_{\alpha r}\lambda_{dr}\lambda_s\sqrt{gH_{m0,t}^2}} = 0.2 \times e^{-2.6\times\frac{R_{c,j}}{H_{m0,t}}} \qquad (8)$$

or

$$Q = \frac{q}{\lambda_{\alpha r}\lambda_{dr}\lambda_s\sqrt{gH_s^3}} = 0.2 \times e^{-2.6\times\frac{R_C \quad 1}{H_s\gamma_b\gamma_h\gamma_\beta}} \qquad (9)$$

referring to the literatures $\gamma_r = \gamma_b = \gamma_h = \gamma_\beta = 1$.

Koefoed presented a formula as follows

$$\frac{q}{\lambda_{\alpha r}\lambda_{dr}\lambda_s\sqrt{gH_S^3}} = 0.2 \times e^{-2.6\times\frac{R_{c,j}}{H_s}} \qquad (10)$$

And the efficiency is calculated from the following equation[15]

$$\eta_{Hyd}^{SS} = {P_{Hyd}}\big/{P_{wave}} \qquad (11)$$

3. Results

3.1. Wave No. 1

This wave has a height of 0.06 meters and a period of 1.7 seconds. Over time, the peak velocity in the contour decreases, and as the wave recedes, the wave velocity gradually decreases. The speed is gradually reduced at the beginning of the path, and the speed is increased at the output channel. Also, over time, the speed at the output path decreases, and its value decreases. This reduction is also observed along the channel path.

As time goes on and the wave recedes, the volume of available water decreases, and the peak point of the wave occurs before 15 seconds; and the first and second reservoirs are emptied, and the third reservoir is emptied. In general, in this wave, due to the smaller volume of water, most of the lower reservoirs are involved, and the upper reservoirs, especially the first reservoir, do not pass a large volume of fluid.

As shown in the diagram, the end of the diagram is when the fluid enters the outlet path, which is naturally accompanied by an increase in velocity and energy. In the first graph of fluid velocity, we see that the fluid has a constant velocity for most of the simulation time. When it enters the output channel, it reaches its maximum velocity of about 12 m / s for a moment.

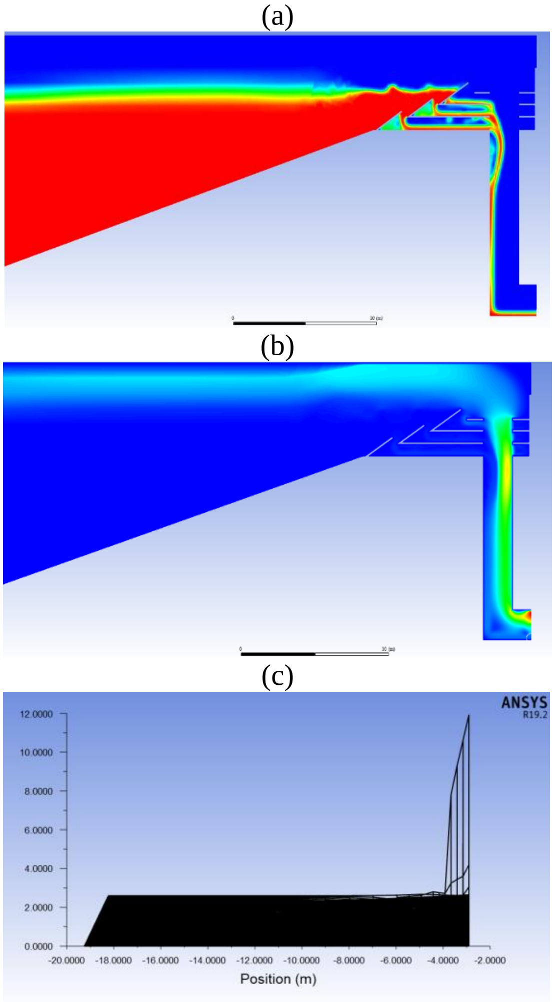

Figure 10. (a) The volume of water for wave No. 1. (b) Velocity situation in wave No. 1,(c) Velocity chart for wave No. 1

This mode has an average speed of 2.2 m/s, wave power of 0.00293 kW/m, and hydraulic efficiency of 0.099 kW/m.

3.2. Wave No. 2

This wave has a height of 0.06 meters and a period of 4.2 seconds. Over time, we see a gradual decrease in the speed of the output path. However, this reduction is more noticeable along the output path and is not detectable in the channel's end parts due to involvement until the last moment.

Because the first and second waves have the same velocity of 2.6 m/s, they are almost equal in terms of inlet water volume and shapes and differ only in some details.

According to the information in the diagram of the water flow velocity, it can be seen that in a wave with these conditions, the maximum velocity can reach about 16 meters per second. Still, in other cases, the fluid velocity is a constant value.

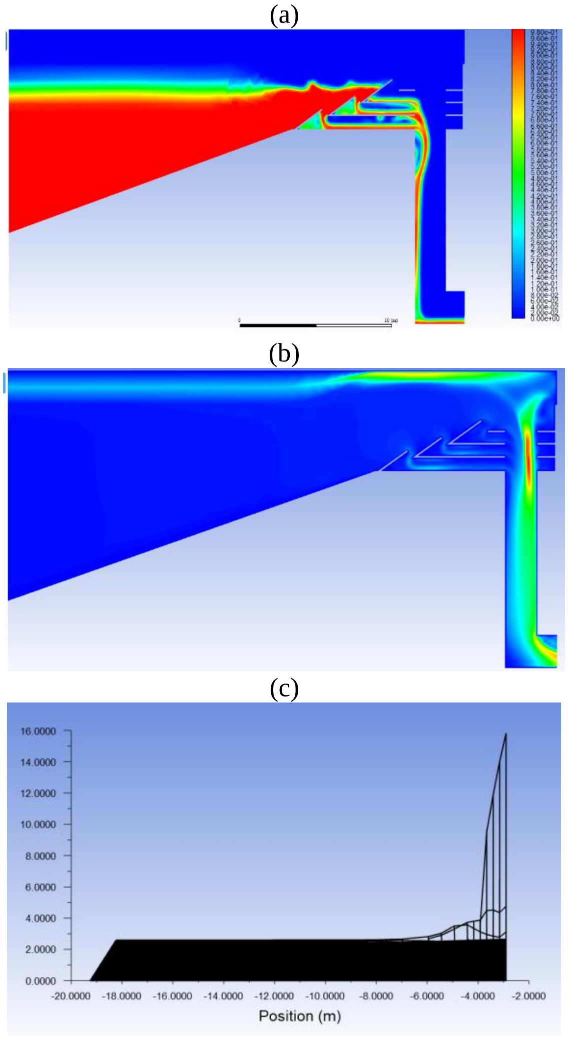

Figure 11. (a) the volume of water for wave No. 2. (b) velocity situation in wave No. 2. (c) velocity chart for wave No. 2

This mode has an average speed of 2.15 m/s, wave power of 0.20352 kW/m, and hydraulic efficiency of 0.06326 kW/m.

3.3. Wave No. 3

The increase in velocity is visible from the air and water phases. Also, to a limited extent, an increase in water inlet speed can be seen in the lower reservoir. Due to the increase in velocity and the increase in water volume, more time is needed to drain the water, which makes the descent of the deceleration, in this case, have less night. On the other hand, due to the higher speed in the third wave, we see a noticeable increase in speed at the output of the three reservoirs and the wall of the output channel. However, over time, this speed is transmitted to the output channel relative to 8 seconds. On the other hand, due to the increase in water volume, we are witnessing changes in the reservoirs' inlet velocities.

As shown in the figure, due to the increase in velocity, the water volume has increased and completed more of the breaking capacity, but not completely. On the other hand, it can be seen that the volume of water in the canal is gradually draining from 8 to 15 seconds. Furthermore, when the channel empties of fluid, a slight instability is observed over the simulation time**.**

As can be seen in the flow velocity diagram, the main velocity is related to the same velocity of 6.52 m/s, which reaches its maximum value of about 8 to 9 m/s when entering the output channel.

(a)

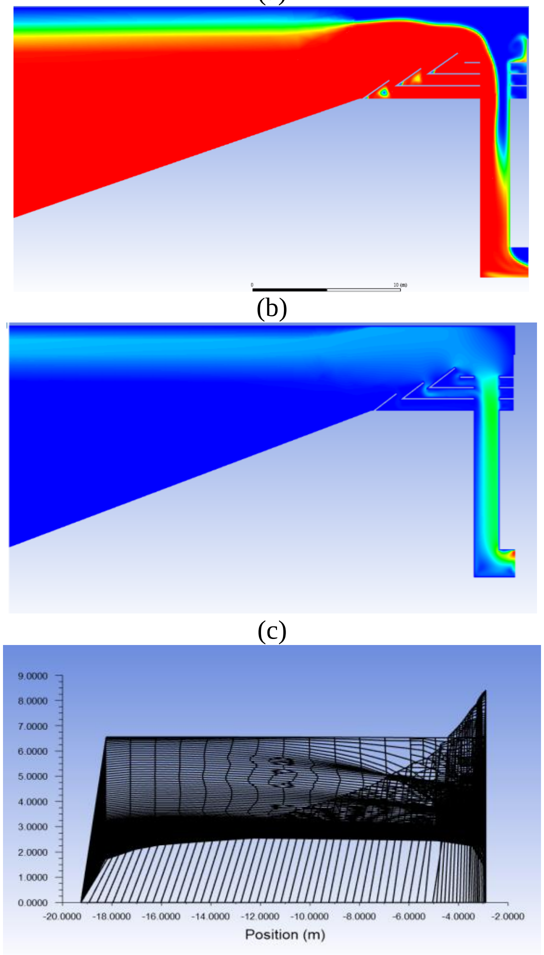

(b)

(c)

Figure 12. (a) the volume of water for wave No. 3. (b) velocity situation in wave No. 3. (c) velocity chart for wave No. 3

This mode has an average speed of 2.7 m/s, wave power of 0.00724 kW/m, and hydraulic efficiency of 0.097062 kW/m.

3.4. Wave No. 4

In the relevant image of 8 seconds, we see the speed spread throughout the channel wall. But moving to higher seconds of the simulation, we see a decrease in water's speed entering the reservoirs. We also see velocity pressure at the inlet point of the reservoirs to the outlet channel. Due to the similarity of velocity to the third wave, the velocity contour is similar to the third wave contour. As in the output of the reservoirs and the channel wall, we see a high number of velocities, which are reduced by continuing the simulation process. And is broadcast throughout the channel.

At second 8, a slightly larger water volume enters the channel than at second 8 of the third wave. But in the 15th second, as the wave recedes, we see a decrease in the water in this breakwater output path.

In the flow velocity diagram, similar to the third wave, most of the simulations have a constant velocity at the beginning of the simulation, which is 6.25 m/s, reaching its maximum value of about 8 m/s by entering the reservoirs and the output channel.

(a)

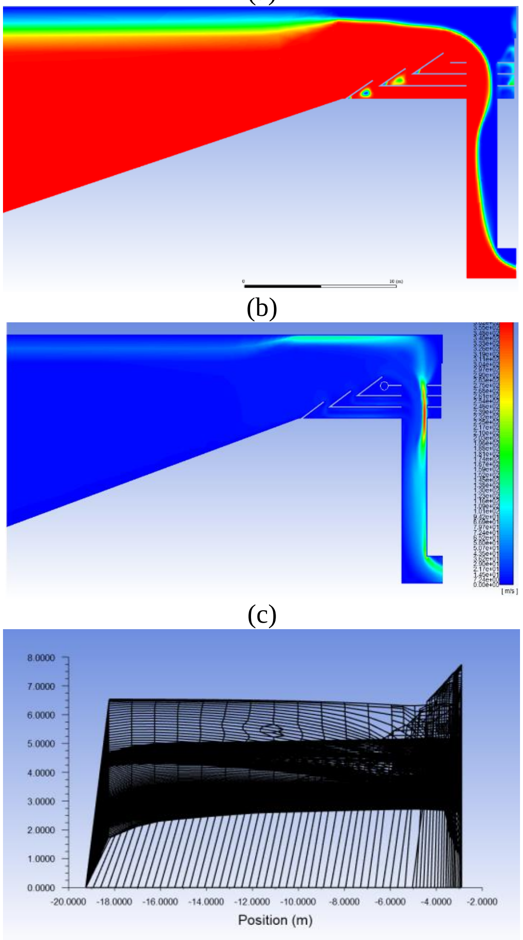

(b)

(c)

Figure 13. (a) The volume of water for wave No. 4. (b) Velocity situation in wave No. 4.(c). Velocity chart for wave No. 4

This mode has an average speed of 2.72 m/s, wave power of 0.50282 kW/m, and hydraulic efficiency of 0.07296 kW/m.

3.5. Wave No. 5

In this case, unlike other cases, there is no regular entry and exit of water fluid, and turbulence at the inlet is well known, especially in the 8th second. We cause part of the water to pass from the breakwater to the space behind the water. Also, this turbulence on different parts of this breakwater, such as the speed of water entering the reservoirs, is significant. But by going through this step to higher seconds, the simulation is balanced, and the input speed of the reservoirs is almost the same as the previous two modes. On the other hand, the velocity turbulence in the output channel, which we saw in 8 seconds, has reached a normal equilibrium in this second. Most of the velocity is visible in certain areas, such as the output of the reservoirs. It should be noted that, unlike the previous two waves, which had points with an accumulation of velocity in the 8th second, in this wave, this state occurred later, and in the 15th second, we see this issue.

In the flow volume contour, the amount of turbulence created and the water volume that the breakwater has passed can be seen, which is 15th seconds; as the water flow reaches equilibrium and the wave recedes, the volume of water in the breakwater gradually decreases. As in the previous waves, the regression and stability of the fluid flow can be seen.

In the flow velocity diagram, the simulation starts with the input number of 6.25 m/s, mostly stable. Only at the beginning of the reservoirs in which we saw turbulence, we see some increase. Finally, we see water entering the canal, which is a maximum of about. It reaches 12 m/s.

(a)

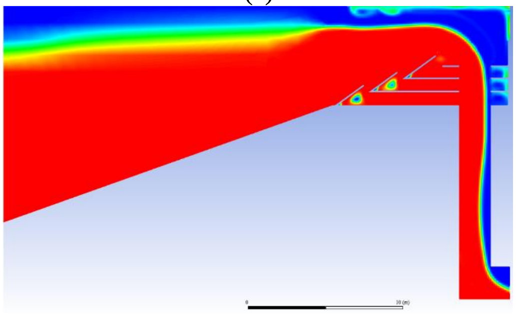

(b)

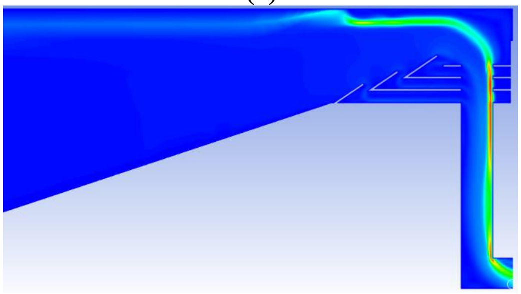

(c)

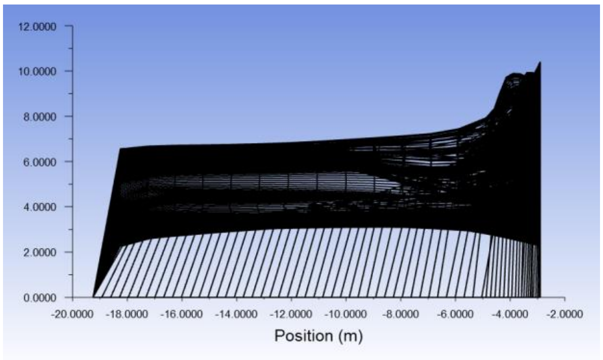

Figure 14. (a) The volume of water for wave No. 5. (b) Velocity situation in wave No. 5. (c) Velocity chart for wave No. 5

This mode has an average speed of 2.81 m/s, wave power of 16.05164 kW/m, and hydraulic efficiency of 0.58104 kW/m

3.6. Wave No. 6

Due to the high speed of the wave, we see the arrival of a large volume of water and, in fact, the use of all the capacity of the breakwater, which leads to an increase in the overall speed in various parameters of the breakwater. This wave has a higher speed in the simulation stages than the previous waves, which causes the speed to have large values along the output channel. Also, input speed values have been increased. Over time, we see an increase in speed in the outlet channel, which due to the large volume of water, it is natural that it takes longer. Of course, the highest speed can be seen on the sides of the channel and the channel output.

Due to the high velocity of the wave and the arrival of a large water flow volume, it was clear that all paths were full. Naturally, due to this amount of fluid volume, even with the wave retreating, it takes longer than in other cases for the fluid to flow from the outlet. Be evacuated. Due to the high volume of water, more time is needed for the wave to retreat. Although. At 15 seconds, there are signs of a wave reversal.

In the velocity diagram, during the simulation, it has an almost constant velocity equal to the incoming velocity of 13.02 m/s. Gradually, however, as the simulation progresses, this value increases to a maximum of about 30 m/s.

(a)

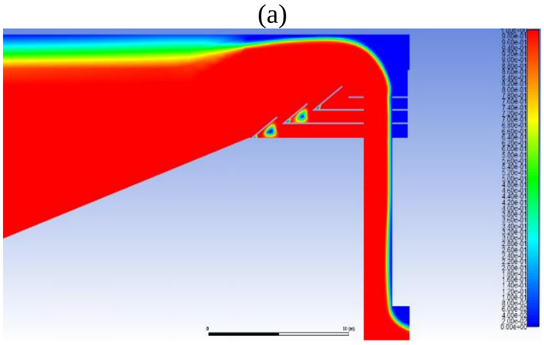

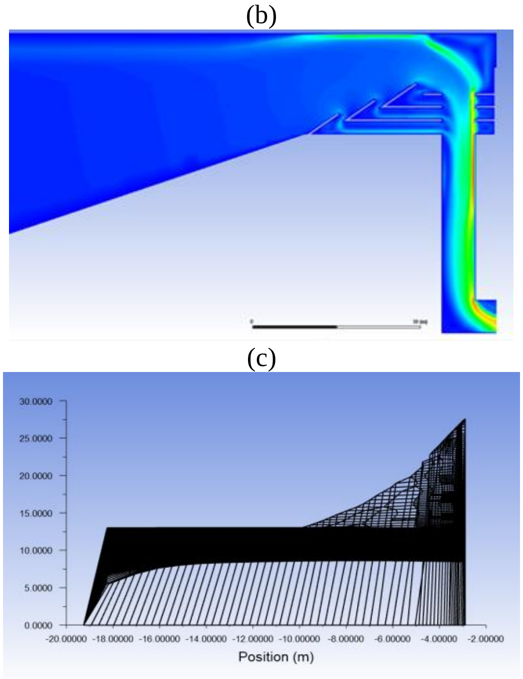

Figure 15. (a) The volume of water for wave No. 6. (b) Velocity situation in wave No. 6. (c) Velocity chart for wave No. 6

This mode has an average speed of 6.1 m/s, wave power of 0.01430 kW/m, and hydraulic efficiency of 0.01773 kW/m

3.7. Wave No. 7

Similar to the sixth case, due to the same speed, in this case, too, a large volume of water fills the outlet path, and no significant change is seen in the figure, such as turbulence. Similar to the previous cases, at the point of exit of water fluid into the outlet channel, we see the highest velocity as a point that is a combination of air and water velocity. Also, in 15 seconds, we see a faster scatter than in 8. Due to the velocity similar to the sixth wave, the velocity contour of the seventh wave is identical to the sixth wave, and we see the maximum velocity at the side of the channel as well as at the output in 8 seconds, which increases throughout the channel as the simulation time.

According to the previous explanation, which is also evident here, a large volume of water flow almost fills the outlet path's capacity. It requires more time than other cases to empty this volume of water fluid. Also, we see the gradual balancing of the input wave and the beginning of its regression.

According to the diagram, the speed, in this case, has reached about 30 m/s; although similar to the previous wave, most of the simulation time has remained constant, but in the end, has increased.

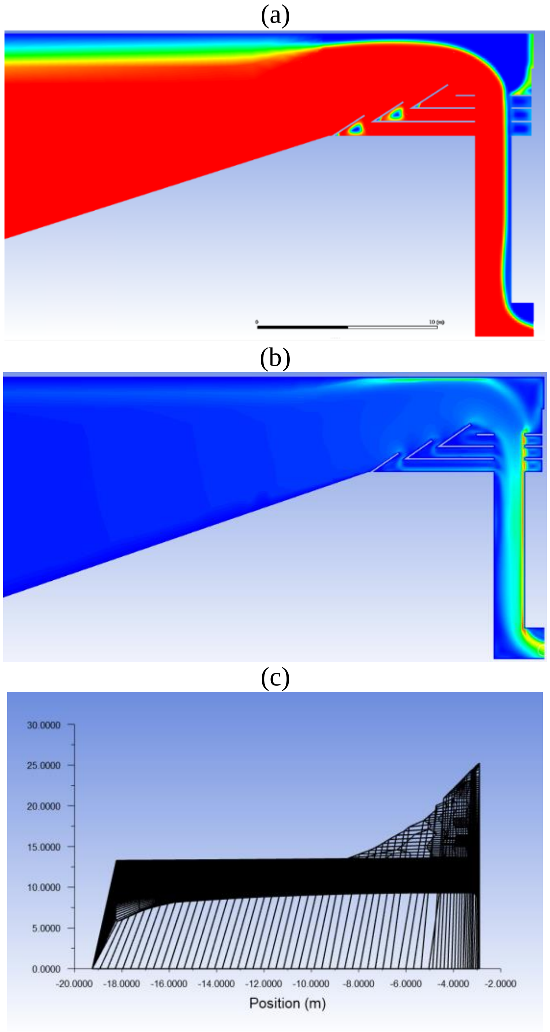

Figure 16. (a) The volume of water for wave No. 7. (b) Velocity situation in wave No. 7. (c) Velocity chart for wave No. 7

This mode has an average speed of 6.3 m/s, wave power of 0.99367 kW/m, and hydraulic efficiency of 0.6136 kW/m

3.8. Wave No. 8

Due to its speed equal to the previous two modes, it has a similar distribution. As the simulation process continues, this speed begins to reach equilibrium, and its scattering decreases. On the other hand, the speed of water entering the reservoirs is also reduced. As a result, instead of the speed distribution in the channel being uniform, we see an increase in this value at the side of the channel and the outlet of the reservoirs, which continues to the outlet of the channel.

As in the previous two cases, at a speed of 13.02 m/s, the volume of flowing water fills the entire path. Also, according to this mode's information, the eighth mode has the highest intensity among other modes. However, as the simulation process continues, water volume gradually decreases, as shown in the 15th second image.

In the diagram of fluid flow velocity, most simulation time has a constant input time of 13.02 m / s. But with the arrival of the reservoirs and the entry of fluid flow into the outlet channel, this value has increased and reached it maximun valie.

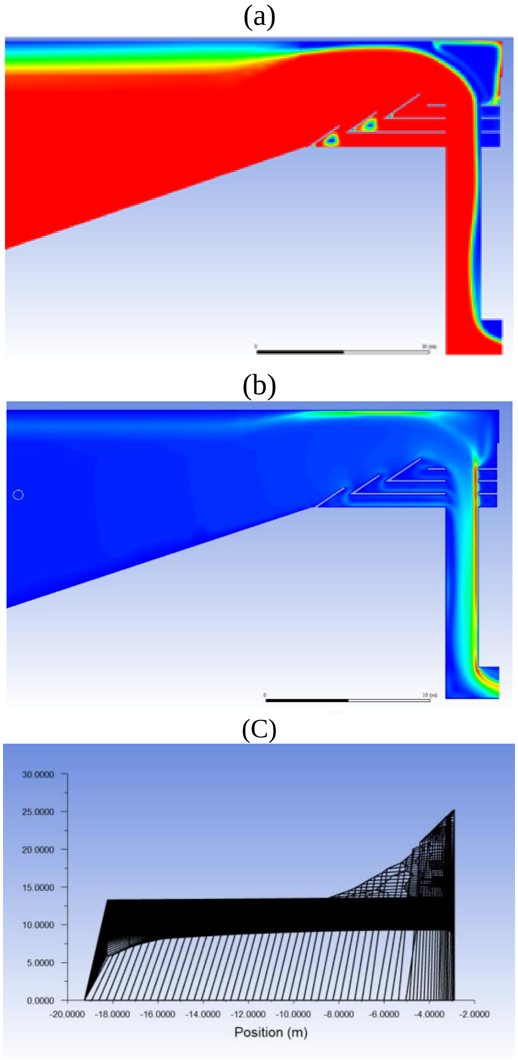

Figure 17. (a) The volume of water for wave No. 8. (b) Velocity situation in wave No. 8. (c) Velocity chart for wave No. 8

This mode has an average speed of 6.71 m/s, wave power of 31.72074 kW/m, and hydraulic efficiency of 0.86550 kW/mc

3.9. Validation

To confirm the method's accuracy to obtain the numbers used in this study, validation was performed based on valid research. In this work, based on the dissertation done in this direction in the country's southern seas[26], a criterion was set in which the study is both modelings using FLOW 3D software for different waves and examining laboratory behaviour and comparison of the respective breaker. Accordingly, a wave with a periodicity of 1.84 seconds and a wave index height of 0.069 m was considered, simulated in ANSYS fluent software, and the corresponding numbers were obtained. Also, by equating the number obtained in FLOW 3D software for the same conditions, the software number for the average speed obtained in ANSYS fluent software is 2.26 m/s, and the desired number for FLOW 3D software is 1.90 m/s,which is a difference of 18.9%. Show that it is a relatively acceptable error.

Table 2. Information of validation

H_S (m)	0.069
T_P (s)	1.84
V_M (Flow3D)	1.90
V_M (Ansys)	2.26
Error	%18.9

4. Discussion

According to the information in this table, it is clear that this breakwater's efficiency is a deficient number and is out of the economic range for most waves with a height of less than one meter.

Also, for waves with a height of more than one meter and a period of more than 4.2 seconds, good efficiency can be observed. In general, the highest efficiency expected from this system in the Caspian Sea is the eighth wave with a height of 2.825 meters and a period of 8.3 seconds, which has an efficiency of about 86%.

The following diagrams show the changes in wave height and the changes in the waves' periodicity over about three months in 2019, prepared by the Ports and Shipping Authority.

Table 3. shows an overview of the results obtained from the simulation of the eight selected waves

Type of Spectrum	**1**	**2**	**3**	**4**	**5**	**6**	**7**	**8**
Tp (s)	1.7	1.7	4.2	4.2	4.2	8.3	8.3	8.3
Hs (m)	0.06	0.5	0.06	0.5	2.825	0.06	0.5	2.825
V_{mean} (m/s)	2.2	2.15	2.70	2.72	2.81	6.10	6.30	6.71
P_{wave} (kW/m)	0.00293	0.20352	0.00724	0.50282	16.05146	0.01430	0.99367	31.72074
P_{Hyd} (kW/m)	0.00029	0.01287	0.00070	0.03668	9.32654	0.00025	0.60971	27.45430
η^{ss}_{Hyd}	0.099	0.063	0.097	0.072	0.581	0.017	0.613	0.825

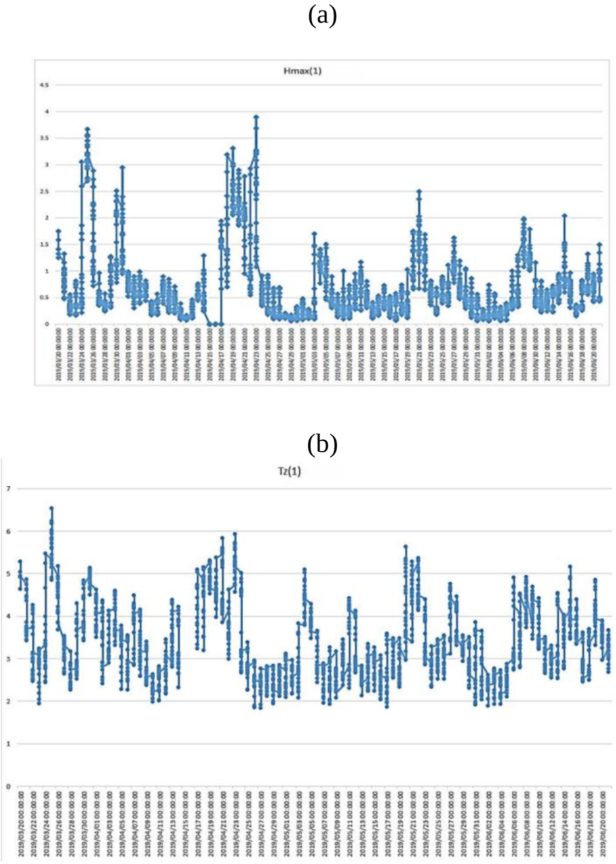
(a)

(b)

Figure 18. (a) Graph of wave height occurring in 100 days (b) Graph of wave period occurring in 100 days

According to the information obtained from these diagrams, it is clear that the principal height of the waves in the Caspian Sea is about 0.5 meters and less. Also, the periodicity is about 3 to 4 seconds.

But among the three waves that are most efficient than the others, in this period, we see only the fifth wave and the seventh and eighth waves did not occur, and their occurrence in the Caspian Sea is unlikely.

5. Conclusion

In this study, the possibility of using SSG breakwaters on the southern shores of the Caspian Sea and, more precisely, the Bandar Anzali region was investigated. First, the Caspian Sea's general characteristics, such as the characteristics of waves and wind currents in the sea, were examined. Then, according to previous research in this field, its model was built in ANSYS software. Also, simulations were performed in ANSYS fluent. Based on the available information, eight waves were selected, and for each wave in specific factors such as total pressure, velocity, current volume, and other cases were examined.

Regarding the possibility of using this breakwater, considering that most of the waves in the time shown are close to the simulated wave No. 4, and given that waves with a height of less than 1 meter of sufficient efficiency are not available, Therefore, it is recommended to use this system in smaller dimensions, which are more economically viable.

Author Contributions:

Hereby, it is confirmed that all the authors contributed in the manuscript.

References

[1] Kofoed, J.P., *Model testing of the wave energy converter Seawave Slot-Cone Generator.* Hydraulics and Coastal Engineering, 2005(18).

[2] Larsen, B.J. and J.P. Kofoed, *Model Test Setup and Program for Experimental Estimation of Surface Loads of the SSG Kvitsøy Pilot Plant from Extreme Wave Conditions.* Hydraulics and Coastal Engineering, 2005(32).

[3] Margheritini, L., J.P. Kofoed, and P. Frigaard, *Status and performance of the SSG Wave Energy Converter*. Department of Civil Engineering, Aalborg University, Denmark, 2006.

[4] Kofoed, J.P., D. Vicinanza, and E. Osaland. *Estimation of design wave loads on the SSG WEC pilot plant based on 3-D model tests*. in *The Sixteenth International Offshore and Polar Engineering Conference*. 2006. International Society of Offshore and Polar Engineers.

[5] Jensen, P.M., L. Gilling, and J.P. Kofoed, *User manual for SSG power simulation 2.* 2006.

[6] Beseau, M., *Analysis o f Computational Fluid Dynamics study on Seawave Slot-Cone Generator.* 2006.

[7] Margheritini, L. and A. Morris, *Model tests on overall forces on the SSG pilot plant.* 2007.

[8] Borgarino, B. and J.P. Kofoed, *Power Production from Integration of SSG in a Breakwater at Liseleje.* 2007.

[9] Margheritini, L., D. Vicinanza, and P. Frigaard, *SSG wave energy converter: Design, reliability and hydraulic performance of an innovative overtopping device.* Renewable Energy, 2009. 34(5): p. 1371-1380.

[10] Alamian, R., et al., *Evaluation of technologies for harvesting wave energy in Caspian Sea.* Renewable and Sustainable Energy Reviews, 2014. 32: p. 468-476.

[11] Oliveira, P., et al., *Experimental evaluation of the effect of wave focusing walls on the performance of the Sea-wave Slot-cone Generator.* Energy Conversion and Management, 2016. 110: p. 165-175.

[12] Buccino, M., et al., *The use of CFD in the analysis of wave loadings acting on seawave slot-cone generators.* Sustainability, 2016. 8(12): p. 1255.

[13] Musa, M.A., et al., *Numerical simulation of wave flow over the overtopping breakwater for energy conversion (OBREC) device.* Procedia engineering, 2017. 194: p. 166-173.

[14] Maliki, A.Y., et al., *Comparison of numerical and experimental results for overtopping discharge of*

the OBREC wave energy converter. J. Eng. Sci. Technol, 2017. 12(5): p. 1337-1353.

[15] Salimi, F., M. Rahbani, and B. Mohammadi, *Feasibility assessment for installing Sea-wave Slot-cone Generator breakwater in the Iranian coasts of Persian Gulf and Oman Sea*. Energy & Environment, 2018. 29(1): p. 95-108.

[16] Rodriguez-Delgado, C., R.J. Bergillos, and G. Iglesias, *Dual wave farms for energy production and coastal protection under sea level rise*. Journal of Cleaner Production, 2019. 222: p. 364-372.

[17] Di Lauro, E., et al., *Advantages of an innovative vertical breakwater with an overtopping wave energy converter*. Coastal Engineering, 2020: p. 103713.

[18] Hernández-Fontes, J.V., et al., *Is ocean energy an alternative in developing regions? A case study in Michoacan, Mexico*. Journal of Cleaner Production, 2020. 266: p. 121984.

[19] Gonçalves, M., P. Martinho, and C.G. Soares, *Wave energy assessment based on a 33-year hindcast for the Canary Islands*. Renewable Energy, 2020. 152: p. 259-269.

[20] Ribal, A., et al., *A high-resolution wave energy resource assessment of Indonesia*. Renewable Energy, 2020. 160: p. 1349-1363.

[21] Alizadeh, M.J., et al., *Projection of spatiotemporal variability of wave power in the Persian Gulf by the end of 21st century: GCM and CORDEX ensemble*. Journal of Cleaner Production, 2020. 256: p. 120400.

[22] Jahangir, M.H., A. Shahsavari, and M.A.V. Rad, *Feasibility study of a zero emission PV/Wind turbine/Wave energy converter hybrid system for stand-alone power supply: A case study*. Journal of Cleaner Production, 2020. 262: p. 121250.

[23] Jahangir, M.H. and M. Mazinani, *Evaluation of the convertible offshore wave energy capacity of the southern strip of the Caspian Sea*. Renewable Energy, 2020. 152: p. 331-346.

[24] Kosarev, A.N., *Physico-geographical conditions of the Caspian Sea*, in *The Caspian Sea Environment*. 2005, Springer. p. 5-31.

[25] Alamian, R., et al., *Wave energy potential along the southern coast of the Caspian Sea*. International journal of marine energy, 2017. 19: p. 221-234.

[26] Khalifehei, K., G. Azizyan, and C. Gualtieri, *Analyzing the Performance of Wave-Energy Generator Systems (SSG) for the Southern Coasts of Iran, in the Persian Gulf and Oman Sea*. Energies, 2018. 11(11): p. 3209.

INTERNATIONAL JOURNAL OF
COASTAL & OFFSHORE ENGINEERING

IJCOE Vol.6/No. 5/ Autumn 2021 (76-88) / **Special issue of "Marine Renewable Energy"**

Available online at: www. Ijcoe.org

Evaluation and validation of wind energy extension (Bahooz) in Manjil region

Akbar Rashidi Ebrahim Hasari [1*], Milad Rhime[2]

[*1] *Assistant Professor, Department of Marine Physics, Faculty of Natural Resources and Marine Sciences, Tarbiat Modares University, Iran; akbar.rashidi@modares.ac.ir*
[2] *M.Sc. in Environmental Science, Department of Environmental Science, Faculty of Natural Resources and Marine Sciences, Tarbiat Modares University, Iran; miladrhime@yahoo.com*

ARTICLE INFO

Article History:
Received: 02 May. 2021
Accepted: 25 Oct. 2021

Keywords:
wind energy
Power Density
Harvest Energy
Sites Suitable
Rough's impact
Wind Simulations
Artificial intelligence
Manjil Wind park

ABSTRACT

Development that is not environmentally friendly is not sustainable. One of the methods of sustainable development is the use of renewable energy such as wind. One of the most important sites in Iran with wind energy potential is the Manjil region. Four sites in Manjil region (Manjil, Siahpoosh, Rudbar and Herzeville) were surveyed. In this paper, wind energy potential measurement in onshore and coastal areas evaluates wind energy according to the extensions developed by the authors. The results with scientific achievements and similar software in 4 stages of wind simulation, simulation of conditions the boundary of the range will assess wind power and extractable energy. Summary of spatial fit and arrangement of turbines shows that Manjil power plant in world energy class has sufficient quality of energy production and can be compared with global sites. This site with a nominal capacity of 240 million kilowatt-hours per year is one of the largest sites in the Middle East with a capacity factor of 0.25. Siahpoosh site with a capacity of 410 million kilowatt-hours per year has a limited factor capacity of 8%. This site has a coefficient of variation of 11%, which modeling shows that the choice of 660 MW turbines is not very appropriate and practical. Therefore, it seems that the use of 500 kW turbines has a better capability than 660 turbines on this site. Based on the results, the two sites of Rudbar and Herzeville have a very proportionate factor capacity, so these two sites can be upgraded according to the installation of Class 4 and 3 turbines.

1. Introduction

Energy is one of the most important factors in the progress and development of human societies [1]. On the one hand, population growth and the limitation of fossil resources, and the increase in environmental pollution caused by the burning of these resources, on the other hand, have led to the development of exploration for clean and non-polluting sources [2]. The wind is one of these clean, inexhaustible sources of free energy [3]. Wind energy, like other renewable energy sources, is geographically extensive and at the same time scattered and decentralized, and almost always available [4]. This energy was used as an energy source before the Industrial Revolution, to the extent necessary, but during the Industrial Revolution, the use of fossil fuels replaced wind energy due to its cheapness and high reliability [5]. During this period, the old wind turbines could not compete with the oil and gas energy market, but again in 1973 and 1978, due to two major oil shocks and the concept of sustainable development, the energy economy of oil and gas was hit hard and In this way, the cost of energy generated by wind turbines improved compared to the global rate of energy prices [6, 7]. Since 1975, significant progress has been made in the field of wind turbines to generate electricity [8]. In 1980, the first wind turbine connected to the national grid was built [9]. Since then, numerous research centers and institutes, and laboratories around the world have studied new technologies for the use of wind energy [10]. In addition, this crisis caused new tendencies in the field of the application of wind energy technology to generate electricity connected to the grid, pumping water, and supplying electricity to different areas [11].

Global installed wind-generation capacity onshore and offshore has increased by a factor of almost 75 in the past two decades, jumping from 7.5 gigawatts (GW) in

1997 to some 730 GW by 2020, according to IRENA[1]'s latest data. Production of wind electricity doubled between 2009 and 2013, and in 2016 wind energy accounted for 16% of the electricity generated by renewables [12]. Many parts of the world have strong wind speeds, but the best locations for generating wind power are sometimes remote ones. Offshore wind power offers tremendous potential [13]. The worlds Winds total about 2,700 terawatts of energy. About 25% of it is located 100 meters above the ground [14]. However, unfortunately in Iran, the use of wind energy is not widely developed and it is used in limited places such as Manjil and Binalood. The capacity of 95 MW has reached 303 MW, which is all related to the offshore sector [13].

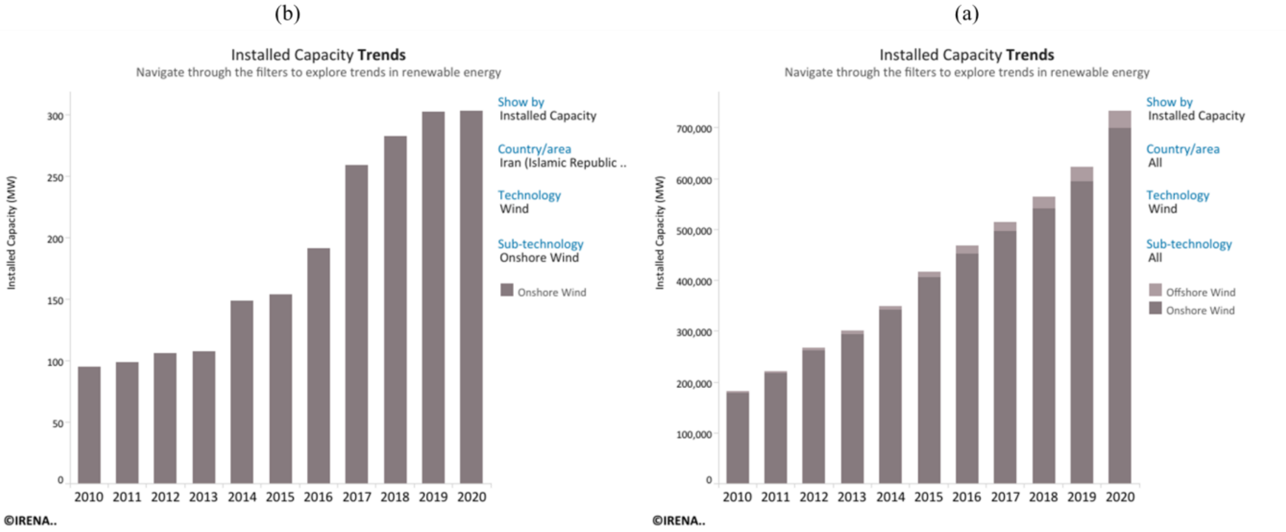
(b)

(a)

Figure 1. installed wind-generation capacity onshore and offshore in World&Iran;
(a): World, (b): Iran

Renewable energy will account for a significant share of the world economy, the share of renewable energy in the world energy portfolio doubling by 2030, the world's gross domestic product will increase by 0.6% or $ 706 billion [15] According to this study, oil-dependent economies have the highest financial loss [16] and among Asian countries, Japan will have the highest GDP [13]. In 2019, 11 and a half million jobs were created by renewable energy in the world, of which the share of wind energy is 1.17 million people [15]. In this statistic, Iran's share is 468 thousand jobs in all energy and 3400 jobs in wind energy [15].

Modeling and validation of models that represent possible wind energy functions are critical [17]. Wind speed has a random nature that in order to model it, it is necessary to select the appropriate cumulative distribution function [18]. In this regard, many studies and researches have been done, which can be referred to as the probability distribution functions of Weibull, Riley, and normal distribution. In studies [18-22], emphasis and support have been on the Weibull model. But some of the other Persian and Latin studies are as follows: they have studied the daily, monthly and annual trends of wind speeds in an area for energy and have considered winds with a speed of 4 to 25 meters per second to be suitable for energy. In energy density measurement, they used Weibull and Rayleigh distribution functions [23]. Wind energy potential in 21 US states was calculated using Weibull distribution and the amount of wind energy extracted was estimated for the whole country. [24] Especially marine resources were used more efficiently [25]. In Iranian studies, Mostafaeipour et al [26], Hashemi et al [27], Kayhani et al [28], and Ashrafi et al. [29] used a similar method to estimate Weibull distribution parameters using They used a frequency distribution table. Also in the study area, we can mention [30] that have calculated the wind energy potential. But in this study, in addition to evaluating the wind energy situation in the study area, provide an extension is provided to calculate this importance and validate it with the help of conventional methods.

2. Materials and methods:

2.1. Area of study

The study area in the present study is limited to the border of Rudbar city, which is located at latitude and longitude 37 degrees north and 50 degrees west. This city is located in the middle of Alborz Mountains, a continuous valley towards Qazvin plain by the Caspian Sea. The average temperature of this city is 24 degrees

---

[1] International Renewable Energy Agency (IRENA)

Celsius and it can be seen in different parts of it from desert climate to dense forest. It is important to note that there are several wind sites in this city and the ability to generate wind energy due to climatic conditions and topography has a high speed with an average of 5.5 meters per second. In the recent study, 4 sites of Manjil, Qazvin, Harzivel and Rudbar in black are studied and evaluated (fig.2).

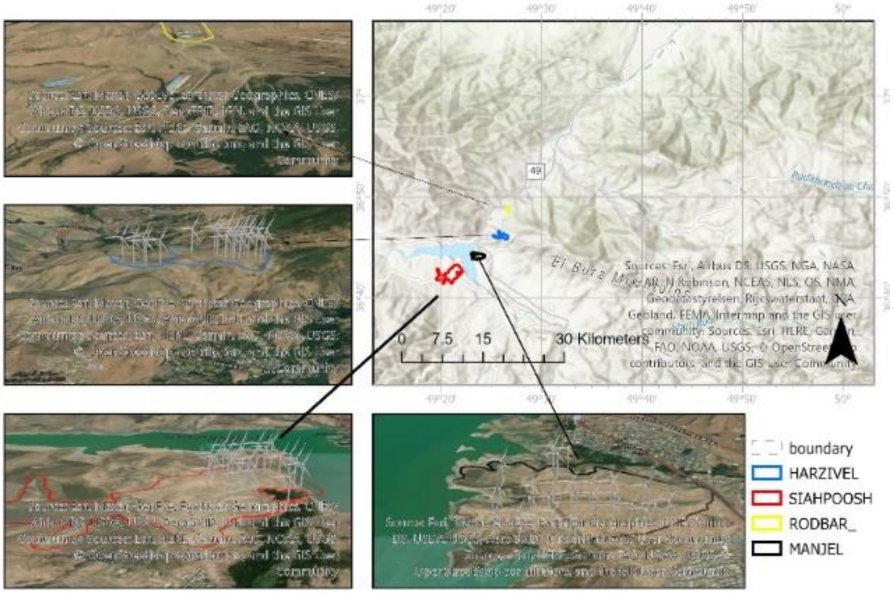

Figure 2. Study area

Our study in the field of wind energy potential measurement in onshore and coastal areas evaluates wind energy according to the extensions developed by the authors and the results with scientific achievements and similar software in 4 stages of wind simulation, simulation of conditions the boundary of the range will assess wind power and extractable energy.

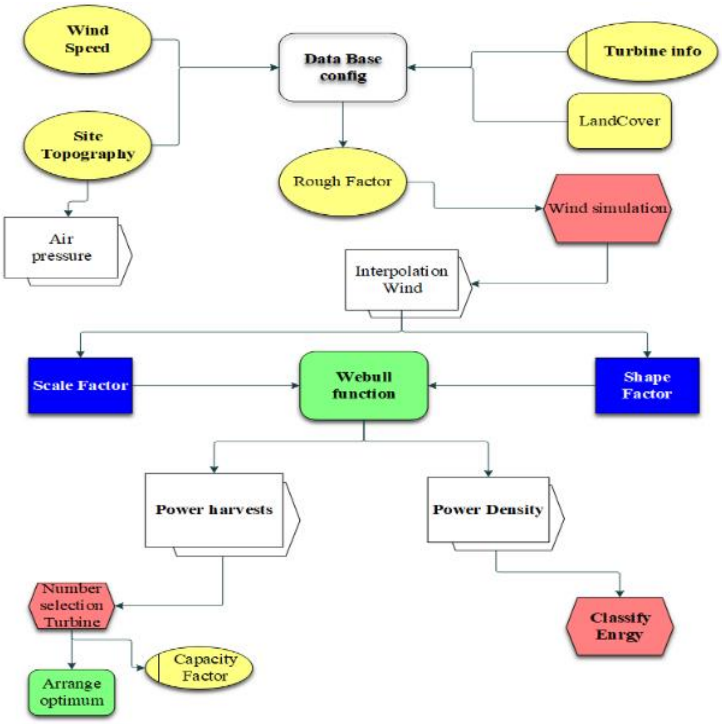

Figure 3. Flow diagram of wind energy software

2.2. Modeling wind data from reference height to turbine rotor height

All meteorological data are collected at a height of 10 meters, so modeling wind speed at the height of the turbine rotor is important. There are two numerical or rule models for wind speed modeling; Which is suitable for smooth surfaces and homogeneous distribution of wind[31]. The first is the logarithmic law, which is derived from the fluid mechanism of boundary layers studied on the basis of theoretical and experimental sciences. The second approach is derived from research into wind energy science, called the law of power. Both models have unknown variables. In the present study, the power law profile has been used. This rule is presented in a simplified form based on Equation (1).

$$\frac{V}{V_R}=(\frac{Z}{Z_R})^{\alpha} \qquad (1)$$

2.3. Wind scattering probability modeling

Usually, various statistical functions such as Weibull and Rayleigh functions are used to model wind energy[31]; Many studies have been done to evaluate the accuracy of these models, which in general, the Weibull function has a more accurate response to the facts; But in general, it can be understood that the accuracy of these statistical functions depends on the type and accuracy of the study of their parameters[23]. To verify these methods, many studies have been done that almost all studies in the field of wind energy, the use of standard deviation methods for studies for which there is no information is appropriate. In the continuation, the most likely neighborhood method can be used[32]. After calculating the wind speed, the probability of wind in a period can be calculated with statistical functions. In the study of wind energy, the Weibull function has the most application and has a good accuracy[33]. This function is a special discussion of the third-class distribution of the Pearson function, which was presented by Weibull in 1937[34]. This function has two functions for wind speed: 1- Probability density function 2- Cumulative distribution function. These functions are indicators of time changes for wind speed. Thus Equation (2) represents the Weibull probability density function:

$$f\ (v)=\frac{\kappa}{\lambda}\left(\frac{v}{\lambda}\right)^{\kappa-1} e^{-\left(\frac{v}{\lambda}\right)^{\kappa}} \qquad (2)$$

In Equation (2), respectively, they represent the shape and scale factors, which is a dimensionless numerical shape factor, which in a way represents the wind speed variability. It is lower, on the other hand, the scale factor is expressed in m / s-1. In fact, this factor indicates the concentration of wind speed in a certain range. The small size of the scale factor helps to increase the probability of wind speed. In other words, changes in this factor affect the scale value of the base curvature of the distribution [31]e is equal to the Napier number. And v, f (v) indicates wind speed and wind speed probability, respectively.

In short, it can be said that the Weibull function is affected by the accuracy of two factors, shape and scale. If the shape factor is decreasing, the changes around the average wind speed are also reduced. For example, if the scale factor is constant and the shape factor is less than 2.6, right skewing occurs, while in contrast, negative skewing occurs above 3.6. If this value is between 2.6 to 3.6, the elongation coefficient is zero. Now, on the opposite side, the scale factor is minimal, indicating the concentration of wind speed in a certain value, for example, if the shape factor and the scale factor increase, the graph is stretched to the right. Pulls to the left and increases the height of the chart. To further understand this, we can look at Figure 4.

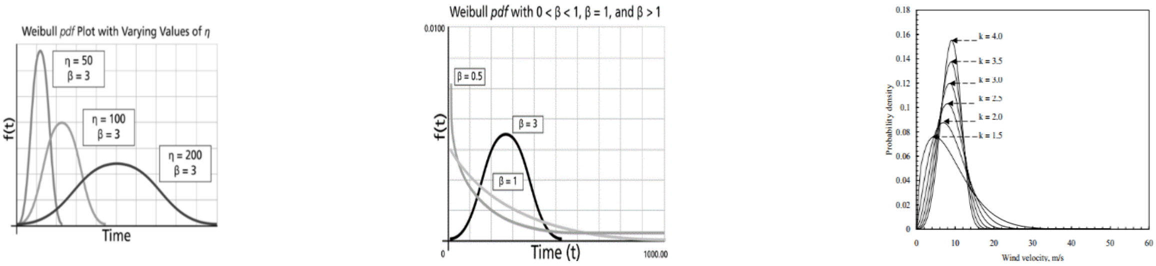

C B A

Figure 4. A: shows the frequency of shape and scale factors and their effect on the probability function, B: the effect of the shape factor on the probability curve, C: the effect of the Mughal factor on the probability

There are different methods for calculating the two factors of shape and scale. But two methods are commonly used: 1- Standard deviation 2- The most probable neighborhood are the most used. It should be noted that the first method is most useful for identifying wind sources from which little field information is available [35]but the second method is the most accurate in calculating energy and increasing the accuracy of power plant output calculations among a variety of methods[25]. The method of calculating these methods is presented in the equations below, respectively.

$$\lambda = \frac{v_m}{\Gamma\left(1 + \frac{1}{\kappa}\right)} \qquad (3)$$

$$\lambda = \frac{v_m \times \kappa^{2.6674}}{0.184 + 0.816 \times \kappa^{2.73855}} \qquad (4)$$

$$\kappa = \left(\frac{\sigma_v}{v_m}\right)^{-1.090} \qquad (5)$$

Equation (3) represents the scale factor. In this equation, г represents the gamma function. Numerous studies have used Equation (4) to increase the accuracy of calculations. Equation (5) also shows the method of calculating the shape factor from the standard deviation and the average wind speed [36].

2.4. Power density

Dominant energy assessment on a site is an essential component of wind energy projects. In fact, the density of energy concentration is to measure the energy per unit area of the rotor and time. Energy concentration density the site design method and turbine blades are very effective. To investigate the amount of energy per unit area and its suitability for the construction of wind farm sites can be rewritten from Equation (5) and easily used [37].

$$PD = \frac{1}{2}\rho \sum_{j=1}^{n} (f\ (v_j).\mathrm{v}_j{}^3) \qquad (5)$$

In Equation (5), PD represents the density of a concentration in a given area in terms of (watts per square meter). ρ also indicates the density of air. $F\ (v_j)$ and v_j indicate the probability of wind gusts at a given speed and wind speed, respectively.

The air boundary layer is one of the most important components in various calculations. This component is directly affected by the earth's surface[38]. But other physical parameters such as acceleration, temperature, humidity change rapidly per unit time and place. In wind energy engineering, identifying the variance of vertical wind speed plays a very important role in designs[39]. 1- Directly on turbine energy production at the characteristic height of the tower 2- Significant effect on the lifespan of turbine blades. Air density is an important factor in the boundary layer under the influence of temperature and pressure. Equation (6), which is the ideal gas law, can be used to calculate air density.

$$\rho = \frac{p}{RT} = 3.4837\frac{p}{T} \qquad (6)$$

In Equation (6) p shows the air pressure. T stands for air temperature in Kelvin. Therefore, air density is calculated in kilograms per cubic meter.

The International Atmospheric Standard assumes sea level temperature and air pressure to be 288.15 Kelvin and 101.325 kpa, so the air density is 1.225 kg / m2 [40]. Therefore, with increasing altitude, the air density decreases. To calculate the air density less than 500 meters, Equation (7) presented by the organization [40] can be used.

$$\rho = 1.225 - (1.194 \times 10^{-4})\,\mathrm{z} \qquad (7)$$

In Equation (7) z represents the height of the turbine to calculate the wind speed.

Extractable energy

There is no question that not all energy in the environment can be used. Rather, our energy extraction will be limited to the environmental conditions and capabilities of existing technology. Therefore, the extraction of energy from the total energy will be in a certain range and range of wind speed and time. Because energy exchangers have a significant effect on energy that can be extracted from the environment. Therefore, we can simply refer to Equation (8) with which the extractable energy of the turbine can be extracted experimentally [41].

$$P_{avail} = \frac{1}{2}\rho A v^3 C_p \qquad (8)$$

Equation (8) shows the extractable energy and A represents the surface area of the sweeper. In the continuation of the same equation, C_p expresses the specific characteristics of the turbine, which depend on the number of impellers per unit time and its diameter.

According to all the topics mentioned in the extraction discussion, the elimination of ancillary parameters and increasing the focus on general parameters causes a greater degree of confidence in the extraction of energy calculations. Since the wind blows in a unit of time and continuously, so the calculation of the speed of extractable energy must also be done in this range. Therefore, the use of equation (9) for modeling extractable energy is more applicable [41].

$$p(v)=\begin{cases}0 & V<V_c \;\; or \;\; V>V_f\\ \Pr & V_r<V<V_f\\ \left(V^m-V_c^m\right)/\left(V_r^m-V_c^m\right) & V_c\le V\le V_r\end{cases} \qquad (9)$$

$$HE=nday\times\frac{p}{p_0}\times P_{rate}\times\left(\int_{V_c}^{V_r}\frac{V-V_c}{V_r-V_c}\right)\times f(V)dV+\int_{V_r}^{V_0}f(V)dV\times(1-loss)$$

According to Equation (9) HE is equal to the energy recoverable for one year, Nday is equal to the consideration, usually 365 days. Prate is equal to the maximum power of the turbine used, and f (v) is the probability of wind speed. v_c and v_o are the assumed wind speed and the assumed speed for maximum output and the wind speed required to start the turbine and finally the assumed speed for stopping the turbine to prevent damage, respectively. In this regard, the loss value will be used for the reduction coefficient of the turbine.

3. Results and Discussion:

One of the important pieces of information in wind energy modeling is related to the dominant land cover[42].This causes the local flow in different parts with fluctuations in height and speed or by creating a dam to cause different rotations in wind speed and direction. In the study area from the north, focusing on the Rudbar valley, there is more forest cover at high altitudes. Forest cover accounts for 27% of the area. But in the southern part, due to its location in the opposite direction of the Caspian Sea, it is less under the influence of prevailing air currents, which has caused 68% of the area to be dense rangeland cover with an average height of 65 cm and of course poor cover shrublands. In the area in question, 0.80 of the total area is water levels and 0.31 of the total area is urban areas. According to the roughness map extracted from the land cover section, there is the least friction in the southern part of the region. Only two urban settlements with the lowest area in the region have the highest coefficient.

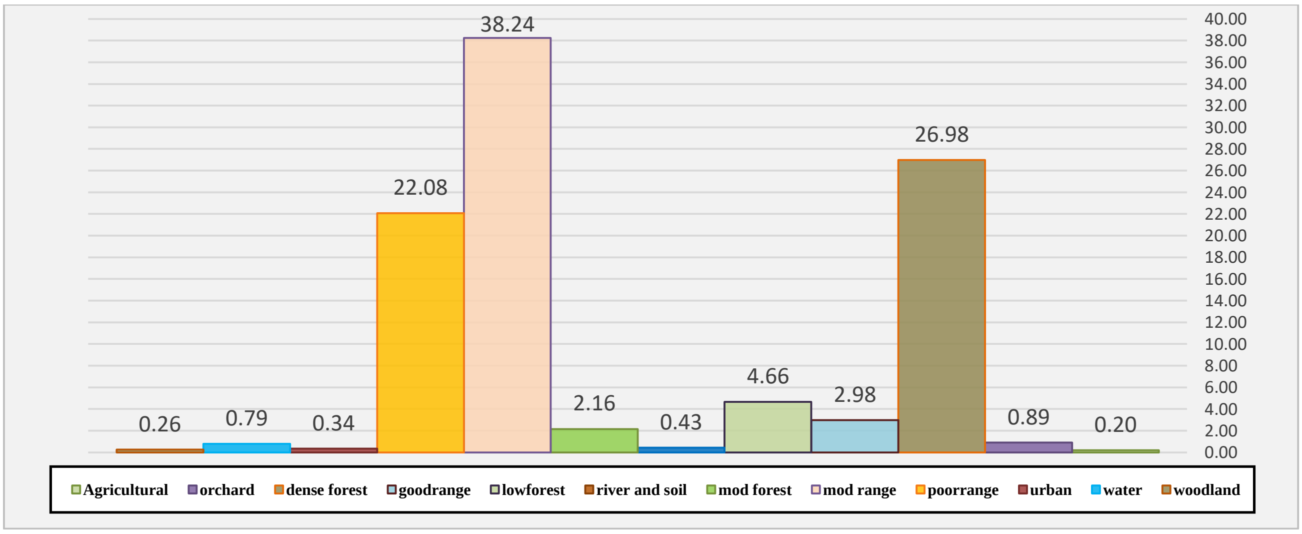

Figure 5. Percentage chart of land cover frequency

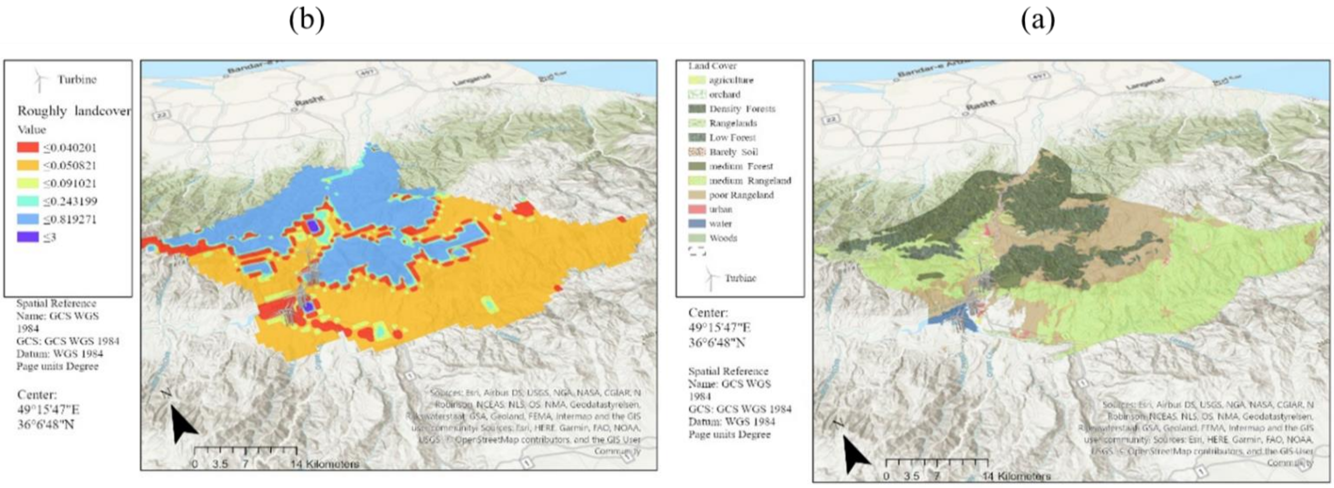

Figure 6. Status maps; (a): Land cover, (b): Ambient roughness coefficient

An important parameter of the output of the atmospheric pressure simulation model in the region with emphasis on the existing experimental model. In this model, altitude and topographic shape play a major role in creating local wind flow. The existence of the Rudbar River and the existing valley causes airflow from the Qazvin desert to the Caspian Sea and vice versa. In the study area, the elevation difference of 250 meters from the riverbed to 3000 meters of Alborz peaks is very important and effective in twisting and creating a strong local mountain stream. One of the important features of the region according to the output model is the atmospheric pressure parameter. In the Manjil-Rudbar valley area, the level of pressure or air density according to the air density map is equal to 1.21 Pa; which is significant pressure for the area and in terms of functionality at the coastal level. On the slopes of the existing valley, the density decreases by 1.1. The average density of 0.92 in the whole region limits the development for the construction of wind farms. In the study of 4 sites in the study area, the Herzeville site with the highest height on the southern slope (1000 meters) and the Rudbar site with a height of 1125 meters have the lowest power density level and this factor reduces the efficiency of turbine systems in higher production capacity.

(b) (a)

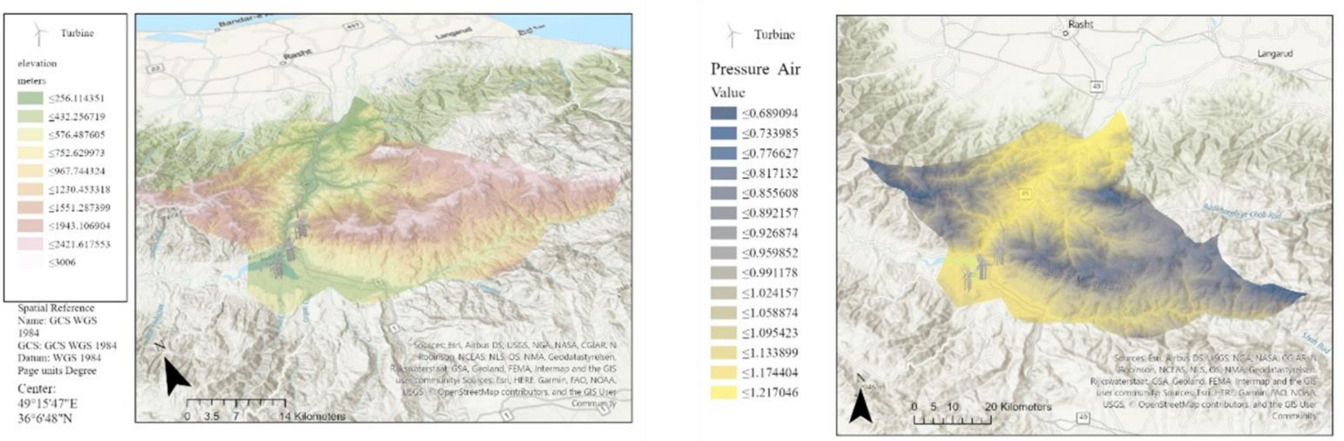

Figure 7. Status maps; (a): Elevation , (b): air pressure

According to the model output of the average and the deviation of the average wind speed at the level of 10 and 40 meters, the effect of the ambient roughness parameter in the speed disorder shows itself more. In our study, the Jirandeh region has the highest speed and standard deviation due to the low time of the statistical period. But in other areas, the trend is normal. According to our study, the average of 11 to 9 meters per second is excellent and causes the turbines to operate at their maximum power. The mean deviation at the level of study sites shows that the Manjil site is in the most optimal point with the highest speed and the lowest standard deviation (9.54 and 1.4), respectively.

(b) (a)

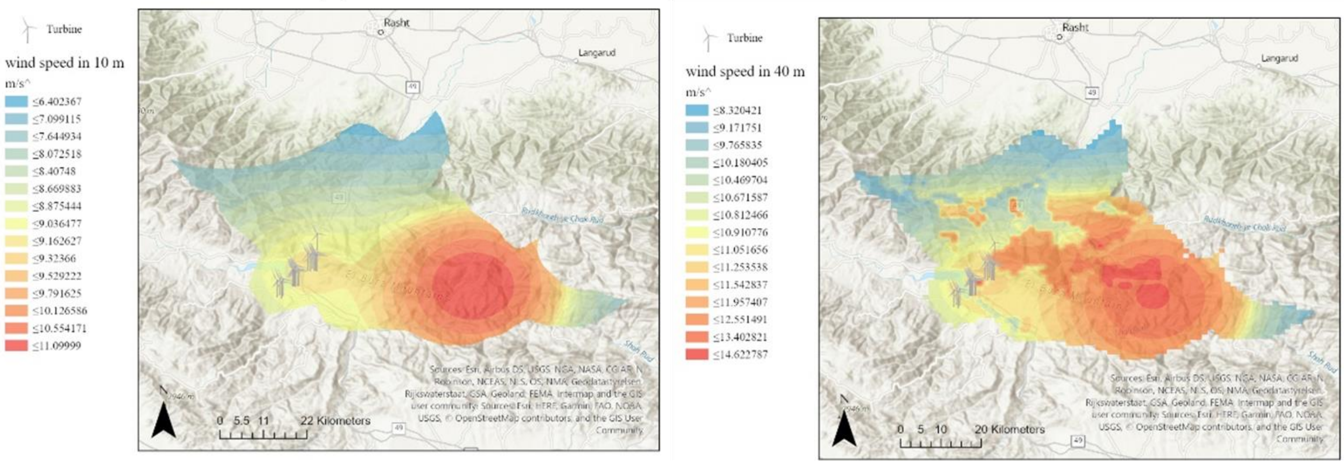

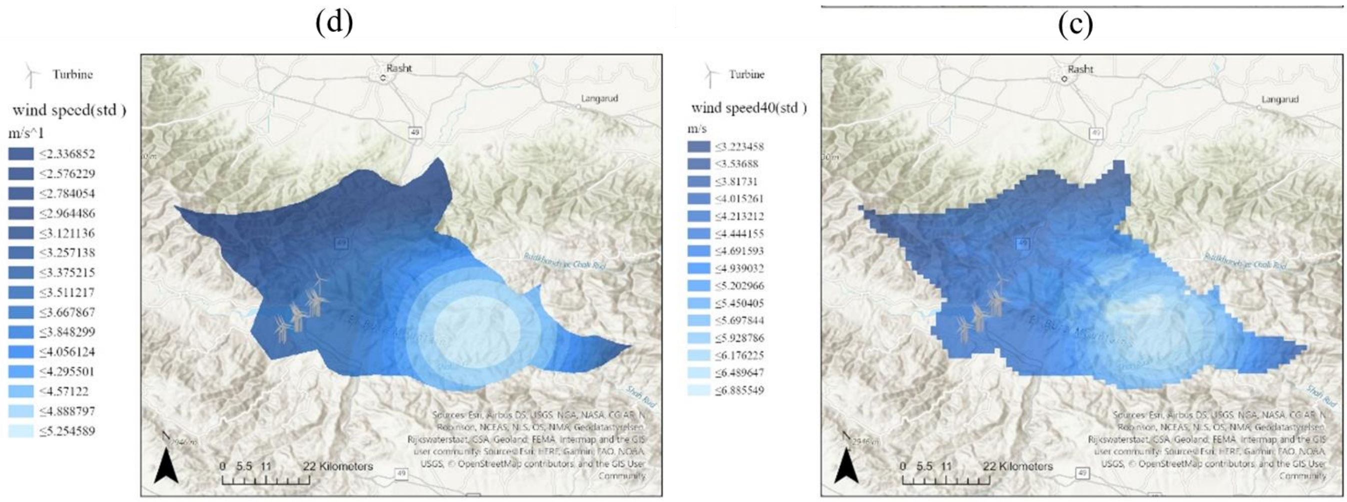

Figure 8. Average and average wind speed deviation;
(a): At a height of 40 meters, (b): At a height of 10 meters
(c): At a height of 40 meters , (d): At a height of 10 meters

Based on the results of modeling, the probability distribution function of the Weibull function of the k-statistic for the region is 2.32. This function will ensure that the speed is repeated. The experimental Weibull function model in the equation for the wind shape index or C states the value of 10.79, which shows a lower estimate according to the wind speed map at a height of 40 meters above the surface. In general, among the existing methods, the EPF experimental scattering index has shown that the scattering probability will have a range of 1.8, which is a good condition. A noteworthy point according to the wind speed chart is the presence of two peaks in Manjil wind speed. The first peak is related to the continuous flow of wind speed in the range of 2 meters per second, which is referred to as non-functional wind in the power plant. The second peak that makes the Manjil region significant is in the range of 12 meters per second due to the morning flow from the Caspian Sea and the mountains to the Qazvin plain. The Weibull distribution diagram has a skew to the right, which is why the average velocity estimate is less than the reality in the speed range of 6 meters per second. This difference causes the probability estimator to have a negative tendency towards a low probability density and to count the estimate as lower.

The wind energy power map shows that the power density range is 145 to 305 watts per square meter. The high power of the region, considering the average of 238 watts per square meter, shows that the construction of small and large power plants will be potentially profitable. In general, based on the output of the model, the highest wind energy power is located around the city of Manjil. The highest power point is located at the shore of Manjil Dam and at the Manjil site. In total, 23% of the total area is in Class 5 of the World Wind Energy Classification Standard. From the total area of the study area, modeling estimates show that 50% is in the optimal class 4 with a range of 200 to 250 watts. The other 30% of the region has low thrust power, so it does not have the efficiency of industrial power plants.

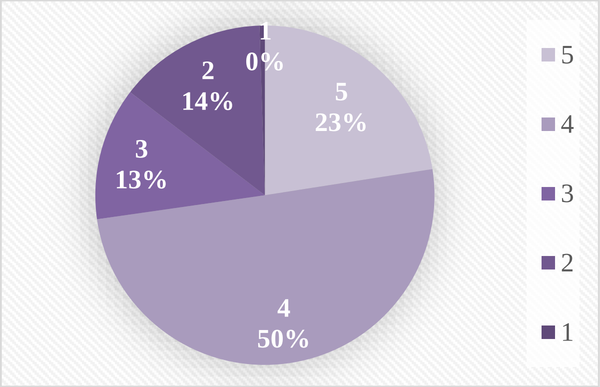

Figure 9. Graph of the frequency of energy classes in the study area

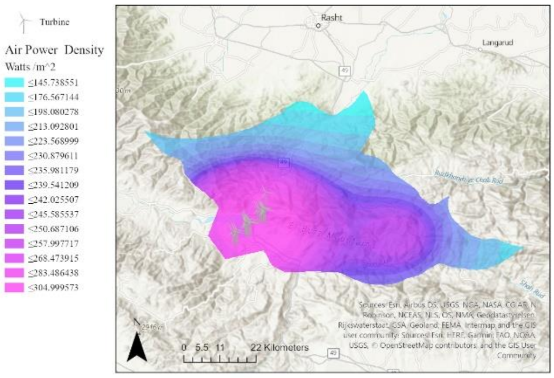

Figure 10. Power density zone map

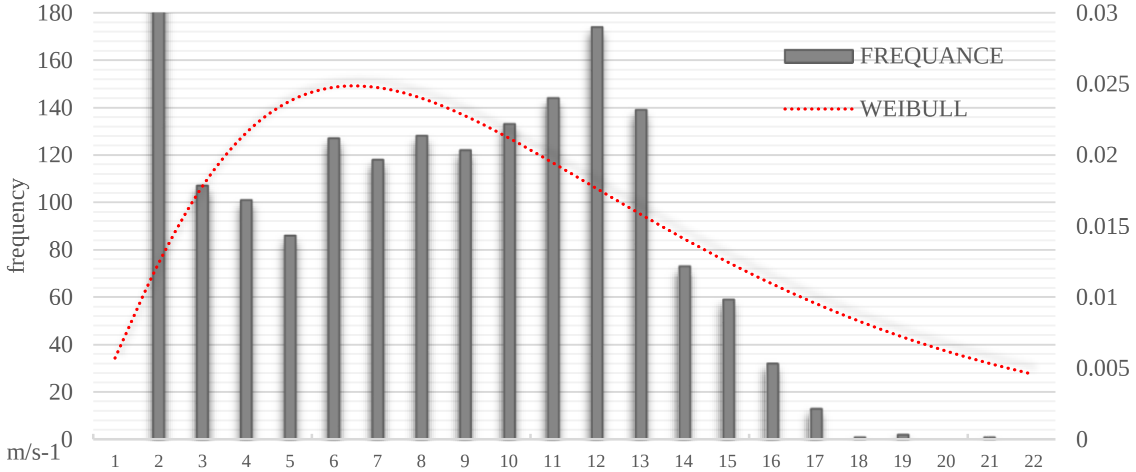

Figure 11. Frequency diagram of wind speed and Weibull probability distribution

Based on the results, the nominal energy potential generated for the four wind turbine models available at the study sites shows the high efficiency of the 550 models with a maximum power of one million watts per year with a factor coefficient of 42%, which is close to optimal capability and efficiency. The issue of 300 MW turbines with a capacity factor of 28% has a lower efficiency in energy production due to the limitation of wind speed due to the speed range in the region. The results of the model show that the use of heavier turbines with power class more than 5 capacities has a more limiting factor of 29%.

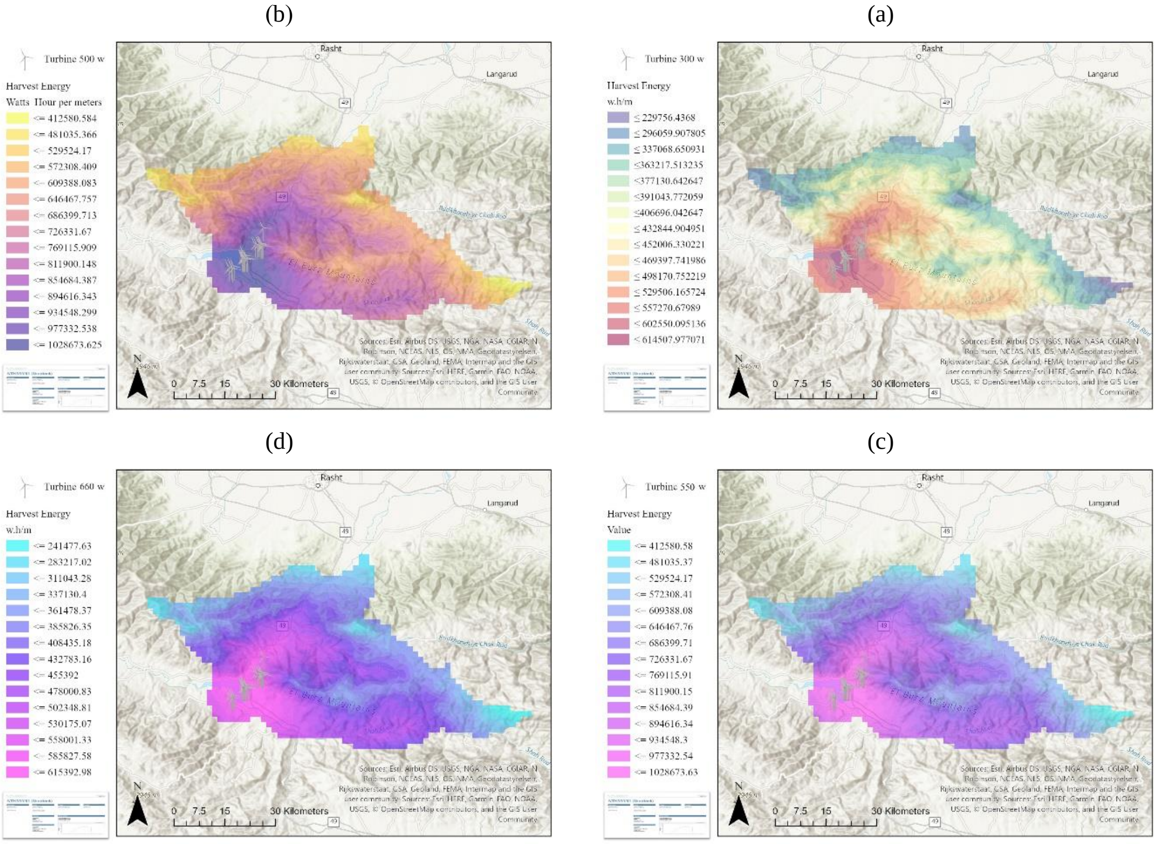

Figure 12. Turbine harvest energy;
(a): 300 w, (b): 500 w
(c): 550w , (d): 660 w

To evaluate the existing wind energy power model with the existing reality in the four power plants show that there is a significant negative difference in harvest energy. Separating the turbines and the site separately, Table 1 shows that the 300-megawatt turbines at the Manjil site generate 9.25 million watts per year, compared to the estimated 8.64 million watts in the model, which is 6.6% lower than reality. The 500-watt turbine has a very small difference of -0.2%. At the Manjil site, 550-watt turbines with 11 units have the highest difference of 10.56% - the model has suffered the most negative errors in this section. On the other hand, due to the high power density of the Manjil site, 660 MW turbines with 22 units on the shore of Manjil dam have a low error of 1.53%. Siahpoosh site in the west of Manjil and south of Manjil dam lake has a uniform and homogeneous composition in the level of turbines, this site with 24 660 MW turbines has a lower error in all sites with - 0.18%. Herzeville site at the top of Mount Manjil has estimated the highest error of the model in terms of error. In this site, the effect of the topographic parameter is more visible and the threshold error has reached -10 and -12%. At the Rudbar site, the high altitude has caused the effect of topography and local flow to create a certain torsion, which makes the model estimate the reality lower than usual. Finally, an overall estimate of the energy production field report for the one-year period shows that 123.2 million kilowatts of energy were produced, compared to the model estimate of 116.7 million kilowatts. The difference in the percentage of error changes is negative -5.31% of the total, an acceptable error in the negative direction, which is due to the Weibull estimator due to the right Skewness. Therefore, according to the results of the wind speed filter and the removal of noise below the threshold speed of 4 meters per second, the experimental estimator of Weibull is stretched to the peak. On the other hand, the correction of wind gauges is more important in bringing the equations closer to reality.

Table 1.Site specifications and changes in Power plant and Model output

Sites	Turbine type	Number	Power plant output (KWh hours per year)	Model output (KWh hours per year)	CV[2]
Manjil	300	14	9,256,350.00	8,639,849.75	-6/6%
	500	1	1,030,693.00	1,028,673.63	-0/2%
	550	11	18,970,572.00	16,967,415.00	-10/56%
	660	22	29,840,981.00	29,383,395.25	-1/53%
Siahpoosh	660	24	31,490,390.00	31,433,565.00	-0/18%
Herzweil	300	12	7,447,500.00	6,663,163.50	-10/53%
	660	15	20,658,421.00	18,209,512.50	-11/85%
Rudbar	500	1	993,080.00	925,867.63	-6/77%
	550	3	3,508,149.00	3,393,483.00	-3/27%
total	-	93	123,196,136.00	116,644,925.25	-5/31%

Summary of spatial fit and arrangement of turbines shows that Manjil power plant in world energy class has sufficient quality of energy production and can be compared with global sites. This site with a nominal capacity of 240 million kilowatt-hours per year is one of the largest sites in the Middle East with a capacity factor of 0.25. Therefore, it has the lowest coefficient of modeling and design changes. For this reason, this site is considered an excellent control fuehrer with its appropriate density and layout. According to the obtained results, the Siahpoosh site with a capacity of 410 million kilowatt-hours per year has a limited factor capacity of 8%. This site has a coefficient of variation of 11%, which modeling shows that the choice of 660 MW turbines is not very appropriate and practical. Therefore, it seems that the use of 500 kW turbines has a better capability than 660 turbines on this site. Based on the results, the two sites of Rudbar and Herzeville have a very proportionate factor capacity, so these two sites can be upgraded according to the installation of Class 4 and 3 turbines.

Table 2. Compare different powers and capacity factor of sites

Sites	Area (meters)	CV	The calculated power of the model	Reported power	Nominal power	capacity factor
Manjil	3875	0.3	56019333.63	59098596	240637200	25%
Siahpoosh	11616	11.1	31,433,565.00	31490390	410493600	8%
Herzeville	9680	5	4319350.63	4501229	18834000	24%
Rudbar	3872	0.28	24872676.00	28105921	118260000	24%

---

[2] coefficient of variation

4. Conclusions

Comparison of production capacity of Manjil site in Rudbar based on energy production capacity model and comparison of its capacity with coastal and offshore sites shows that this site is comparable to sites such as Robin Riga America with a capacity of 180 MWh due to the topographic parameter[43]. Has. Also, according to the reports provided, the good power that is on this site will be able to provide energy consumption for 300,000 inhabitants. Compared to the London Array site, with a capital of less than $ 200 million, it has a higher capability of using 500 MW turbines.

Based on the most basic input parameters, the model has a high detection in identifying the potential and actual power of sites because the output specifications and details show that the model has a prediction error of less than 5% for power measurement. And in comparison with the estimates of the scattering parameters of the Weibull function to evaluate the power of wind energy and to evaluate the accuracy of models in reality in the United States by [44]who stated the error is 20% of the total, the model emphasizes low error . Compared to identifying wind energy power models and comparing reality using ARMA time series models in Canada by [45] the model uses artificial intelligence algorithms to filter its dynamics in filtering time noise and data incompetence. Expresses it in a more optimal way. Therefore, compared to the study and general review of various wind energy estimation methods and MONTE CARLO simulation revision in power plant power output estimation in China [46], this model has specific spatio-temporal frequencies compared to non-functional filters such as [47]. This software package utilizes the use of fuzzy techniques and neural networks to increase the speed of calculations and increase the accuracy of models to assess the accuracy of power plants in the Netherlands [48]native capability for a large area of Iran and its diverse climate has found.

5. References

[1] Karki R, Billinton R. Cost-effective wind energy utilization for reliable power supply. IEEE Transactions on Energy Conversion. 2004; 19(2): 435-440.

[2] Gude VG, Fthenakis V. Energy efficiency and renewable energy utilization in desalination system .Progress in Energy. 2020; 2(2): 022003.

[3] Hashemzadegazar M, Azizi G, Karimi M, Khoshakhlagh F, Shamsipour A. Performance Evaluation of ERA-ENTRIM in spatio-temporal distribution and wind speed trend in eastern Iran. Physical Geography Research Quarterly. 2020; 52(4): 515-533.

[4] Pryor SC, Barthelmie RJ. A global assessment of extreme wind speeds for wind energy applications. Nature Energy. .9-2021:1

[5] Zhang L. Wind Energy Development: History and Current Status. Wind, Water and Fire: The Other Renewable Energy Resources: World Scientific; 2021. p. .6-1

[6] Baxter J, Walker C, Ellis G, Devine-Wright P, Adams M, Fullerton RS. Scale, history and justice in community wind energy: An empirical review. Energy Research & Social Science. 2020; 68:101532.

[7] Nazir MS, Mahdi AJ, Bilal M, Sohail HM, Ali N, Iqbal HM. Environmental impact and pollutionrelated challenges of renewable wind energy paradigm–a review. Science of the Total Environment. 2019; 683:436-444.

[8] Roy A, Bandyopadhyay S. Wind Energy Systems. Wind Power Based Isolated Energy Systems: Springer; 2019. pp.17 - 32

[9] Kaldellis JK, Zafirakis D. The wind energy (r) evolution: A short review of a long history. Renewable energy. 2011;36(7): 1887-1901.

[10] Cantoni R. Energy and civilization. A history (Vaclav Smil, 2017). Journal of Energy History/Revue d'Histoire de l'Énergie [Online]

[11] Sadorsky P. Wind energy for sustainable development: Driving factors and future outlook. Journal of Cleaner Production. 2021; 289:125779.

[12] Li L, Lin J, Wu N, Xie S, Meng C, Zheng Y, et al. Review and Outlook on the International Renewable Energy Development. Energy and Built Environment. 2020.

[13] Groups I. International Renewable Energy Agency (IRENA) 2020. Available from: ttps://www.irena. org/wind.

[14] El Bassam N. Wind energy. Distributed Renewable Energies for Off-Grid Communities: Elsevier; 2021. pp. 63-149.

[15] IRENA. Renewable Energy and Jobs Annual Review 2020.

[16] Erdogan S, Okumus I, Guzel AE. Revisiting the Environmental Kuznets Curve hypothesis in OECD countries: the role of renewable, nonrenewable energy, and oil prices. Environmental Science and Pollution Research. 2020; 27: 23655-23663.

[17] Manwell JF, McGowan JG, Rogers AL. Wind energy explained: theory, design and application: John Wiley & Sons; 2010.

[18] Wadi M, Elmasry W. Statistical analysis of wind energy potential using different estimation methods for Weibull parameters: a case study. Electrical Engineering. 2021; 103: 2573–2594.

[19] Kwon S-D. Uncertainty analysis of wind energy potential assessment. Applied Energy. 2010; 87(3): 856-865.

[20] Karsli V, Gecit C. An investigation on wind power potential of Nurdağı-Gaziantep, Turkey. Renewable Energy. 2003; 28(5): 823-830.

[21] Ruiz SAG, Barriga JEC, Martínez JA. Wind Power Assessment in the Caribbean Region of Colombia, Using Ten-Minute Wind Observations and Era 5Data. Renewable Energy.2021.

[22] Palese C, Lässig JL, Cogliati MG, Bastanski MA. Wind regime and wind power in North Patagonia, Argentina. Wind Engineering. 2000; 24(5): 361-377.

[23] Sterns A, Manuel L, Saranyasoontorn K, Nelson L. Analysis of time series data on wind turbine loads. National Science Foundation, Arlington, VA, Tech Rep. 2003.

[24] Elliott D, Schwartz M. Wind energy potential in the United States .Pacific Northwest Lab., Richland, WA (United States); 1993.

[25] Zheng C-w, Li C-y, Xu J-j. Micro-scale classification of offshore wind energy resource——A case study of the New Zealand. Journal of cleaner production. 2019; 133: 2261-2241.

[26] Mostafaeipour A, Jadidi M, Mohammadi K, Sedaghat A. An analysis of wind energy potential and economic evaluation in Zahedan, Iran. Renewable and Sustainable Energy Reviews. 2014; 641: 30-50.

[27] Hashemi-Tilehnoee M, Babayani D, Khaleghi M. Evaluating wind energy potential in Gorgan-Iran using two methods of Weibull distribution function. International Journal of Renewable Energy Development. 2016; 5(1): 43-48.

[28] Keyhani A, Ghasemi-Varnamkhasti M, Khanali M, Abbaszadeh R. An assessment of wind energy potential as a power generation source in the capital of Iran, Tehran. Energy. 2010; 35(1): 188-201.

[29] Ashrafi ZN, Ghasemian M, Shahrestani MI, Khodabandeh E, Sedaghat A. Evaluation of hydrogen production from harvesting wind energy at high altitudes in Iran by three extrapolating Weibull methods. International Journal of Hydrogen Energy. 2018; 43(6):3110-3132.

[30] Mostafaeipour A, Abarghooei H. Harnessing wind energy at Manjil area located in north of Iran. Renewable and Sustainable Energy Reviews. 2008; 12(6):1758-1766.

[31] Afiesimama E, Pal J, Abiodun B, Gutowski W, Adedoyin A. Simulation of West African monsoon using the RegCM3. Part I: model validation and interannual variability. Theoretical and Applied Climatology. 2006; 86(1): 23-37.

[32] Ciang CC, Lee J-R, Bang H-J .Structural health monitoring for a wind turbine system: a review of damage detection methods. Measurement science and technology. 2008; 19(12): 122001.

[33] Akdağ SA, Dinler A. A new method to estimate Weibull parameters for wind energy applications. Energy conversion and management. 2009; 50(7): 1761-1767.

[34] Ouahabi MH, Elkhachine H, Benabdelouahab F, Khamlichi A. Comparative study of five different methods of adjustment by the Weibull model to determine the most accurate method of analyzing annual variations of wind energy in etouanMorocco. Procedia Manufacturing. 2020; 6: 698-707.

[35] Teyabeen AA, Akkari FR, Jwaid AE, editors. Comparison of seven numerical methods for estimating weibull parameters for wind energy applications. 2017 UKSim-AMSS 19th International Conference on Computer Modelling & Simulation (UKSim); 2017: IEEE.

[36] Justus C, Hargraves W, Mikhail A, Graber D. Methods for estimating wind speed frequency distributions. Journal of applied meteorology. 1978; 17(3): 350-353.

[37] Hau E. Wind turbines: fundamentals, technologies, Application, Economics: Springer Science & Business Media; 2013.

[38] Porté-Agel F, Wu Y-T, Lu H, Conzemius RJ. Large-eddy simulation of atmospheric boundary layer flow through wind turbines and wind farms. Journal of Wind Engineering and Industrial Aerodynamics. 2011; 99(4): 154 -168.

[39] Zhou H, Lu Y, Liu X, Chang R, Wang B. Harvesting wind energy in low-rise residential buildings: Design and optimization of building forms. Journal of Cleaner Production. 2017; 167: 306-316.

[40] Whitcomb RT. A design approach and selected wind tunnel results at high subsonic speeds for wing-tip mounted winglets. 1976.

[41] Burton T, Harpe D, Jenkins N, Bossanyi E. Wind Energy Handbook. 2002: 511-558.

[42] Gasset N, Landry M, Gagnon Y. A comparison of wind flow models for wind resource assessment in wind energy applications. Energies. 2012; 5(11): 288-322.

[43] Oteri FA, Baranowski RE, Baring-Gould EI, Tegen SI. 2017State of Wind Development in the United States by Region. National Renewable Energy Lab.(NREL), Golden, CO (United States); 2018.

[44] Seguro J, Lambert T. Modern estimation of the parameters of the Weibull wind speed distribution for wind energy analysis. Journal of wind engineering and industrial aerodynamics. 2000; 85(1): 75-84.

[45] Karki R, Hu P, editors. Wind power simulation model for reliability evaluation. Canadian Conference on Electrical and Computer Engineering, 2005; 2005: IEEE.

[46] Wen J, Zheng Y, Donghan F. A review on reliability assessment for wind power. Renewable and sustainable energy reviews. 2009; 13(9):2485-2494.

[47] Yu Z, Tuzuner A, editors. Fractional weibull ind speed modeling for wind power production estimation. 2009IEEE Power & Energy Society General Meeting; 2009: IEEE.

[48] Jafarian M, Ranjbar A. Fuzzy modeling techniques and artificial neural networks to estimate annual energy output of a wind turbine. Renewable Energy. 2010; 35(9): 2008-2014.